

RL-TR-93-157
In-House Report
August 1993

AD-A275 818



PHOTONIC DEVICES AND SYSTEMS FOR OPTICAL SIGNAL PROCESSING

Michael A. Parker, Paul D. Swanson, Stuart I. Libby, 1/Lt,
USAF

DTIC
ELECTE
FEB 16 1994
S B D

APPROVED FOR PUBLIC RELEASE; DISTRIBUTION UNLIMITED.

BEST AVAILABLE COPY

94-05105



DTIC QUALITY INSPECTED 8

Rome Laboratory
Air Force Materiel Command
Griffiss Air Force Base, New York

01 0 1 5 001

**Best
Available
Copy**

This report has been reviewed by the Rome Laboratory Public Affairs Office (PA) and is releasable to the National Technical Information Service (NTIS). At NTIS it will be releasable to the general public, including foreign nations.

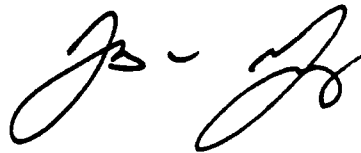
RL-TR-93-157 has been reviewed and is approved for publication.

APPROVED:



JAMES W. CUSACK, Chief
Photonics & Optics Division
Surveillance & Photonics Directorate

FOR THE COMMANDER:



JAMES W. YOUNGBERG, LtCol, USAF
Deputy Director
Surveillance & Photonics Directorate

If your address has changed or if you wish to be removed from the Rome Laboratory mailing list, or if the addressee is no longer employed by your organization, please notify RL (OCPB) Griffiss AFB NY 13441-5700. This will assist us in maintaining a current mailing list.

Do not return copies of this report unless contractual obligations or notices on a specific document require that it be returned.

REPORT DOCUMENTATION PAGE

Form Approved
OMB No. 0704-0188

Public reporting burden for this collection of information is estimated to average 1 hour per response, including the time for reviewing instructions, searching existing data sources, gathering and maintaining the data needed, and completing and reviewing the collection of information. Send comments regarding this burden estimate or any other aspect of this collection of information, including suggestions for reducing this burden, to Washington Headquarters Service, Directorate for Information Operations and Reports, 1215 Jefferson Davis Highway, Suite 1204, Arlington, VA 22202-4302, and to the Office of Management and Budget, Paperwork Reduction Project (0704-0188), Washington, DC 20503.

1. AGENCY USE ONLY (Leave Blank)		2. REPORT DATE August 1993		3. REPORT TYPE AND DATES COVERED In-House Apr 89 - Sep 91	
4. TITLE AND SUBTITLE PHOTONIC DEVICES AND SYSTEMS FOR OPTICAL SIGNAL PROCESSING				5. FUNDING NUMBERS PE - 62702F PR - 4600 TA - P3 WU - 05	
6. AUTHOR(S) Michael A. Parker, Rome Laboratory; Paul D. Swanson, Cornell University; Stuart I. Libby, 1Lt, USAF, Rome Laboratory					
7. PERFORMING ORGANIZATION NAME(S) AND ADDRESS(ES) Rome Laboratory (OCPB) 25 Electronic Pky Griffiss AFB NY 13441-4515				8. PERFORMING ORGANIZATION REPORT NUMBER P9-H006	
9. SPONSORING/MONITORING AGENCY NAME(S) AND ADDRESS(ES) Rome Laboratory (OCPB) 25 Electronic Pky Griffiss AFB NY 13441-4515				10. SPONSORING/MONITORING AGENCY REPORT NUMBER RL-TR-93-157	
11. SUPPLEMENTARY NOTES Rome Laboratory Project Engineer: Michael A. Parker/OCPB (315) 330-7671					
12a. DISTRIBUTION/AVAILABILITY STATEMENT Approved for public release; distribution unlimited.				12b. DISTRIBUTION CODE	
13. ABSTRACT (Maximum 200 words) This report is a compilation of the preliminary designs, fabrication and test results for multiquantum well optical amplifiers, stripe and square broad area lasers, model switched optical memory elements, optical RS flip flop, NOR gates, photo-detectors and acousto-optic switches.					
14. SUBJECT TERMS multiquantum well optical amplifiers, photodetectors, NOR gates, optical RS flip flop, acousto-optic switches				15. NUMBER OF PAGES 150	
				16. PRICE CODE	
17. SECURITY CLASSIFICATION OF REPORT UNCLASSIFIED	18. SECURITY CLASSIFICATION OF THIS PAGE UNCLASSIFIED	19. SECURITY CLASSIFICATION OF ABSTRACT UNCLASSIFIED	20. LIMITATION OF ABSTRACT U/L		

ABSTRACT

This final report is a compilation of the design, fabrication and test results for multi-quantum well optical amplifiers, stripe and square broad area lasers, mode switched optical memory elements, optical RS flip flops, NOR gates, photodetectors and acousto-optic switches. All of these laser based devices, except one of the amplifiers, were developed in-house. The phenomenological theory of laser operation is discussed. The processing sequence for the devices is presented with data on the P^+ electrical contacts. Both commercial and in-house optical amplifiers were investigated for gain and threshold current. Stripe lasers with total internal reflection mirrors were tested for emitted power versus injected current (L-I curves). Broad area lasers with both Uniformly Pumped and Gain Guided Arrayed gain sections were tested for L-I and emission spectra as a function of the voltage applied across intracavity saturable absorbers. The mode switched optical memory elements were designed to use the broad area lasers. The optical RS flip flops have two quench lasers, a main laser and a saturable absorber to develop the bistable output characteristics. Data is presented for the hysteresis and quenching. Data is presented for an optical NOR gate which uses three heterostructure lasers with total internal reflection mirrors and operates on the principle of laser quenching. Some memory elements and logic gates require integrated photodetectors to determine the logic state of the device; therefore, heterostructure photodetectors are discussed in terms of parasitic capacitance and the photocurrent response versus both wavelength and intensity of the optical excitation. The design and performance of an acousto-optical switch is also presented.

Accession For	
NTIS - ARI	<input checked="" type="checkbox"/>
DTIC TAB	<input type="checkbox"/>
Unannounced	<input type="checkbox"/>
Justification	
By _____	
Distribution/	
Availability Codes	
Dist	Avail and/or Special
A-1	

ACKNOWLEDGMENTS

The editors wish to acknowledge the following individuals for authoring the original work in their specific areas:

J.M. Battiato, D.A. Honey, and M.A. Parker, "Characterization of a Semiconductor Optical Amplifier for Use in Optical Computing Systems," RL Technical Memorandum, RL-TM-91-6, June 1991.

J.H. Maurice and M.A. Parker, "Acousto-Optic Bistable Device," RL Technical Memorandum, (Submitted for Publication), July 1990.

D.A. Honey and Michael Parker, "AutoCad to Symbad Conversion Utility," RL Technical Memorandum, RL-TM-92-19, September 1992.

The editors also wish to acknowledge the contributions of the following individuals: W. J. Grande, C. L. Tang and R. J. Michalak for many of the ideas presented here; P. Banerjee for his assistance with the early stages of the acousto-optic switch experiments; R. J. Bussjager for helpful discussions on the optics for electro-optic probe stations and for focusing semiconductor lasers; M. Moore and K. Olson for their help with the measurements of the temperature dependence of the P^+ electrical contacts, software and optical fibers; J. M. Osman and B. Longacre for supplying the Ti-Sapphire laser and assisting with its setup.

All three editors of this report were involved with the design, fabrication and testing of the devices.

TABLE OF CONTENTS

ABSTRACT.....	i
ACKNOWLEDGMENTS.....	ii
TABLE OF CONTENTS.....	iii
LIST OF FIGURES	iv
LIST OF TABLES	v
I. INTRODUCTION	1
II. THE IMPORTANCE OF OPTICAL LOSS FOR THE DIFFERENTIAL EFFICIENCY AND THE THRESHOLD CURRENT IN MULTIPLE QUANTUM WELLS	4
III. FABRICATION OF RIDGE WAVEGUIDED PHOTONIC CIRCUITS WITH CHEMICALLY ASSISTED ION BEAM ETCHING	13
IV. P ⁺ ELECTRICAL CONTACTS ON GaAs.....	18
V. APPARATUS FOR THE ANALYSIS OF OPTICAL LOGIC GATES AND COMPONENTS	30
VI. CHARACTERIZATION OF A SEMICONDUCTOR OPTICAL AMPLIFIER FOR USE IN OPTICAL COMPUTING SYSTEMS	44
VII. GaAs-AlGaAs LASER AMPLIFIERS WITH ANGLED FACETS	55
VIII. A SQUARE BROAD-AREA MULTIPLE QUANTUM WELL LASER	65
IX. AN OPTICAL NOR GATE BASED ON GaAs-AlGaAs HETEROSTRUCTURE LASERS	71
X. AN OPTICAL RS FLIP FLOP	76
XI. MULTIPLE QUANTUM WELL PHOTODETECTORS	84
XII. AN ACOUSTO-OPTIC BISTABLE SWITCH	90
XIII. AUTOCAD TO SYMBAD CONVERSION UTILITY	112
XIV. CONCLUSIONS/SUMMARY	119
REFERENCES	120
APPENDIX	
APPENDIX 2.A: Relation For Photon Density, Mirror Reflectivity, Irradiance and Flux	A1
APPENDIX 2.B: Relation Between the Mirror Reflectivity and the Cavity Lifetime	A2
APPENDIX 4.A: Distributed Impedance Models	A5
APPENDIX 13.A: Autocon Program Listing.....	A10

LIST OF FIGURES

Figure 2.1: Intrinsic Gain versus Carrier Density	5
Figure 2.2: Intensity vs. Reflectivity	8
Figure 2.3: Predicted Differential Efficiency	9
Figure 2.4: Threshold Current and $1/D'$	9
Figure 2.5: Quantum Well Laser with Total Internally Reflecting Mirrors	10
Figure 2.6: Experimental L-I Curves	10
Figure 3.2: Views of Intersecting Laser Cavities at Progressive Stages in Fabrication	16
Figure 3.3: SEM of a Total Internal Reflecting Mirror	17
Figure 4.1: Resistance vs. Distance Between Two Metal Electrodes Plot	20
Figure 4.2: The Layered Structure of the Electrodes	22
Figure 4.3: Fabricated Contact Geometry	24
Figure 4.4: Typical I-V Plot for Contact Structures	24
Figure 4.5: Typical Plots of Resistance vs. Distance for GL100 and G85 Contact Structures	25
Figure 4.6: Temperature Dependence on Resistance for Metal	26
Figure 4.7: Temperature Dependence on Resistance for P^+ GaAs	27
Figure 5.1: Electro-Optic Probe Station	31
Figure 5.2: Device Mount Block	32
Figure 5.3: Cooling System	32
Figure 5.4: Optical Probe	33
Figure 5.5: Probe Contact Integrity Test	34
Figure 5.6: Test Setup for Basic Device Optical and Electrical Characterization	35
Figure 5.7: Low-Speed Current Amplifier	38
Figure 5.8: Fast Current Amplifier	38
Figure 5.9: Photodetector Circuit	39
Figure 5.10: Characteristic Curves for a Laser Amplifier with 0.57° Facets	40
Figure 5.11: Characteristic I-V and L-I Curves for CELL Devices in the Off State	41
Figure 5.12: Hysteresis Displayed on the DSO	42
Figure 5.13: Lissajous Figure Width versus Drive Current and Pulse Width	42
Figure 5.14: Quenching Example	43
Figure 6.1: Schematic of SOA Amplifier	45
Figure 6.2: Experimental Setup	49
Figure 6.3: Peak Wavelength of Spontaneous Emission vs. Bias Current	50
Figure 6.4: Spontaneous Emission Spectra for Various Bias Currents	50
Figure 6.5: Power of Spontaneous Emission vs. Bias Current	51
Figure 6.6: SOA Gain vs. Bias Current	51
Figure 6.9: Gain vs. Input Power Curves as a Function of Bias Current	52
Figure 6.10: L-I Curve for the SOA	52
Figure 6.11: $(S/N)_n$ of the SOA	54
Figure 7.1: The Laser Amplifier with Angled Facets	56
Figure 7.2: Fabrication Processing Steps	57
Figure 7.3: Test Setup for Basic Optical and Electrical Characterization	58
Figure 7.4: L-I Curves for Amplifiers with 0.573° and 7.97° Facet Angles	60
Figure 7.5: Laser Amplifier Threshold Current versus Facet Angle	61
Figure 7.6: Differential Efficiency versus Facet Angle	61
Figure 7.7: Amplifier Gain Measurement	61
Figure 7.8: Gain vs. Wavelength for Laser Amplifiers	62
Figure 8.1: Gain Guided Arrayed Broad Area Laser	66
Figure 8.2: L-I for the Gain Guided Arrayed Laser	68
Figure 8.3: Spectra for the Gain Guided Arrayed Laser	69
Figure 8.4: Spectra for the Uniformly Pumped Laser	69
Figure 9.1: The Optical NOR Gate	71
Figure 9.2: NOR Gate Quench Curves	73

Figure 10.1: The RS Flip-Flop and Hysteresis in the L-I Characteristics	77
Figure 10.2: The Components of the RS Flip-Flop	79
Figure 10.3: RS Flip-Flop Hysteresis Plot and Experimental Setup	80
Figure 10.4: Hysteresis Loop Width versus Saturable Absorber Voltage Plot	81
Figure 11.1: The Multiquantum Well Photodetector	84
Figure 11.2: Frequency Dependence on the Capacitance of Rectangular Photodetectors	85
Figure 11.3: Frequency Dependence on the Capacitance of Square Photodetectors	86
Figure 11.4: Voltage Dependence on the Capacitance of Rectangular Photodetectors	86
Figure 11.5: Voltage Dependence on the Capacitance of Square Photodetectors	87
Figure 11.6: Capacitance versus Photodetector Area for Varying Voltages and Frequencies	87
Figure 11.7: Photocurrent versus Incident Beam Power	88
Figure 11.8: Response versus Wavelength Plot	89
Figure 12.1: Basic Principles of AO Operation	92
Figure 12.2: Basic Setup for Bistable Operation	93
Figure 12.3: Experimental Setup (Modified Setup for Incremental α_0)	97
Figure 12.4: Illustration of Hysteresis Loop	98
Figure 12.5: Typical Form of the Relationship between X_{n+1} and X_n	100
Figure 12.6: Illustration of the Iterates of x_0	101
Figure 12.7: Experiment with Parameters Labeled	103
Figure 12.8: Photodetector and Scaling-Summer Circuits	104
Figure 12.9: Linearity of the p-i-n Diode	106
Figure 12.10: Photographs of Behavior: Minimum β to Maximum β	107
Figure 12.11: Definitions for Voltages	108
Figure 2B1: Normalized Cavity Energy Plot	A4
Figure 4A1: Contact Structures and Corresponding Discrete Component Circuit Models	A5
Figure 4A2: Voltage and Current Distribution along Metal Electrode Plots	A8
Figure 4A3: Effective Input Resistance as a Function of the Metal and P^+ GaAs Resistance	A8

LIST OF TABLES

Table 4.1: Table of Resistances	26
---------------------------------------	----

I. INTRODUCTION

The field of optical signal processing¹ has existed since the advent of the first lenses but its potential advantages have never been fully exploited. An optical signal processor can be massively parallel, high speed, immune to EMI, small and inexpensive, and capable of direct image processing. At present, several forms of analog optical processors exist, but all of them lack the precision often required of a digital processor. As with the conventional electronic computers, digital optical signal processors require logic gates, memory elements, input / output devices and instruction sets. The Photonics Center 4600P305 Optical Component Development and Characterization work unit was specifically established to develop preliminary logic devices, memory elements, waveguides and support devices necessary to realize an optical signal processor.

Since the early 1960s, one of the most promising types of logic gates and memory elements have consisted of semiconductor lasers.² However, high laser threshold currents and the lack of integration techniques limited the usefulness of early designs. Recent developments in the epitaxial growth techniques for quantum well heterostructures and the processing techniques have since made the early designs attractive for optical signal processing purposes.

Several semiconductor, laser based devices have been developed. After carefully examining a laser amplifier from BTB, in-house lasers were designed fabricated and tested. The amplifiers had angled etched facets without an AR coating. They were tested for gain, threshold current as a function of facet angle and differential efficiency as a function of facet angle. For the devices tested, the threshold current increased with facet angle and the gain was on the order of unity.

A new single element broad area laser (200 X 200 μm in area) has been designed, fabricated and tested for use as an integrated optical memory element or logic gate. The design incorporates two intracavity saturable absorbers to control two orthogonal lasing modes. The far field pattern indicates a 30 degree divergence angle in the horizontal direction with fairly uniform emission over the length of the mirror facet. The broad area laser has applications as an integrated mode switched optical memory element.

The RS flip flop was designed, fabricated and tested as integrated optical memory element. The flip flop has three GaAs-AlGaAs heterostructure lasers with total internal reflection mirrors. A main laser incorporates a saturable absorber to develop the bistable output characteristics. A pump laser bleaches the absorber to set the logic 1 state. A third laser quenches the main laser to reset the device to logic 0. The experiments and data for the laser quenching and bistability are presented in the RS FLIP FLOP chapter.

Optical NOR gates consisting of GaAs-AlGaAs heterostructure lasers were designed, fabricated and tested. The lasers have etched ridge waveguides and total internal reflection mirrors. Either of two quench lasers can optically quench a main laser to achieve the NOR operation. Data is presented for the quench phenomena and for the characteristics of the emitted optical flux versus the injected current for the main laser.

Many of the devices developed require photodetectors to determine the output logic state; consequently, photodetectors were integrated onto the same heterostructure as the other devices. They were tested for shunt capacitance and photocurrent response as a function of incident light intensity and wavelength.

Although not an integrated device, an acousto-optic switch was developed. A HeNe beam is diffracted from an acousto-optic modulator (Bragg cell) into a pin photodetector. The pin photocurrent is amplified and routed back into the Bragg cell. The positive feedback induces hysteresis and allows the switch to latch.

Many of the following chapters are condensations, revisions and reprints of technical memorandums, technical reports and journal articles published in connection with the 4600P305 work unit. The chapters begin with a discussion of semiconductor laser operation; this chapter stresses the importance of optical loss mechanisms in the laser cavity for determining the threshold current and differential efficiency. The subsequent chapter details the fabrication process with emphasis on waveguide theory. A chapter on the P^+ electrical contacts covers more of the fabrication process and also discusses the quality of the P^+ contacts. Most of the chapters contain additional processing related steps not covered in the chapter on fabrication. Next, the experimental procedures and apparatus are discussed. The remainder of the

chapters are concerned with the following topics: a commercial laser amplifier, a heterostructure laser amplifier with angled facets, a square broad area laser, mode switched optical memory elements, RS flip flops, NOR gates, photodetectors and an acousto-optic switch.

II. THE IMPORTANCE OF OPTICAL LOSS FOR THE DIFFERENTIAL EFFICIENCY AND THE THRESHOLD CURRENT IN MULTIPLE QUANTUM WELL LASERS

This chapter stresses the importance of optical losses associated with the laser cavity for determining the differential efficiency and the threshold current for multi-quantum well lasers. Expressions for the differential efficiency and threshold current are obtained from the steady state solutions of the basic laser rate equations. As examples, plots of the optical power as a function of the injected current are presented for lasers with various mirror reflectivities.

A. INTRODUCTION

A set of coupled, nonlinear, differential equations has been widely used³⁻⁵ to explain the transient and steady state properties of semiconductor lasers. However, the importance of optical losses in the cavity is sometimes overlooked. The threshold current will decrease while the differential efficiency can either increase or decrease with improving mirror quality depending on the relative amounts of optical loss due to the mirror transmissivity, scattering and diffraction. This technical memo develops expressions for the differential efficiency and threshold current from steady state solutions of the basic laser equations. The expressions are compared with plots of the experimentally measured emitted optical power (L) as a function of the laser pump current (I).

B. MODEL

The simplest phenomenological model for semiconductor lasers can be expressed by the following two equations:³⁻⁵

$$\frac{dn}{dt} = -G(n)\gamma + J - s n^2 - \frac{n}{A} \quad (2.1)$$

$$\frac{d\gamma}{dt} = G(n)\gamma - \frac{\gamma}{D} + \beta s n^2 \quad (2.2)$$

The quantity $n(t)$ is the electron density ($1/\text{cm}^3$). The hole density and electron density are the same in this model. $\gamma(t)$ is the photon density ($1/\text{cm}^3$). J is the electron pump rate which is approximately related to the current I through the electronic charge e and the volume of the active region V_a by $I = eV_a J$. The parameter s is the coefficient for spontaneous emission. A is the electron recombination lifetime. The cavity lifetime D includes the effects of optical losses capable of being modeled through the use of time

constants D_i such that $1/D = \sum (1/D_i)$. The confinement factor β accounts for the portion of the spontaneous emission which couples into the waveguide and stimulates emission at the lasing wavelength.

$G(n)$ in equations 2.1 and 2.2 is the well known intrinsic gain for stimulated emission and stimulated absorption. For high carrier densities, additional injected carriers tend to fill energy levels which do not contribute to the gain for stimulated emission. Thus the differential gain (dG/dn) must decrease with increasing n . $G(n)$ is described by

$$G(n) = \frac{g_0}{n_s} \frac{n - n_0}{1 + \frac{n - n_0}{n_s}} \quad (2.3)$$

and it is graphed in figure 2.1. The quantity n_0 , the transparency density, is the value of the electron density for which the gain medium becomes transparent and the intrinsic gain exactly compensates the intrinsic losses. The saturation density, n_s , is the point where the curve rolls over and passes through $g_0/2$. The gain constant g_0 is the maximum coupling between the photons and carriers.

The function $G(n)$ characterizes the gain medium – positive values correspond to gain and negative values signify absorption. For cavities with both gain and saturable absorber sections, models include equation 2.3 to predict hysteresis in the L-I curves^{6,7} or mode locking.⁸ Some models, however, approximate the gain G with an equation linear in n . For example, gain-absorber pairs can be modeled by approximating $G(n)$ with a line tangent to $G(n)$ at $n < n_0$ for the saturable absorber and another at $n > n_0$ for the gain section. The linear approximation can be written as

$$G(n) \equiv c_1 n - c_2 \quad (2.4)$$

where, for the approximation at n_0 , $c_1 = g_0/n_s$ and $c_2 = n_0 g_0/n_s$.

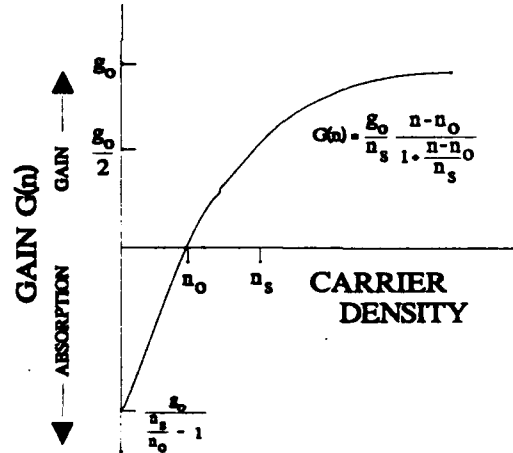


Figure 2.1: Intrinsic Gain versus Carrier Density

Typically, the L-I curves are obtained from semiconductor lasers which are pulsed on the order of a few tenths microsecond to avoid heating problems. However, the transient response of the laser lasts for a period of time on the order of several time constants which characterize the optical cavity -- a few nanoseconds at most. Thus, on the time scale required for an L-I curve, each point on the curve represents the steady state solution for the photon and carrier densities at a fixed value of injected current ($dn/dt = 0$ and $dy/dt = 0$). The spontaneous emission term in equation 2.2 is primarily responsible for initiating laser oscillation in the cavity; however, the term can be neglected once oscillation commences. As a result, for currents above threshold, equation 2.2 yields

$$G(n') = \frac{1}{D} \quad (2.5)$$

where n' , the value of n which satisfies equation 2.5, is

$$n' = \frac{n_s}{D g_0 - 1} + n_0 \quad \text{for exact } G(n) \quad (2.6a)$$

$$n' = \frac{c_2 + \frac{1}{D}}{c_1} \quad \text{for approx. } G(n) \quad (2.6b)$$

Equation 2.5 shows that, independent of the pump current, the net intrinsic gain above threshold just compensates for the optical losses, described by D , and that the value of n is "pinned" to n' . If the value of $n(t)$ should momentarily exceed n' then (1) dy/dt in equation 2.2 becomes a positive number, (2) $\gamma(t)$ increases in equation 2.1, (3) dn/dt becomes negative and (4) $n(t)$ is returned to its steady-state value; similar considerations hold for a momentary drop in $n(t)$. Thus equations 2.1 and 2.2 have a feedback mechanism for n built into them. Also note that a decrease in the optical loss, which means an increase in D , leads to a decrease in the carrier density necessary to achieve and maintain laser oscillation. The carrier density tends toward the transparency density as the optical loss is reduced.

The differential efficiency (dL/dI) and threshold current can be obtained from equation 2.1 with the results of equations 2.5 and 2.6 and $dn/dt = 0$. With these substitutions, equation 2.1 becomes

$$\gamma = D (J - J_{thr}) \quad (2.7)$$

where the differential efficiency is related to D , the threshold current is $I_{thr} = eV_a J_{thr}$ and the threshold pumping rate J_{thr} is given by

$$J_{thr} = s \left(n_0 + \frac{n_s}{D g_0 - 1} \right)^2 + \frac{1}{A} \left(n_0 + \frac{n_s}{D g_0 - 1} \right) \quad \text{for the exact } G(n) \quad (2.8a)$$

$$J_{thr} = s \left(\frac{c_2 + \frac{1}{D}}{c_1} \right)^2 + \frac{1}{A} \left(\frac{c_2 + \frac{1}{D}}{c_1} \right) \quad \text{for the approx. } G(n) \quad (2.8b)$$

Thus, the $\gamma(J)$ curve is linear for currents larger than the threshold current.

The predicted behavior of the differential efficiency and threshold current as functions of the reflectivity are very sensitive to the functional form of the relation between the mirror reflectivity and the optical loss at the mirrors. The cavity loss term in the laser equations becomes nonlinear for the exact relation but remains simple when the cavity loss term involves a cavity lifetime constant as does equation 2.2. The relation for the cavity lifetime can be written as $1/D = 1/D_m + 1/D_r$ where D_m , the mirror time constant, is the portion of the cavity lifetime attributable to the mirrors and D_r accounts for optical scattering and diffraction. Relations in appendices A and B permit rewriting the mirror time constant, the photon density and the pump rate in terms of the mirror reflectivity R , the optical flux L and the current I respectively. With the relation between J and I and relations 2A1 and 2B1, equations 2.7 can be written as:

$$L = v_g h \frac{c}{\lambda} \frac{1}{2eL_c} (1-R) D (I - I_{thr}) \quad (2.9)$$

where the cavity length has been inserted for the ratio of the volume of the active region V_a to the approximate cross sectional area of the beam A_b , $L_c \equiv V_a/A_b$, and the differential efficiency is given by

$$DE = v_g h \frac{c}{\lambda} \frac{1}{2eL_c} (1-R) D \quad (2.10)$$

Similarly, equation 2.8 can be rewritten to yield the threshold current

$$I_{thr} = s e V_a \left(n_0 + \frac{n_s}{D g_0 - 1} \right)^2 + \frac{e V_a}{A} \left(n_0 + \frac{n_s}{D g_0 - 1} \right) \quad \text{for the exact } G(n) \quad (2.11a)$$

$$I_{thr} = s e V_a \left(\frac{c_2 + \frac{1}{D}}{c_1} \right)^2 + \frac{e V_a}{A} \left(\frac{c_2 + \frac{1}{D}}{c_1} \right) \quad \text{for the approx. } G(n) \quad (2.11b)$$

The second term in equations 2.11 can be neglected in many cases of interest.

The optical loss of the cavity determines both the differential efficiency and the threshold current. As previously mentioned, the cavity lifetime can be attributed to the mirror lifetime D_m and to those other losses which can be expressed by the lifetime D_r such as optical scattering. If the loss term D_r were not present in the expression for D then increasing the mirror reflectivity would result in decreasing threshold and increasing differential gain. This behavior can be

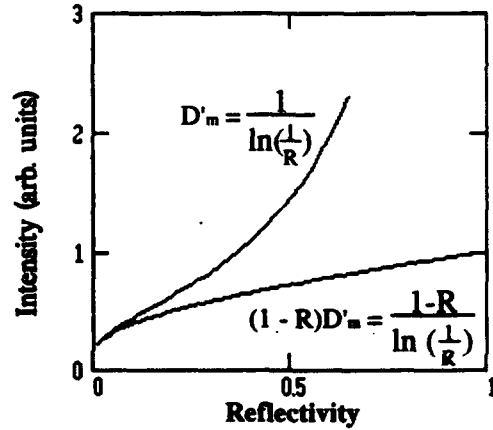


Figure 2.2: Intensity vs. Reflectivity. Flux inside the cavity (top curve) and the flux emitted from a facet (bottom) for a laser with only mirror losses.

understood as follows. Without the D_r loss in the cavity, the photon density in the cavity would rapidly increase without bound -- faster than $(1-R)^{-1}$ -- as the reflectivity increases (top curve in figure 2.2). In fact, at a fixed current, the emitted flux would increase in proportion to $(1-R) D_m$ as would be given by equation 2.10 (bottom curve in figure 2.2). With the additional loss D_r in the cavity, the rate of increase of the photon density in the cavity will eventually be limited by that loss as the mirror quality improves. The increase in the photon density in the cavity will be slower

than $(1-R)^{-1}$ and the emitted flux will decrease. Figure 2.3 shows this behavior as a family of plots of $(1-R)D'$ where $1/D' = 1/D'_m + 1/D'_r$ and the primes indicate that the factor (L_c / v_g) has been factored out for convenience (for example, $D_r = D'_r L_c / v_g$). Thus the differential efficiency depends on the relative amounts of optical loss due to the mirrors and D'_r . For values of D'_r near 0.3, the differential efficiency monotonically decreases for reflectivities larger than 0.1 and, for relatively low loss, such as $D'_r = 100$, the differential efficiency rises until the reflectivity is made close to unity.

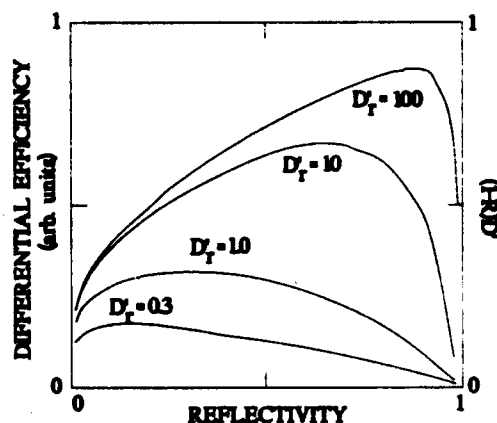


Figure 2.3: Predicted differential Efficiency and $(1-R)D'$ for lasers with optical loss time constants attributable to mirror transmissivity, optical scattering and diffraction.

The threshold current is primarily determined by the optical losses as shown in equation 2.11. However, an increase in the reflectivity of the mirrors always leads to a decrease of the threshold current. The factor $1/D$ in Equation 2.1b, for example, is graphed in figure 2.4 after renormalizing D , D_m and D_r by (L_c / v_g) . The threshold current can never be made lower than $seV_a n_o^2 + eV_a n_o / A$ by reducing the optical loss. The first

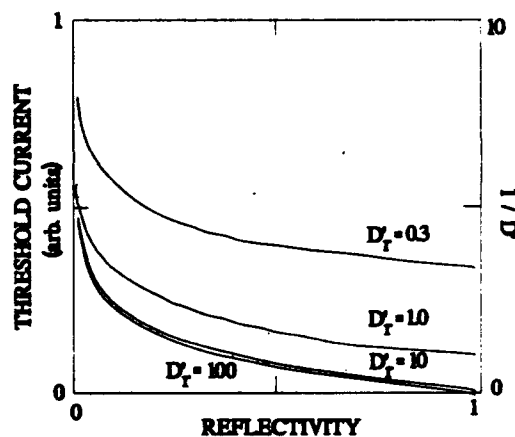


Figure 2.4: Threshold Current and $1/D'$.

term is related to the efficiency of spontaneous emission to start the stimulated emission. The second term is the current necessary to replenish the carrier population as it is being reduced by recombination.

The above model was applied to lasers with Total Internally Reflecting (TIR) mirrors (figure 2.5).⁹⁻¹¹ The lasers were made from graded index, GaAs-AlGaAs quantum well heterostructures with 5 wells; they were about $85 \times 10 \mu\text{m}$ in size. The mirrors and ridge

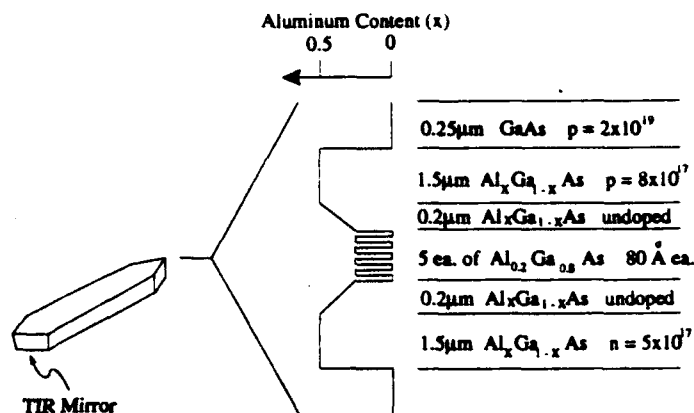


Figure 2.5: Quantum Well Laser with Total Internally Reflecting Mirrors

waveguides were etched in a Chemically Assisted Ion Beam Etcher (CAIBE). The lasers emitted near 860 nm. The quality of the mirrors varied across the wafer surface and three of them, with widely varying reflectivities, were chosen as examples.

Typical L-I curves appear in figure 2.6. These curves were taken with the experimental setup shown in the inset to figure 2.6. The pulse generator produced 5 μsec wide pulses, separated by 2 msec. The pulse itself was the positive portion of a sine wave. The voltage was applied to the series combination of the main laser

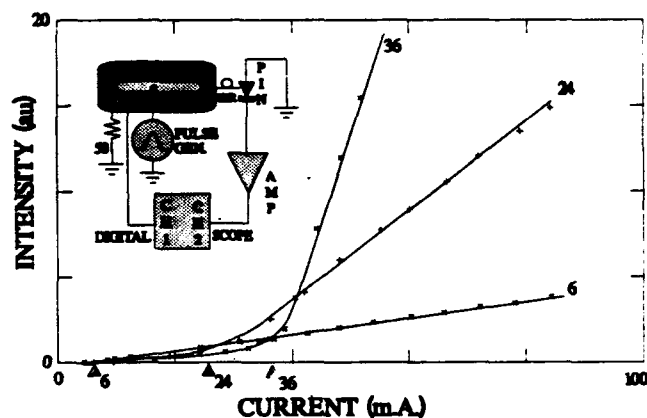


Figure 2.6: Experimental L-I Curves. The inset shows the experimental setup.

and a 50Ω sampling resistor which were joined at the bottom N^+ contact. This resistor yielded a voltage drop proportional to the current through the laser. A single mode fiber, with one end positioned next to a facet of the main laser, routed the illumination to a pin photodiode circuit. A digital oscilloscope plotted the pin photodiode signal versus the signal from the 50Ω resistor. Threshold currents as low as 6 mA were observed.

The L-I curves in figure 2.6 exhibit decreasing differential efficiency and decreasing differential gain for increasing mirror reflectivity. The reflectivity of the TIR mirrors exceeds the 34% maximum intrinsic reflectivity of cleaved or etched mirrors. In the range of interest, $R > 0.34$, the predicted differential

efficiency decreases for values of D'_r less than about 2 as shown in figure 2.3. Thus the observed decreasing differential efficiency suggests that D'_r has a value of about 2 or less. For a reflectivity of 0.4, D'_m is about unity as shown by the top curve in figure 2.2. Thus D' has the value of 2/3 which scales to 0.8 picoseconds when the factor of L_c/v_g is included. The values used in equations 2.9 and 2.10 are $L_c=0.85 \mu\text{m}$, $v_g = 0.8 \times 10^{10} \text{ cm/s}$ and $\lambda = 860 \text{ nm}$. Equation 2.10 reduces to

$$DE = 1.7 (1-R) D' \quad (\text{both mirrors}) \quad (2.12)$$

where the factor of 2 in equation 2.10 was removed to include the light emitted from both mirrors and D' has the units of L_c/v_g . For the values given, the differential efficiency is about 0.7 mW/mA. For a differential efficiency on the order of 0.1 mW/mA as for the bottom L-I curve in figure 2.6, the mirror reflectivity would be on the order of 95%.

C. CONCLUSIONS

The optical power as a function of the injected current was presented for multi-quantum well lasers with various mirror reflectivities. This technical memorandum stressed the importance of optical losses in the cavity for determining the differential efficiency and the threshold current. The differential equations for the model and the corresponding steady state solutions were presented. The results show that both the differential efficiency and the threshold current decrease with reflectivity near unity.

The predicted behavior of the differential efficiency and threshold current as functions of the reflectivity are very sensitive to the functional form of the relation between the mirror reflectivity and the optical loss. The cavity loss term in the laser equations becomes nonlinear for the exact relation but remains simple when the cavity loss term involves a cavity lifetime constant as does equation 2.2. An approximation to the relation between the reflectivity and the lifetime, denoted by $D_m(R)$, obtains by calculating the energy remaining in the cavity at end of each trip of the energy across the cavity; this calculation places an $\ln(1/R)$ term in $D_m(R)$. A second approximation obtains by applying the equation of continuity to the energy in the cavity and the optical flux through the mirrors; the same results can be obtained from a Taylor series expansion for the $\ln(1/R)$ term in the first approximation for reflectivities

near unity ($\ln(1/R) \cong 1-R$ for $R \cong 1$). These two approximations bound the exact relation. As the mirror quality improves, the first approximation yields a decreasing threshold current and either an increasing or decreasing differential efficiency depending on the relative magnitudes of the loss due to the mirrors, scattering and diffraction. The second approximation results in a differential efficiency and threshold current that monotonically decrease throughout the range of R .

The two approximate relations for $D_m(R)$ can be compared to obtain a better prediction for the differential efficiency. The first approximation breaks down for reflectivities smaller than about 0.1 which explains the sharp decrease in the differential efficiency below 0.1 in figure 2.3. For reflectivities larger than 0.35, the approximation is well within 5% and improves for better mirrors. Thus, the differential efficiency is primarily determined by the relative magnitudes of the loss attributable to the mirrors, optical scattering and diffraction. These same quantities, along with the current to achieve transparency and the current necessary to replace carriers lost to nonradiative recombination, determine the threshold current.

III. FABRICATION OF RIDGE WAVEGUIDED PHOTONIC CIRCUITS WITH CHEMICALLY ASSISTED ION BEAM ETCHING

A. INTRODUCTION

Discrete GaAs-AlGaAs laser diodes have already proven to be highly useful and commercially viable photonic devices. The next logical step in the evolution of this family of devices is the monolithic integration of photonic devices based on a laser diode heterostructure. The standard optical waveguide structure used to confine and amplify light within a diode laser can also be used as a saturable absorber¹¹, electro-optic modulator¹², detector¹³, and passive waveguide¹⁴. Applications range from Q switched and bistable lasers to optical switching and optical logic. This paper reviews the processing techniques used to fabricate laser based logic devices comprised of Chemically Assisted Ion Beam Etched (CAIBE) waveguides and mirrors.¹⁵⁻¹⁷ A brief discussion of principles of guiding within an etched ridge waveguide will precede a chronology of the processing steps.

B. ETCHED RIDGE WAVEGUIDES

In order for monolithically integrated optical devices to function, light must be routed to, and confined in each device in accordance with the over all "photonic circuit." The photonic circuits whose fabrication is described in this chapter use etched ridge waveguides for both of these requirements. Etched ridge waveguides use index guiding to confine light in the vertical direction and "strip loading" to confine light in the lateral direction. In both cases, light is confined by having, at some distance from the center of the waveguide, a purely imaginary phase constant in the direction normal to the direction of propagation. By definition, this creates an exponential decay of intensity with distance from the center of the guide. This exponential decay is the result of light traveling in phase, along the boundary between a region experiencing a high index of refraction (the core) and a region with a lower index of refraction (the cladding). Since the wave equation for light dictates that the square of the magnitude of the phase constant vector for light traveling in a given material equals the square of the product of the index of refraction and the free space propagation constant,

$$B_x^2 + B_y^2 + B_z^2 = (nk_0)^2 \quad (3.1)$$

it follows that, in order for light traveling in both the core and cladding to be constantly in phase ($B_{z,\text{core}} = B_{z,\text{cladding}}$), the phase constants in the directions normal to propagation must be real in the higher index core and imaginary in the lower index cladding. A standard laser heterostructure confines light in the vertical direction in this manner by using planar epitaxially grown layers of varying index of refraction. The strip loading in an etched ridge laser is formed by etching down to just above the planar core on either side of the waveguide. This produces the equivalent of a slight lateral index drop in the side regions by lowering the phase constant of their possible vertical modes.¹⁸ This is more desirable than etching all the way through the core because the smaller index drop allows for wider, and therefore easier to fabricate, single mode lasers.

C. PROCESSING

The laser logic devices being fabricated requires etched regions of two different depths: a deep etch that extends well into the lower cladding region for the laser mirrors, and a shallow etch to delineate the waveguides. In order to create an effective lateral index difference, the shallow etch should be within 100 nm of the top of the planar waveguide core.¹⁹ Both etch depths can be achieved with a single etch by depositing a material which etches slowly in the CAIBE over the shallow etch regions.¹⁶ When this material is totally etched away, the previously uncovered deep etch regions will have already etched down to the difference between the two etch depths. A single layer of SiO_2 can be used as both the etch retarding layer and insulation between the contact pads and the semiconductor. Chromium, whose etch rate in the CAIBE is almost negligible, is used to mask region which require no etching. These regions correspond to the regions to be metallized, namely the Ohmic contacts on top of the waveguides and the electrical contact pads. For this reason the chromium etch mask is delineated at the same time as the p-type Ohmic contact metallization. The entire process requires only two photolithographic mask steps. A chronology of the design and processing steps are as follows:

1. The masks used to delineate the SiO_2 and the metallization are laid out on a CAD system.
2. The photolithographic masks are generated using a Mann 360F Pattern Generator.
3. The laser heterostructure wafers (see figure 3.1), along with blank GaAs substrates are cleaned and dried. SiO_2 is grown on the wafers. The desired thickness of the SiO_2 is determined by the etch rate of both SiO_2 and GaAs / AlGaAs in the CAIBE by the following equation:

$$T_{\text{SiO}_2} = R_{\text{SiO}_2} (D / R_{\text{GaAs}}), \quad (3.2)$$

where R_{SiO_2} is the SiO_2 etch rate, R_{GaAs} is the average heterostructure etch rate, and D is the difference in etch depths.

4. Photoresist is spun on and the first mask pattern is transferred onto the wafers, leaving exposed the areas which are to be deep etched or Ohmically contacted.
5. The wafers are placed in a reactive ion etcher and the SiO_2 in the exposed areas is etched away, using a CHF_3 plasma. While still in the reactive ion etcher, the Photoresist is removed with an oxygen plasma (see figure 3.2a).
6. In order to improve the Ohmic contact, a shallow Zn diffusion is used to dope the contact regions P^+ . ZnAs_3 is used to form a Zn vapor source during an open ampule diffusion, lasting 9 minutes at 650°C . The patterned SiO_2 on the wafers insure that only the areas to be p-contacted are doped P^+ . Since the diffusion is shallow (about 300 nm), the Zn diffusion in the regions to be deep etched is without consequence to the final device.
7. After the diffusion, a new layer of 5214 photoresist is spun on the wafers and the metallization pattern is transferred to the photoresist. Using the negative reversal process for 5214, the areas to be metallized are left uncovered.
8. A standard GaAs p-type Ohmic contact metallization, followed by 100 nm of chromium, is evaporated onto the sample. The pre-alloyed Ohmic contact metallization consisted of 20 nm of titanium, 20 nm of platinum, and 200 nm of gold.
9. Soaking in acetone lifts off the metallization in the regions to be etched (see figure 3.2b).

10. The wafers are dry etched in the CAIBE, with blank GaAs substrates being used for calibration runs to verify etch rates (see figure 3.2c).

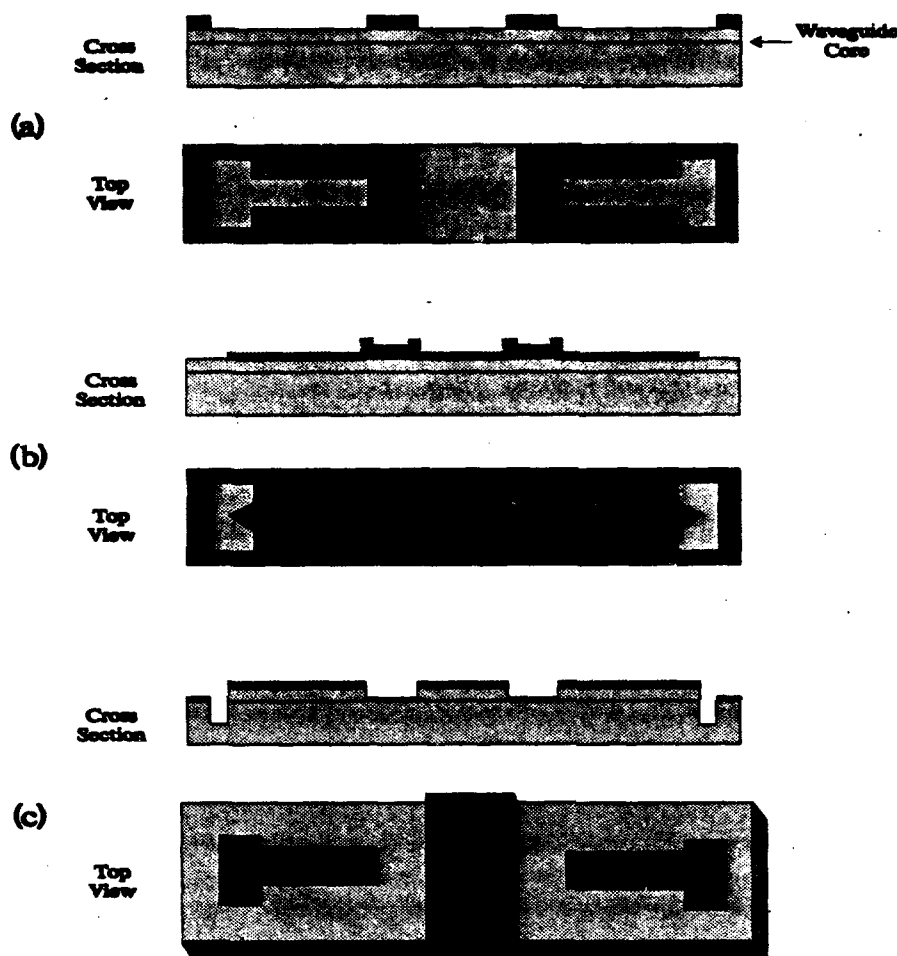


Figure 3.2: Cross sections and top views of two intersecting laser cavities during progressive stages in fabrication: (a) After the patterning of the SiO₂ etch retarding mask, (b) After the patterning of the Ohmic contact metallization / chrome etch mask, and (c) after etching in the CAIBE.

11. Using 3 micron AlO₃ grit, the backs of the wafers are then lapped down such that the final wafer thickness is approximately 150 microns.

12. The samples are cleaned and dried. A standard n-type Ohmic contact metallization is evaporated on the backs of the wafers (10 nm of nickel, 40 nm of germanium, 80 nm of gold, 50 nm of silver, and 80 nm of gold).

13. The wafers are then placed in an alloying oven at 360 °C for 60 seconds in order to alloy the Ohmic contacts.

14. The wafers are now ready to be cleaved and tested. Even with etched laser mirrors, cleaving may be required in order to access the optical output. Figure 3.3 shows a scanning electron micrograph of a completed device.

Discussions of the test methods used as well as the design and testing of specific photonic circuits have been published separately.^{10,11}

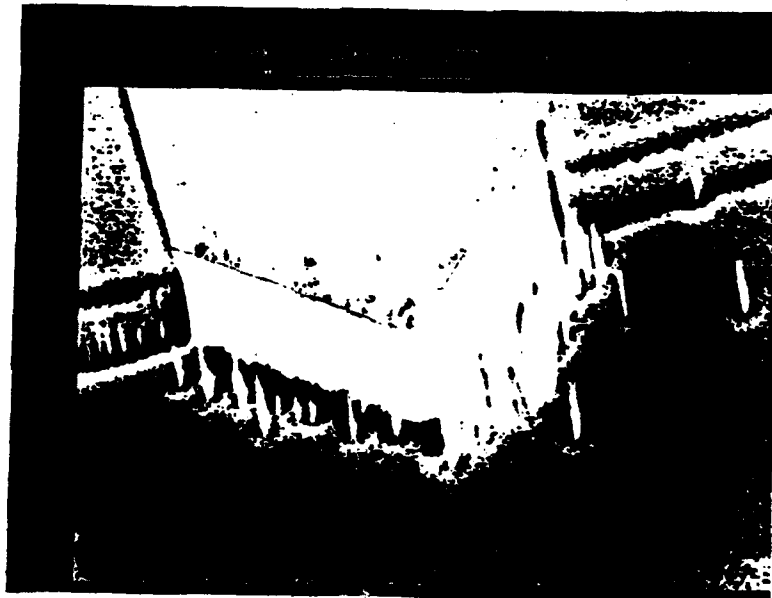


Figure 3.3 A total reflection mirror at the end of an etched ridge waveguide, as seen by a scanning electron microscope. The unintentional tree-like structures in the deeply etched region do not effect the performance of the mirror.

D. CONCLUSIONS

Photonic circuits utilizing etched ridge waveguides in conjunction with deep etched mirrors can be fabricated in a self aligned process which avoids photolithography on previously etched substrates. This is accomplished by using an etch retarding mask to facilitate two etch depths during a single run in the CAIBE. Since the contact metallization and the unetched region coincide, only two photolithography masks are needed for this process.

IV. P⁺ ELECTRICAL CONTACTS ON GaAs

This chapter discusses the physics and engineering of semiconductor electrical contacts and the importance of low resistance Ohmic contacts for the best performance from electronic devices. A simple method is used to deduce the resistance of the electrical contacts and the bulk semiconductor. The fabrication process for P⁺ GaAs contacts is discussed. Test results are presented for the resistance of the metal electrodes, P⁺ GaAs bulk, the intrinsic contact resistance and the temperature dependence of the metal and P⁺ GaAs. The distributed impedance of the contact structure for semiconductor lasers is discussed.

A. INTRODUCTION

Electrical contacts have been studied since the middle of the last century.^{20,21} Since the late 1940's, industry has utilized the properties of electrical contacts to realize semiconductor components such as high speed Schottky diodes and integrated electro-optic circuits. Electrical contacts are the most basic and, at the same time, one of the most important parts of modern integrated circuitry.

Electronic and electro-optic devices, which do not require the diode properties of a metal-semiconductor interface, are usually given Ohmic, low resistance electrical contacts; without this type of contact, the performance of the device would be linked to the properties of the contact itself. Ohmic electrical contacts have linear current-voltage (I-V) characteristics by definition; this permits the device characteristics to be observed independently of the contact characteristics. The contacts should generally have low intrinsic resistance to improve the performance of the device. Specifically, lowered contact resistance increases the device bandwidth and decreases both the noise figure and the power dissipation. Under the appropriate conditions, a device with Ohmic contacts can still have a transient response which is dominated by the depletion or accumulation region at the metal-semiconductor interface.²²⁻²⁵

The Ohmic properties of the contact are a result of thermionic field emission at the metal - semiconductor interface.²¹ Thermionic field emission occurs at the metal - semiconductor interface for narrow or small energy barriers presented by bent conduction or valence bands; the width of these barriers can be controlled with high levels of doping. Generally, the conditions of the surface of a semiconductor determine the shape of the conduction and valence bands near the surface. Surface states can *pin* the

Fermi energy level in the semiconductor to a given value. In this case, the width and height of the barrier is determined by the relative magnitudes of the density of states at the surface and the density of donor or acceptor states in the bulk. Metal evaporated onto a surface with a high number of surface states will have little affect on the band bending. However, the width and height of the barrier in a semiconductor with few surface states is directly related to the work function of the metal evaporated onto the surface. The width of the barrier can be reduced to enhance tunneling (field emission) by heavily doping the semiconductor near the surface. Carriers can surmount the barriers (thermionic emission) or tunnel through narrow parts of it at higher energies by absorbing phonons from the lattice. Generally, field emission is used to provide Ohmic contacts but thermionic emission has been used in recent heterostructure materials where the band discontinuities at the interfaces have been lowered by band gap engineering.²⁶

Semiconductor devices such as PIN photodiodes, transistors and lasers, have diode-like structures and therefore use both N^- and P^+ Ohmic contacts. The type of contact determines the processing steps and the type and number of metals evaporated onto the wafer. The high doping levels can be achieved in several ways. The dopants can be placed into the substrate during an MBE growth phase, they can be diffused into the substrate in a high temperature oven or they can be included as a layer of metal and then diffused into the substrate during a subsequent alloying step. The P^+ contacts on GaAs discussed in this technical memorandum use the second method with zinc as the dopant. Consideration must be given to the adhesive properties between the metal and the substrate. Some metals such as titanium or chrome adhere better than others and are therefore evaporated onto the substrate first. The first layer of metal on GaAs for P^+ contacts consists of titanium; chrome should not be used for this purpose with GaAs since it produces deep traps. The second layer consists of platinum which provides a diffusion barrier between a top gold layer and the GaAs wafer. An N^- contact has a top layer of gold to getter the Ga out of the substrate so that Ge from one of the metal layers can substitute at the resulting vacant lattice sites in the GaAs to serve as a dopant. The gold layer on the P^+ contacts provides a highly conductive layer so that the metal will have the lowest possible resistance and be immune to corrosion. After the metals have been evaporated

onto the surface, the wafer is alloyed to diffuse any metal dopants into the substrate and to activate those dopants.

The remainder of this technical memorandum discusses the basic circuit model for the contact, the fabrication process, the experimental data and the author's interpretation of the data. An appendix contains a distributed impedance model for the effective resistance of an electrode structure similar to that used for semiconductor lasers.

B. BASIC CIRCUIT MODEL

The simplest model defines a contact resistance R_c and bulk GaAs resistance R_b .²⁰ The contact resistance occurs at the MS interface as a result of the energy barrier there. The resistance of a metal electrode R_m becomes important when it is comparable in value with the resistance of the bulk semiconductor. As is well known, Schottky barriers have both resistive and reactive components; thus, for the general case, the response of the electrical contact depends on the frequency content of the drive signal. For low frequency work, the reactive component of the contact is negligible. The inset to figure 4.1 shows the low frequency model.

The values of the contact and bulk resistance can be determined by use of an appropriate test structure. One of the simplest geometries consist of a series of metal electrodes evaporated onto the GaAs. In one case, the electrodes are placed at regular intervals along the length of the GaAs wafer. In another case, the distance separating two adjacent electrodes D_i changes along the length of the wafer. For either case, assuming that the contacts are uniformly

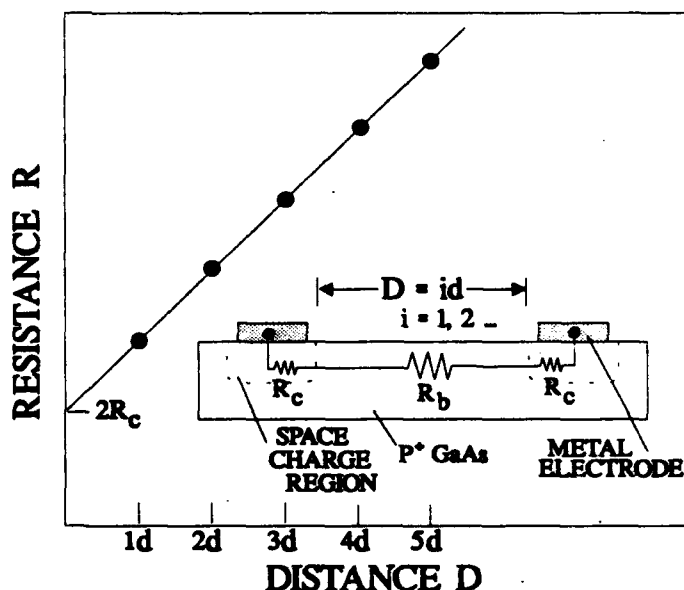


Figure 4.1: The expected plot of resistance between two metal electrodes as a function of separation between the pads. The intercept of the straight line with the resistance axis yields $2R_c$ and the slope of the line yields the bulk resistance. The inset shows the low frequency model. The electrodes are spaced by $D=id$ where i is an integer.

fabricated across the surface of the sample, the plot of the total resistance R as a function of the separation distance D is a straight line. The total resistance between the pads is defined by

$$R = 2R_c + \frac{D}{d} R_b \quad (4.1)$$

where D is the distance separating two adjacent electrodes, d is the smallest such distance for a given contact geometry and R_b is the bulk resistance corresponding to the distance d . The intercept of the line with the resistance axis is $2R_c$ and the slope is R_b/d . The space charge region can give rise to photocurrents when illuminated which can be modeled by a current source in parallel with the contact impedance. In addition, the GaAs can exhibit a photoconductive response. Photocurrents originating in the space charge region produce a non-linearity in the I-V curves at low applied voltages if they are not specifically taken into account. The photoconductive response changes the slope of the I-V curves. The experiments reported here were performed in the dark and the photocurrents were determined to be negligible.

The electrical contact can be represented accurately as a transmission line.²⁰ Such an approach models the resistance and capacitance as a distributed impedance. Generally, the metallization is assumed to have negligible resistance for the calculations. A distributed impedance model can also be used to explain results obtained from certain electrode geometries as discussed in the appendix. Single mode semiconductor lasers generally have long, narrow electrodes on one side of the wafer and a large area, low resistance electrode on the other side which carries the current common to all of the devices on the wafer. The narrow electrodes can have resistance on the same order of magnitude as the laser. The voltage drop along these narrow electrodes can be significant at high currents and, as demonstrated in the appendix, this voltage drop is nonlinear with distance along the electrode. Such a voltage drop would result in uneven pumping of a laser cavity. Thus, the distributed impedance of the contact, the metal and the semiconductor are important to the operation of semiconductor lasers, laser amplifiers and laser based optical logic gates.

C. FABRICATION

The contacts were fabricated on an n-type GaAs wafer so that each P⁺ doped region, a resistive element, can be positioned in the potential well of a reversed biased diode. During the test phase, the current flow is confined to a narrow channel between the pads by reverse biasing the contact structure with respect to the substrate. However, with sufficiently high doping levels, leakage current from the doped region to the substrate is generally negligible. The following outlines the fabrication process used to produce the contact structures for this study.

(1) The wafer surfaces were cleaned with a camel hair brush and liquid Ivory dish soap and rinsed in DI water. The wafer was dipped in Acetone, Methanol, Isopropanol and DI water to remove grease and residues from the surface. A solution of Ammonium Hydroxide and DI water, in the ratio of 1:15, was used to remove organics from the surface and to perform a slight etch on the surface oxides.

(2) A 1500 angstrom thick layer of SiO₂ was deposited over the wafer surface in a Plasma Enhanced Chemical Vapor Deposition (PECVD) system at 250 °C to provide (i) a diffusion mask for the subsequent processing step and (ii) electrical isolation for the finished device. The glass layer was patterned in a Reactive Ion Etcher (RIE) with CHF₃ gas; the mask for this process consisted of a patterned Shipley 1400-27 photoresist layer. After patterning the SiO₂ layer, an oxygen plasma was used to remove the remaining photoresist.

(3) Regions of the n-type GaAs, as defined by the openings in the SiO₂, were doped p-type by a Zinc diffusion process. The Zinc was diffused to a depth of 0.7 μm during a 1/2 hour bake at 650 °C in a diffusion oven.

(4) The metal electrodes were defined by photolithography. The metal was evaporated in an electron beam evaporator and then a lift off process produced the desired electrode pattern. A standard photoresist lift off process was unsuitable for use with

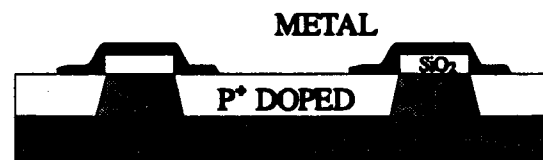


Figure 4.2: The layered structure of the electrodes.

the available electron beam evaporator. Heat transferred from the evaporated metal to the photoresist would have hardened the photoresist and made it difficult to remove. Instead, a One Step Two Level Etch

process was used.¹⁶ Layers of polyimide and SiO_2 were deposited across the surface. The first layer, polyimide, was spun on at 5K RPM, baked at 80 °C for 30 minutes and then baked at 150 °C for an additional 30 minutes as per the manufacture's specifications. Next, a glass layer was deposited to a thickness of 800 angstroms in the PECVD system at a temperature of 150 °C; the lower deposition temperature prevented the polyimide from becoming impervious to solvents. A patterned photoresist layer was used as an etch mask for the glass which was etched in CHF_3 in the RIE. The patterned glass layer served as the etch mask for the polyimide. An oxygen plasma etched the polyimide and the remaining photoresist. After the metal was evaporated across the wafer surface, the wafer was dipped into methylene chloride which caused the polyimide to lift off both the glass and the unwanted metal.

(5) The metal layer consisted of three metals. A 1500 angstrom Au layer was deposited on top of a 200 angstrom Pt layer which was on top of a 200 angstrom layer of Ti. Later, the metal contacts were alloyed at 360 °C for 3 minutes in a hydrogen atmosphere. The basic electrode structure appears in figure 4.2.

The geometry of the contacts appears in figure 4.3. The nomenclature is as follows. The resistive element between the pads is either Metal M or P^+ GaAs G . The length of the resistive elements is either fixed or Variable V across the wafer. In the case of a fixed length, the last several digits in the structure name represents the distance in microns. In the variable cases, the last two digits give the minimum separation in microns. The column D_i gives the length of the resistive elements in units of microns for each integer i . The figure contains the dimensions of the pads and the amount of overlap of the pad and the GaAs resistive elements.

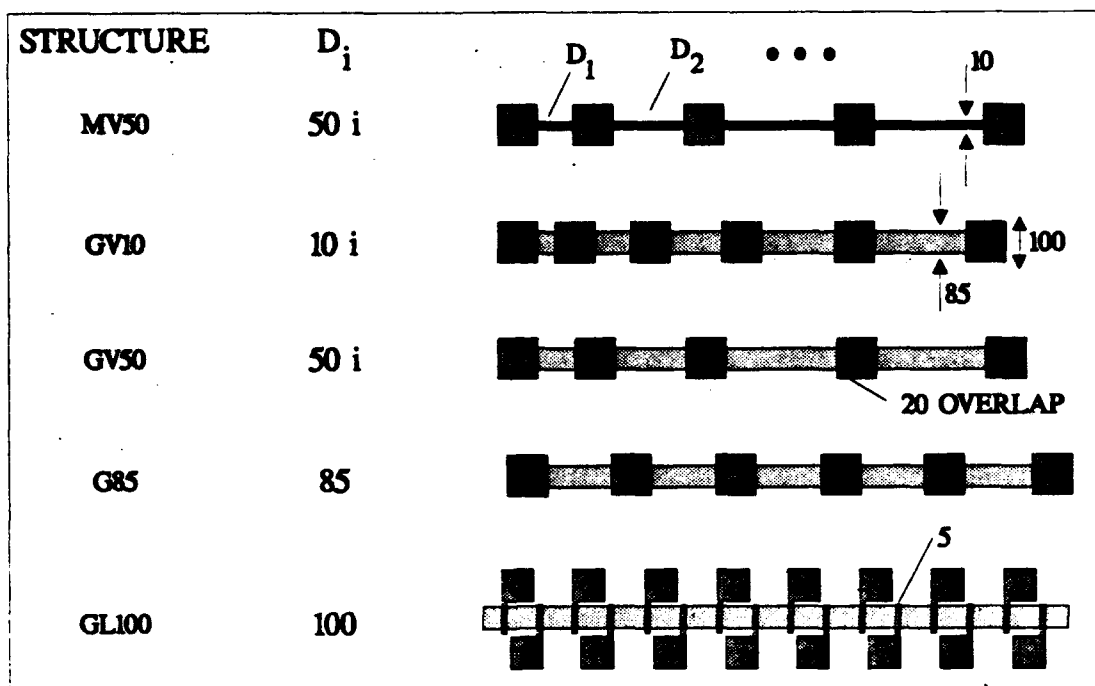


Figure 4.3: The geometry of the contacts fabricated to determine contact resistance. The distances D_i are in microns where i is an integer. The top set, MV50, has metal for the resistive element and a variable distance separating the pads. The remaining sets have P^+ GaAs as the resistive elements between the pads. The bottom set is the laser-like structure discussed in the text in conjunction with distributed impedance.

D. EXPERIMENTAL

The resistances were determined with Keithley digital multimeters by measuring both the voltage applied to the contact structure and the resulting current; for low current levels, a low noise current amplifier was added to the experimental setup. The I-V curves were

determined for 6 decades of current with this arrangement. Tungsten and copper probe tips were used to provide the bias to the pads. The

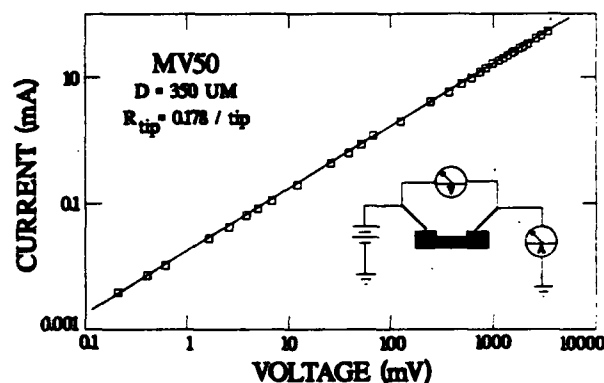


Figure 4.4: Typical plot of current versus voltage for the contact structures. The above graph has the characteristics for the MV50 structure. The probe resistance of 0.356Ω has not been factored out of the data.

on a single large metal pad and then measuring the I-V characteristics. The setup appears in the inset to figure 4.4.

Measurements were made of (1) the I - V characteristics, (2) the resistance as a function of the distance between the pads for a constant current and (3) the temperature dependence of the resistance for metal and the doped GaAs. Typical I-V and R-D plots appear in figures 4.4 and 4.5. For the R-D plots, the current was held constant. The R-D plots generally become nonlinear for large separation distances due to variations in processing across the surface of the

wafer. Measurements were made on the GL100 contact structure to determine the ratio $\Delta V/V_0$, the ratio of the voltage drop along the 85 μm length of metal versus the voltage applied to the two electrodes. Both alloyed and unalloyed contact structures were tested. The tests indicated that (1) the metal had a ratio of resistivity to thickness of $\rho/T = 1.6 \Omega/\square$ independent of the alloying, (2) the G85 style contacts had a resistance $R_c = 1 \Omega$ (or $4 \Omega/\square$) after alloying and a negative value before alloying, and (3) the GL100 contacts had a resistance of 8Ω (or $120 \Omega/\square$), independent of alloying, and values for $\Delta V/V_0$ of 17% and 10% for type 1 structures with an electrode separation distance of $D_1 = 100 \mu\text{m}$ and type 2 structures with an electrode separation distance of $D_1 + D_2 = 200 \mu\text{m}$, respectively. Tests on the G85 style contacts further indicated a value of $29 \Omega/\square$ for the bulk P^+ material. In all cases, the contacts were found to be Ohmic in the range of $1 \mu\text{A}$ to 50 mA . The metal resistance was expected to drop by about an order of magnitude after alloying but it did not do so.

Table 4.1 contains a summary of the resistances obtained from the contact structures. The ratio ρ/T is generally in the range of 30 for the doped GaAs. The contact resistance depends on the amount of overlap between the metal pad and the GaAs. Note the large value of the contact resistance for the GL100

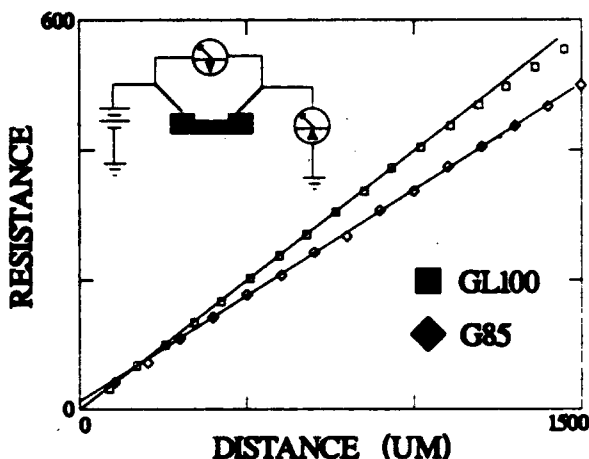


Figure 4.5: Typical plots of resistance vs. distance for the G85 and GL100 contact structures. The current was maintained at mA.

structure. Most of this resistance is attributable to the resistance of the metal in the narrow metal electrode. The effective resistance R_{eff} is related to the contact and bulk resistance by $R_{eff} = 2R_c + R_b$. The GL100 structure has two values for R_{eff} which correspond to two different distances separating the pads. The larger distance corresponds to the situation where an electrode lies between the two current carrying electrodes.

TABLE OF RESISTANCES

TYPE	R_b		R_c		R_{eff}
MV50		1.6 Ω/\square	0		
GV10	3.16	26.7 Ω/\square	3.2	13.6 Ω/\square	9.56
GV50	20.1	34.1 Ω/\square	-0.9		
G85	29.0	29 Ω/\square	1	4 Ω/\square	31
GL100	32.2	27.4 Ω/\square	8	120 Ω/\square	50 / 100 μ 81.5 / 200 μ

TABLE 4.1: Summary of resistances obtained from the R-D graphs. The bulk resistance R_b and contact resistance R_c are listed in Ohms and as the ratio of resistivity to thickness, ρ/T . The bulk resistance in Ohms refers to the resistance of the GaAs for the minimum separation between the electrodes. GL100 has two values for R_{eff} corresponding to pad separations of 100 and 200 μm .

The resistance of metals and highly doped semiconductors increase with temperature. For these materials, there are several contributions to the resistance which includes electron and hole scattering from lattice defects and phonons. Phonon scattering is the most important mechanism for the temperature dependence of the resistivity. As temperature increases, the number of phonons increases and, therefore, the mean free path of the electrons and holes decreases. As a result, the resistance of metals and highly doped semiconductors

increase with temperature. This contrasts with intrinsic semiconductors where the

resistivity decreases with temperature as predicted by the temperature dependence of the Fermi function.

The metal or P^+ GaAs can be used to sense the junction temperature of semiconductor lasers. For this reason, the variation of the metal and P^+ GaAs resistance with temperature was determined. The wafer

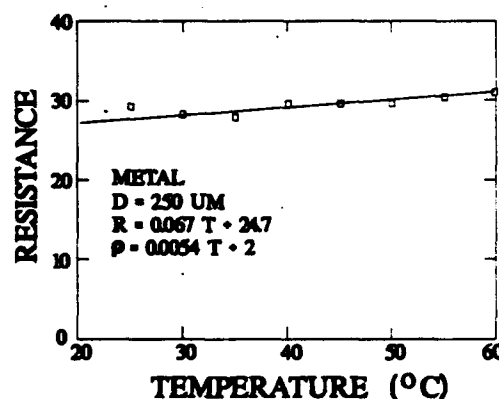


Figure 4.6: Temperature dependence of the resistance for the metal used in the contact structures. The length of the metal was 250 μm and the cross section area was $2 \times 10 \mu\text{m}^2$. The resistivity ρ has units of $\Omega\text{-}\mu\text{m}$.

with the contact structures was mounted on a hot plate to provide control over the temperature of the wafer. Figures 4.6 and 4.7 show the results. Over a range of approximately 40 °C, the resistance of the metal varied by several Ohms while that for the P⁺ GaAs varied by approximately 30 Ω. The inset to the graphs contain the temperature dependence of the resistivity ρ in units of Ω-μm as calculated from the resistance and sample size. The calculation for the resistivity of the P⁺ GaAs used the zinc diffusion depth of 0.7 μm for the thickness.

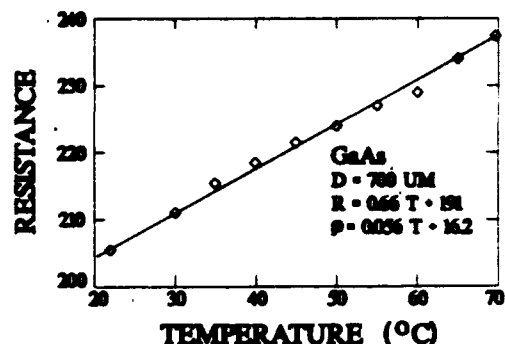


Figure 4.7: Temperature dependence of the resistance for the P⁺ GaAs used in the contact structures. The length of the GaAs was 700 μm and the cross section area was 0.7 x 85 μm². The resistivity ρ has units of Ω-μm.

E. DISCUSSION

The Table of Resistances contains several anomalies. The experimentally determined resistance of the metal is an order of magnitude larger than the value calculated from the thickness and conductivity of the layers. The contact resistance of the GV85 style contacts changed from negative to positive values after alloying. The contact resistance was high for the GL100 style. The experimental values of $\Delta V/V_0$ differ by 15% from those predicted by the distributed impedance models discussed in the appendix.

The anomalies can be explained as follows. The discrepancy between the observed and predicted values of the metal resistivity might be partially attributed to thin film effects and to the fact that probes tend to destroy the electrical pads during testing. The change from negative to positive values for the contact resistance for the G85 style contacts upon alloying can be attributed to changes in the stoichiometry and structure of the metal-semiconductor interface. The experimentally determined values for the contact resistance are quite sensitive to any curvature in the R-D curves which might account for the negative values reported for the contact resistance of the GV50 style. The high resistance for the GL100 contacts is due to (1) the fact that the extrapolation procedure extracts R_c and R_b as if the total distributed impedance could be written as $2R_c + R_b$ instead of the nonlinear expressions obtained in the appendix and to (2) the large value for the resistance of the metal.

The distributed impedance model discussed in the appendix provides some insight into the behavior of the GL100 electrode structure. The set consists of two basic types as shown in figure A1. Adjacent electrodes in the GL100 set are type 1. Two electrodes in the set which are separated by a third electrode are the type 2. Electrodes must be modeled as distributed impedances when the resistance of the metal electrodes is close to that of the semiconductor. For the GL100 set, the resistance of the metal electrode along the direction of current flow is calculated from table 4.1 to be $R_m = 27 \Omega$. The G85 value for R_b , for example, yields the value $R_g = 34 \Omega$ for the resistance of $100 \mu m$ of the GaAs. The model predicts $\Delta V/V_0$ to be 26% and 15% for 100 and 200 μm respectively. These values disagree with the experimental values by about 15% in both cases.

The discrepancy between the experimental and calculated values of $\Delta V/V_0$ can be attributed to several sources including a variation in the processing parameters across the wafer surface and, in particular, to the deviation of the actual path of current flow in the structure from that assumed in the model. The model assumes that the current flows in a straight line perpendicular to the metal electrodes. For the type 1 structure, for example, the actual path will be diagonal across the wafer if the potential difference for a diagonal path adequately compensates for the increased resistance along that path. The difference in values can be partially attributed to the fact that the metal electrodes have slightly larger resistances than the quoted 27Ω due to an additional 10 to 20 μm of metal added to the electrode for placement of the probes.

The values in table 4.1 can be used to arrive at an approximate doping level for the P^+ material. Given that the doping extends to a depth of $T = 0.7 \mu m$, plots of resistivity versus doping, such as in Sze's book²⁷ yield, a doping level on the order of 10^{19} . This number is consistent with other measurements made in the lab.

F. SUMMARY AND CONCLUSIONS

This technical memorandum has briefly discussed the physics of semiconductor electrical contacts and the importance of low resistance Ohmic contacts for proper device performance. A simple method was presented for deducing the resistance of the electrical contacts and the bulk GaAs semiconductor. The

fabrication of several contact structures was discussed. The structures were tested for the resistance of the metal and P^+ GaAs, the contact resistance and the temperature dependence of the resistance of the metal and P^+ GaAs. The appendix to this technical memorandum discusses the distributed resistance of the GL100 contact structure.

The contact study has important implications for laser-based logic gates, optical amplifiers and electrically pumped optical waveguides which use similar contact structures. For a resistive contact, current injected into one end of the contact will not evenly distribute along the length of these devices and, as a result, the devices will not be uniformly pumped. For the laser-based logic gates, the interaction between adjacent lasers will depend on the relative positions of the two devices in the integrated circuit. The gain of the laser amplifier which employs these contacts will be largest near the end where the current is injected. It is possible for the gain to vary in such a way that the amplifier or laser is both above and below transparency or threshold along the length of the device.

V. APPARATUS FOR THE ANALYSIS OF OPTICAL LOGIC GATES AND COMPONENTS

This chapter is a compilation of selected analysis techniques, developed during the past two years, for characterizing optical logic gates and their component parts. It discusses the testing of these elements from the initial probe station setup to the specific test setups. Coverage includes optical/electrical probing techniques, device preparations, and equipment configurations for current vs. voltage (I-V) characteristics, emitted light vs. injected current (L-I) characteristics, hysteresis, Lissajous effects, and quenching.

A. INTRODUCTION

The primary tasks of the Device Engineering Group at Rome Laboratory's Photonics Center are to design, fabricate and evaluate devices which show promise in future digital optical computing schemes. The optical logic gates, fabricated at Cornell University's National Nanofabrication Facility, are cleaved, mounted, and evaluated at the Photonics Center. The devices under study include lasers, optical amplifiers, optical NOR gates, optical RS flip flops and optical memory elements. Typically, each element emits and/or absorbs light at approximately 850 nm. Characterization of these devices requires a number of different setups easily modifiable to the particular Device Under Test (DUT). First, the DUT must be optically and electrically probed, and then the equipment can be configured to measure basic properties such as current versus voltage (I-V) curves, emitted optical power versus drive current (L-I) curves, hysteresis, and quenching.

This chapter first discusses the probe station and equipment needed to input and extract the pertinent signals. The "Signals: Source and Measurement" section covers the general system setup, specific test configurations, and some of the customized source and measurement aides used with the system. The "Experimental Results" section presents some typical data plots. Finally, some general conclusions about the system as a whole and possible future additions are made.

B. OPTICAL/ELECTRICAL PROBE STATION AND PERIPHERALS

The Electro-Optic Probe Station (Figure 5.1) serves as the signal pickup point in the test system. This unit supplies the device with the required drive currents and/or source signals and probes the device for its

particular optical and electronic properties. The station must also support the DUT and provide it with a stable environment to accurately retrieve the signals of interest.

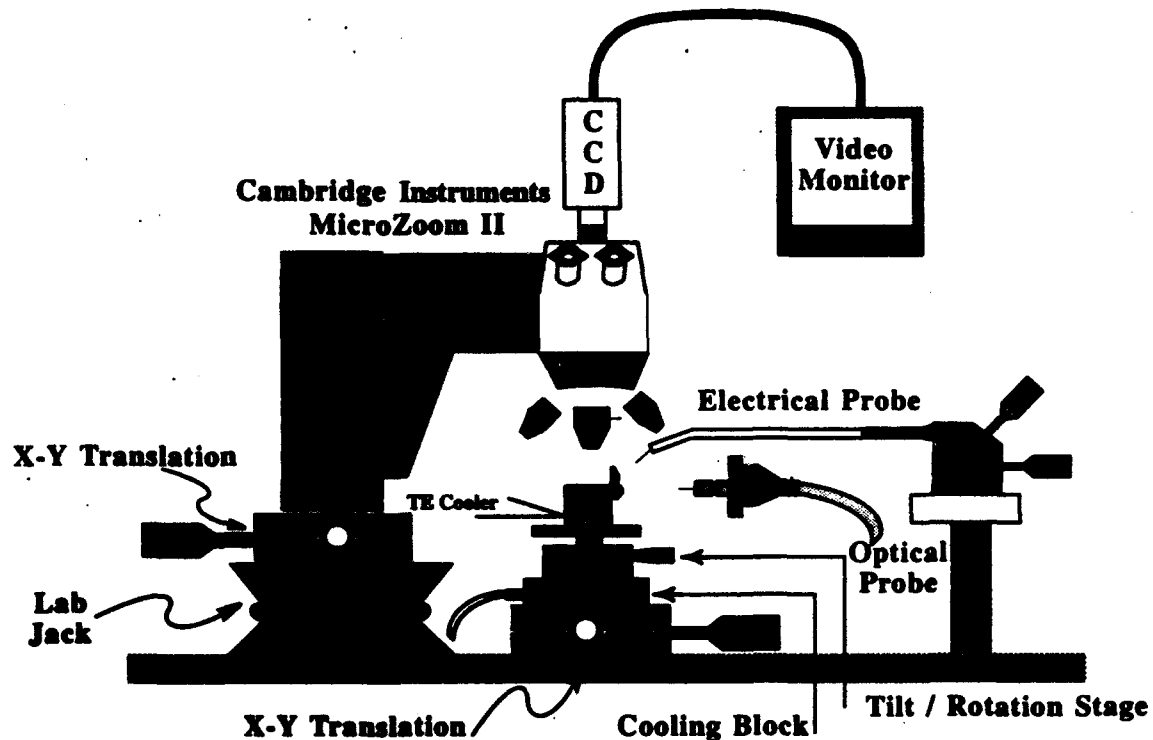


Figure 5.1: Electro-Optic Probe Station

B1. Probe Station Configuration

The heart of this probe station is a Cambridge Instruments MicroZoom II microscope with up to 3000X and 2 cm working distance. Included in the microscope system is a CCD camera and monitor to observe the working area without having to look through the microscope. The microscope is mounted on a large X-Y translation stage and a laboratory jack. This gives the microscope X-Y-Z translation and allows viewing of different parts of the DUT without having to remove the probes once they are placed. The devices are electrically mounted on copper blocks which are screw mounted to a cooling plate and cooled by a NEELAB RTE-110 Proportional Temperature Controller. The devices have X-Y translation, two-axis tilt, and rotation for proper positioning. Electrical probing is accomplished using Alessi high-frequency and DC probes mounted on X-Y-Z translation stages. The input optical probe is a free-space beam from an

Argon Ion/Ti:Sapphire combination (not shown). This beam is focused down to the device input facet after passing through polarization optics.

B2. Mechanical, Electrical, and Thermal Device Stabilization

A series of procedures are used to maintain the device's mechanical, electrical, and thermal stability. The device mount block (figure 5.2) is a thin strip of copper less than 1/4" thick. This strip is filed down at an angle and the tip is polished flat to make a smooth level surface approximately the width of the chip containing the DUTs. This copper strip serves as the common ground and as the heat sink for all the devices. The chip is mounted using Epo-Tek H20E silver epoxy. With the copper mount bolted to a stationary copper block (not shown), a thin layer of the Epoxy mixture is spread on the top ledge and scraped to remove the excess. The chip is then placed on the epoxy and positioned as necessary. After positioning, the mount is placed on the hot plate at 120° C for 15 minutes. This sets the device in place and makes the epoxy electrically conductive (less than 1Ω). The device mount is then bolted to the probe station cooling block for testing. The device mount block provides easier handling, an electrical connection to the ground side of the chip, and thermal heat sinking to draw heat away from the operating devices.

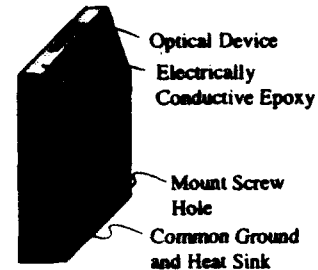


Figure 5.2: Device Mount Block

The device cooling system (Figure 5.3) consists of a cooling plate (cooled by the NESLAB Temperature Controller), a tilt/rotation stage, a thermo-electric (TE) cooler, and the device mount block described above. The cooling block is merely an aluminum block with two 1/4" holes drilled into the sides at 90°. The holes are drilled such

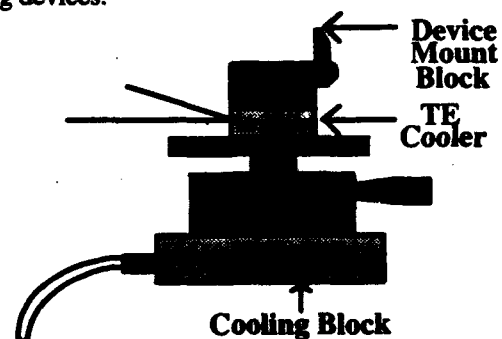


Figure 5.3: Cooling System

that one is slightly above the other where they meet in the center of the block to allow better coolant flow. The coolant, ethylene glycol, is pumped from the chiller, through the block, and back to the chiller. This maintains a cold plate (the tilt/rotation stage) for the (TE) cooler. A Melles-Griot Diode Laser Driver box used in conjunction with their General-Purpose Thermoelectric Cooler Head maintains a constant

temperature on the device. The last part of the cooling system is the device mount block in figure 5.2. In the completed cooling system, the TE cooler draws heat away from the heated device mount, and the cooled rotation stage removes the heat from the hot side of the TE cooler. A further modification will consist of some type of nitrogen flow over the entire cooling system. This will permit device cooling at temperatures below room temperature without the electrical problems associated with condensation.

B3. Optical and Electrical Probing

Optical output probing is accomplished using the fiber probe shown in figure 5.4. The key to this probe is the syringe needle support which allows the fiber to extend well past the end of the fiber chuck and permits the fiber tip to be placed very

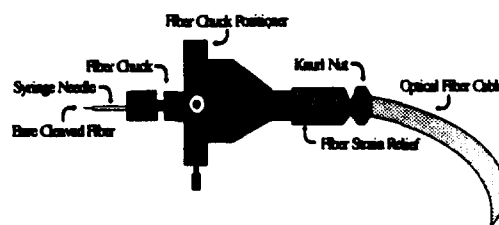


Figure 5.4: Optical Probe

close to the device output. This also eliminates the instability problems associated with having a bare fiber hanging in free space.¹⁰ Probe alignment with the device output consists of visually aligning the probe, then driving the device with a pulse and using a photodetector to measure the strength of the optical signal at the other end of the fiber. When the signal from the photodetector reaches a peak, the optical probe is aligned with the device output.

The purpose of electrical probing is to supply the necessary bias and drive signals to the device and to pick off the electrical signals at the desired points. The Alessi high-frequency probes provide a 50Ω load to high frequency signals; whereas, the DC probes provide a direct connection to the probe tip. Probe alignment is managed through microscopic observation of the probe tip and the contact pad, while the magnetic-base micropositioners move the probe until contact is achieved. The signal return path is provided through the device mount as a common ground connection.

The tip of the probe is of great concern when contacting these devices. The Alessi tungsten probe tips typically make better electrical contact with the device, provide a more stable electrical connection, and have a lower contact resistance (0.2Ω per contact). The main problem with the tungsten probes is they can destroy the device contact pads. An alternate probing method employs gold-wire tipped probes. A 25μm

gold wire is soldered onto the tungsten probe tip. This wire is then used to contact the device. First, the wire tip is positioned over the contact pad using the microscope for viewing. The probe is lowered until the tip makes contact with the pad. Next, a current is passed through the line to the device while viewing the curve tracer display. The current causes Joule heating, and the tip of the gold wire is melted onto the contact pad. Thus, the electrical connection is made. This connection can be removed from the contact pad easily, and no contact pad damage occurs. However, the connection is unstable. Table movement or even air currents in the room can remove the contact. Also, the probe resistance is greatly increased from that of the tungsten probe, typically 10Ω per contact. This means that Joule heating may vaporize the contact during testing. So, to maintain a good, stable, low-resistance, electrical contact, the tungsten probes are used. But when concerned with contacting a device several times, contact resistance and stability are sacrificed for the reusability of the gold-wire probe.

Once the probe tip physically contacts the pad, the integrity of that contact must be determined. This is achieved by using a Tektronix type 576 commercial curve tracer.

Figure 5.5 shows the setup used to test the integrity of the electrical connection. The

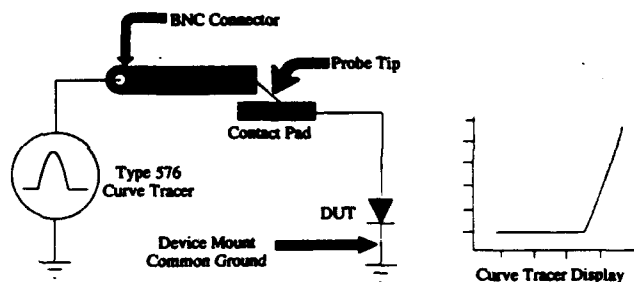


Figure 5.5: Probe Contact Integrity Test

curve tracer supplies a stepped, half sine wave to the DUT and displays the typical I-V curve for a diode. Once the device current can be raised and lowered while maintaining a steady trace, the connection is stable with good contact integrity.

C. Optical/Electrical Signals: Source and Measurement

The probe station supplies and retrieves the necessary signals to the DUT. Figure 5.6 shows the general test system to supply and analyze the appropriate signals. In this picture, the probe station is represented by the DUT shown in the center. The Argon Ion/Ti:Sapphire laser system combination provides a wavelength range from 760 nm to 910 nm. This wavelength is fully programmable over the GPIB bus. The polarization optics allow the device to receive either TM or TE polarized light, or both.

The neutral density filters are actually polarization filters attached to GPIB controlled rotation stages; this is connected through GPIB to the computer and is programmable. This part of the system allows the user to control the input wavelength, polarization, and power to the DUT. The lens focuses the input beam down onto the DUT's input facet.

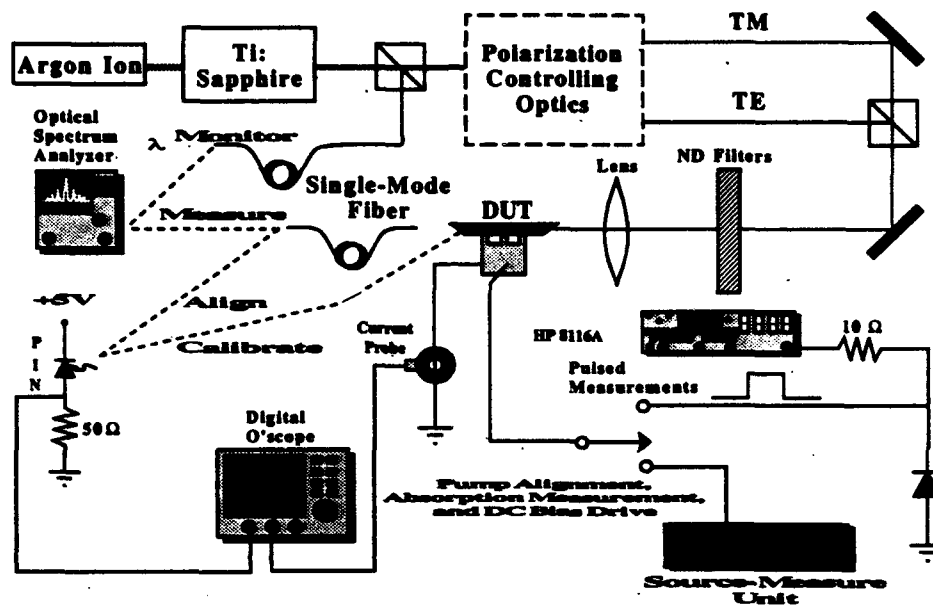


Figure 5.6: Test Setup for Basic Device Optical and Electrical Characterization

Electronically, the device is driven either by the HP 8116A Pulse/Function Generator (PFG) or the Keithley 238 High-Current Source-Measure Unit (SMU), depending on the test being performed. The HP 8116A can supply sine waves, triangular waves, pulses, and single cycles of the sine wave and triangular wave signals. The Keithley SMU can source and measure currents and voltages with current source/measurement ranges of ± 1.0000 nA (with 100 fA step size) to ± 1.0000 A (with 100 μ A step size) / 10 fA to 10 μ A resolution and voltage source/measurement ranges of ± 1.5 V (with 100 μ V step size) to ± 110 V (with 10 mV step size) / 10 μ V to 1 mV resolution.

The components on the left side of figure 5.6 are devoted mainly to the measurement of the retrieved signals. Optical measurements occur in different forms. The coherent wavelength from the Ti:Sapphire is measured from a beam split off from a beam splitter cube through a single-mode fiber to the Anritsu MS9701B Optical Spectrum Analyzer (OSA). The light from the device can be measured solely as a

power using the PIN detector with or without the fiber coupling, or the fiber probe can be connected to the spectrum analyzer to make a more extensive analysis of the emitted light. The HP 54111D Digital Storage Oscilloscope (DSO) measures the electrical properties of the DUT. A Pearson Electronics, Inc. model 2877 inductive current monitor detects the current through the ground lead of the DUT; the signal is displayed on the DSO. The DSO is also used to measure the voltage generated across the dropping resistor connected to the PIN photodiode, which is a representation of the amount of light applied to the PIN. All of the data retrieved with the DSO and the OSA can be down loaded to a computer over the GPIB bus (not shown). The ways in which these pieces of equipment (and others not shown) are connected determine the characteristics that can be extracted from the device under test.

C1. Specific Test Configurations

To perform the current versus voltage (I-V) test, the DSO is the only measurement equipment required. The PFG supplies a triangular pulse of the desired frequency and amplitude. Channel 1 on the DSO is connected to the current monitor, and channel 2 is connected across the device. The I-V characteristics for the device are displayed on the oscilloscope by plotting channel 1 versus channel 2. Once down loaded to the computer, the data can be saved, and analyzed, or used to produce hard copies.

The emitted power versus current (L-I) test is performed much like the I-V test described above. The device drive signal is supplied by the PFG again, and the current monitor/DSO combination measures the drive current. To measure the emitted power, the PIN detector is aligned with the output beam for the DUT. This is accomplished by pulsing the current to the device and moving the photodetector around until the maximum signal is observed on the DSO. With the current applied to channel 2 and the signal from the PIN photodiode output applied to channel 1, channel 1 versus channel 2 gives a representation of the L-I curve. To get an accurate L-I characteristic, the data must be down loaded to the computer; where the voltage from the PIN is converted to an optical power by using a scaling factor.

The hysteresis test is simply another form of the L-I test. Certain devices such as the optical RS flip-flop¹¹ display bistability in their L-I curves. Hysteresis is the result of the device having two possible output states or optical intensities for a single given drive current. This would be displayed as a loop on

the characteristic L-I curve. With this test, it is important that the triangular pulse driving the device is completely displayed on the DSO screen. In order to observe hysteresis, the drive current must be ramped up and then back down again. In general, the observed loop consists of a component due to resistive/capacitive (RC) time delays and the other is the hysteresis effect. The width of the Lissajous figures due to these time delays are greatly affected by the length of the electrical leads, the method of electronic coupling and the different circuit capacitances and resistances. The effect of the test setup and parameters on the width of the loop is discussed in the hysteresis and Lissajous analysis section.

Quenching is a characteristic which is extremely important for, but not limited to, the optical NOR gates.^{2,28} These devices are composed of two main components, a main laser and a side laser with overlapping cavities. In operation, the main laser is biased in the ON condition emitting coherent light. When the side laser is biased ON, it competes with the main laser in the common cavity area and turns the main laser OFF. Characterization of such devices requires measurements of the main laser emission and drive current, and the side laser drive current. The main laser is driven with a square pulse from an HP 8131A pulse generator (not shown in figure 5.6), the side laser is driven with a triangular pulse from the PFG, and both currents are monitored using the Pearson Electronics, Inc. current probes. The light emitted from the main laser is measured using the PIN detector and DSO. To perform this test, the pulse generator and the PFG are synchronized together so that the side laser triangular peak occurs exactly at the center of the main laser square pulse. Looking at the emitted light from the main laser will show the reduction in its output while the side laser is ON.

C2. Low-Speed I-V / L-I System

All of the tests described above are high-speed tests in that the source signals for the devices come from the PFG and the pulse generator which are high-speed instruments. In essence, all of the data for a single I-V, L-I, hysteresis, and quenching characteristic are obtained with one pulse from the drive signal. However, the DSO is limited to 1 mV/div, which limits the resolution of the current and power measurements. Through the use of optical power meters and the Keithley SMU, more accurate data can be taken. This method is slow as it requires GPIB programming to apply a bias with the SMU, measure the

power, remove the bias for the device to cool down, then step the bias to the next level and repeat. Essentially, the L-I or I-V data is taken one point at a time. The source-measure unit measures currents in the range of nanoamps, and the power meter measures optical powers down to picowatts. So, more accurate data is obtained at the cost of speed.

C3. Optical/Electrical Source and Measurement Aides

In the process of testing, several circuits were constructed to aid in the measurement and source of the pertinent signals. Sometimes the test equipment was unable to provide the necessary current to drive the DUT. Therefore, two types of current amplifiers were constructed to overcome this problem. Also, a wide-area photodetector circuit (the PIN detector shown in figure 5.6) was needed to collect all of the emitted light.

The first current amplifier circuit was built to amplify the signal produced by a digital-to-analog (D-A) board in the computer.²⁹ The Data Translations DT2823 data acquisition board can only supply up to ± 5 mA. The circuit in figure 5.7 amplifies this signal to a

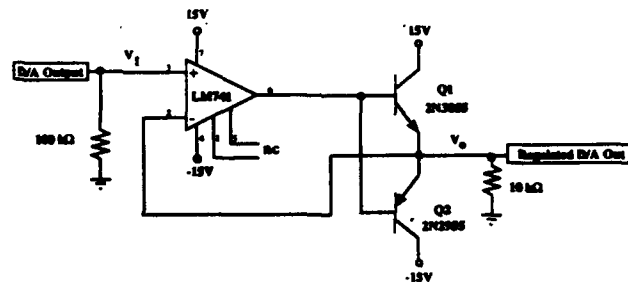


Figure 5.7: Low-Speed Current Amplifier

maximum of ± 1 A. The basic consideration for this design was to get an output signal that exactly duplicated the D-A signal but with a much higher current. The two main parts of the circuit are the LM741 operational amplifier (Op Amp) and the class B amplifier formed by the two power transistors (Q_1 and Q_2). The power transistor pair boosts the output current up to 1 A. The op amp is wired in a negative feedback configuration to regulate the output voltage (V_O) to the input value (V_I).

Because of heating problems, some tests must be run on the microsecond level. This requires a faster current amplifier for the 8116A and 8131A signal and pulse generators. In general, this amplifier is on the order of 1000 times faster than the previous system. Figure 5.8 shows the schematic diagram for this fast current amplifier. Q_1 is a

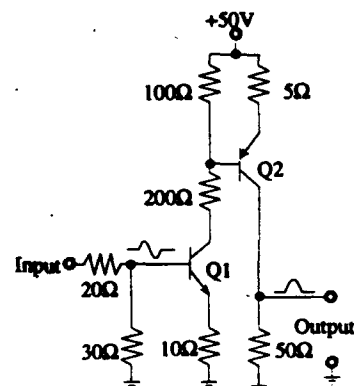


Figure 5.8: Fast Current Amplifier

2N3055 NPN transistor, while Q2 is a MJE2955 transistor. These power transistors are capable of delivering 10A to the load. At 500kHz, they are capable of maintaining 500mA. This circuit serves as a half-wave rectifier, passing only the positive half of the input waveform. At this point, only positive biases are needed on the particular elements under test. The +50V supply is decoupled to ground with a 0.1 μ F capacitor. This prevents the pulse signals from passing to the power supply via the ground plane. The circuit, as shown, amplifies up to 1 μ s triangular pulse widths with an amplitude of better than 20 volts into a 10 Ω load. This allows a triangular 1 μ s pulse, maintained at a current level of 2 amps or better, for the device drive signal. Two identical circuits were constructed to amplify both the 8116A function generator and the 8121A pulse generator signals at the same time during testing. The two copies of the circuit are housed in a standard aluminum box with 4 BNC connectors for the two input and output signals; there is one BNC connector for the 50V power supply.

Another circuit aids in the measurement of the light emitted by the devices. This is the wide-area (PIN) photodetector shown in figure 5.6. This permits signal viewing directly on the oscilloscope. Figure 5.9 shows the designed photodetector circuit. The switches in the circuit permit quick tailoring of the detector circuit to the type of measurements and coupling schemes needed. Photodiode #1, a germanium device, has a slow rise and fall time, therefore the silicon photodiode, which

has rise and fall times in the range of hundreds of picoseconds, was added. The 50 Ω and 5.1k Ω resistors develop the output signal from the photocurrent supplied by the selected photodiode. The 5.1k Ω resistor delivers a higher output signal for a given input optical signal. This resistor also more appropriately matches the impedance of the oscilloscope when using high-impedance coupling. Coupling to the scope on the 1M Ω scale can cause ringing and drastically reduces the displayed signal rise and fall times of the signal. Therefore, the 50 Ω resistor is included to see more accurate rise and fall times. To further reduce

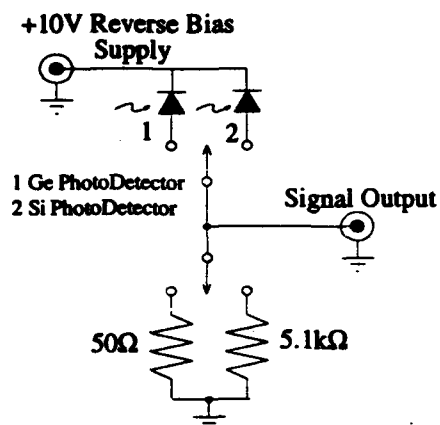


Figure 5.9: Photodetector Circuit

any delays in the system, the signal output connector is a female BNC that connects directly to the scope. This reduces the delays caused by long cables.

D. EXPERIMENTAL RESULTS

This section presents some typical data acquired from different optical logic devices using the test systems described above. The high-speed I-V, L-I, hysteresis, and quenching data includes an analysis of the Lissajous effects associated with electronic RC time delays. The low-speed I-V and L-I data shows the ability to measure very small current and small power signals.

D1. High and Low-Speed I-V/L-I Data

Figure 5.10 shows typical I-V and L-I curves acquired from a semiconductor laser amplifier.³⁰ This amplifier is exactly like the etched facet lasers described in earlier chapters except the facets are etched at angles other than 90° . This angled facet inhibits the Fabry-Perot resonance associated with normal etched facet lasers. The turn-on voltage and device on resistance can be extracted from the I-V curve (left). This graph shows a turn-on voltage of approximately 1.55 V, and by calculating the slope of the curves linear portion, the device has an on resistance of 19.7Ω . The lasing threshold current and differential efficiency for the amplifier are exhibited by the L-I curve (right). The linear portion of the line is extrapolated back to determine the threshold current which is 26.7 mA in this case. The slope of the linear section determines the differential efficiency, 0.16 mW/mA.

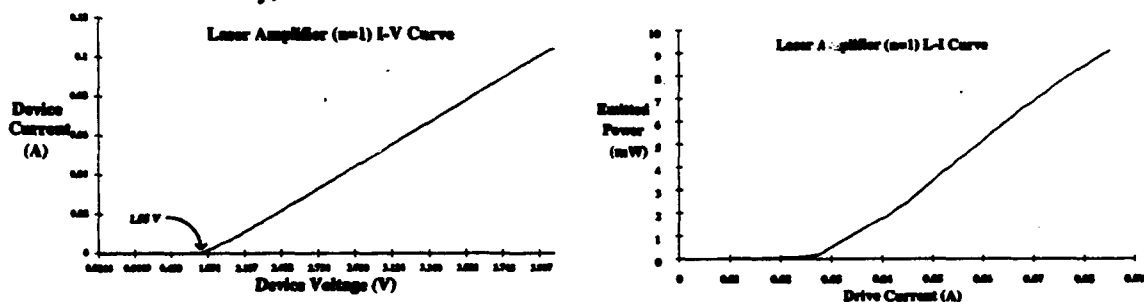


Figure 5.10: Characteristic Curves for a Laser Amplifier with 0.57° facets

The results shown in figure 5.10 can be compared to those in figure 5.11. The data for figure 5.11 was obtained using the low-speed test system. The DUT in this case was a surface-Emitting Laser Logic (CELL) device.³¹ This device consists of a monolithically integrated heterojunction phototransistor (HPT) and a vertical cavity surface-emitting laser (VCSEL). The reason for using the low-speed setup for this

device is the high resolution which the SMU and power meter can attain. These curves show the CELL operating under dark conditions; i.e., there is no light applied to the HPT and therefore, the device is off. Because the CELL is off, an accurate turn-on voltage and threshold current are not displayed here. However, the I-V curve does give a feeling for the degree of device resistance when the CELL is off. The slope of the I-V curve from 5 to 7 volts indicates that the CELL device OFF resistance is on the order of 66.4 k Ω . The main purpose of this demonstration is to show the accuracy with which data is acquired using the low-speed test system. In this case, the system measures currents well below the 20 μ A level and powers below the nW range.

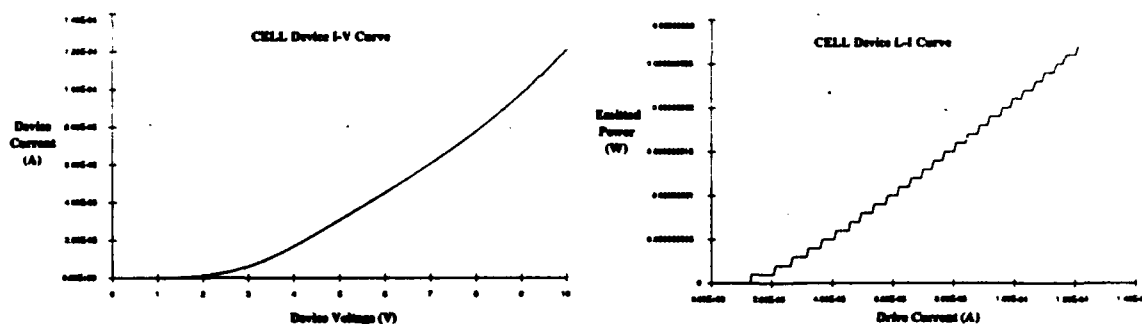


Figure 5.11: Characteristic I-V and L-I Curves for CELL Devices in the OFF State

D2. Hysteresis and Lissajous Analysis

Hysteresis is a very important aspect of logic gates and memory elements; it is a measure of the ability of the memory element to maintain two different optical power levels at a single drive current. Figure 5.12 shows the L-I hysteresis data obtained from the main laser of the RS flip-flop discussed in Chapter 10. The three curves displayed on this graph represent the main laser drive signal (V_g), the main laser output intensity (L_g), and the main laser intensity versus the main laser drive (L_g vs. V_g). The important feature to notice here is the protrusion on the L_g curve. This is an indication of higher optical power emitted by the laser for the same applied current. This is the feature that results in the open loop on the L_g vs. V_g curve.

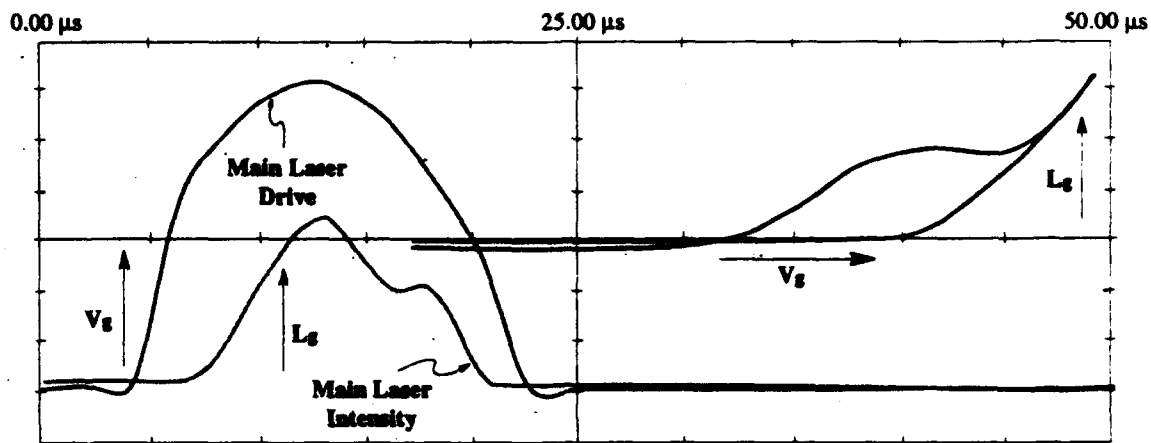


Figure 5.12: Hysteresis Displayed on the DSO

The desired feature in figure 5.12 is the wide opening in the hysteresis loop on the right hand side. However, a laser without a saturable absorber will produce an open loop -- the Lissajous figure -- due to the various delays in the test system. For example, if the light detection system has electronic delays due to long lead lengths or improper signal coupling, the L_g curve is shifted to the right. This would result in a loop displayed in the L_g vs. V_g curve.

Figure 5.13 can be used to determine the expected loop width due to system delays. This plot shows that the width of the Lissajous figure increases with decreasing pulse width and increasing drive current. To determine the expected loop width, first determine the drive current and the drive pulse width. From these values, the expected loop width with no hysteresis present can be extrapolated. Example: With a 3 μ s pulse width and a drive current of 80mA, the expected loop should be 0.32V wide. Any loop which is substantially greater than this 0.32V under these conditions can not be attributed to RC effects.

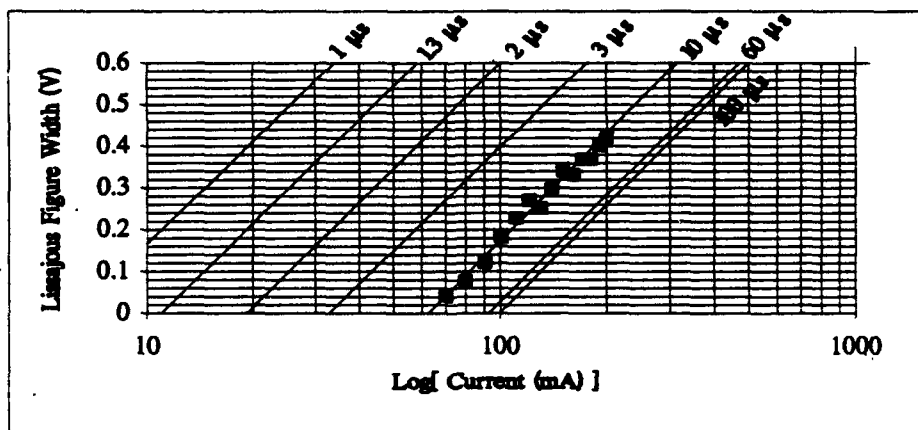
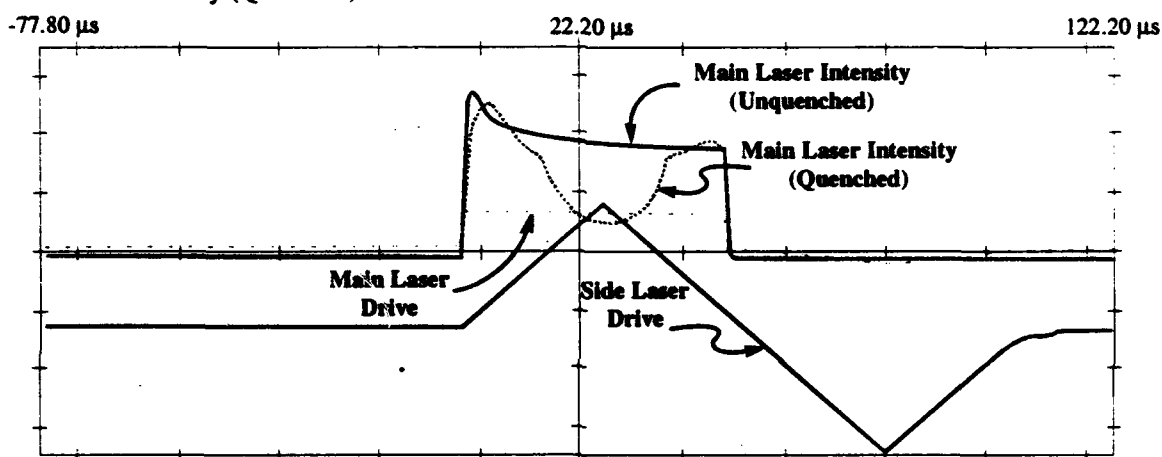


Figure 5.13: Lissajous Figure Width versus Drive Current and Pulse Width

D3. Quenching Analysis

Both the optical NOR gates and the optical flip-flops make use of intersecting laser cavities to quench the output of a main laser. The configuration described in section C1 is used to measure this characteristic. Figure 5.14 shows an example of quenching as measured on the DSO. The main laser drive is a square pulse. The light out of the main laser is also comparable to a square pulse. The side or quench laser drive is the triangular pulse. When the triangular pulse is applied to the side laser, the main laser is quenched, and the emitted power drops dramatically at the peak of the quench pulse. This is easily observed in the Main Laser Intensity (Quenched) curve.



Plot 5.14: Quenching Example

E. Conclusions

The setups described herein can be used to examine a variety of optical logic gates and their component parts. The devices can easily be mounted, cooled, and probed optically and electrically, to ascertain their specific characteristics. Using commercial test equipment and specially designed circuits, accurate data is collected and saved quickly. A high-speed system has been constructed to acquire I-V curves, L-I curves, quenching data, and hysteresis data for specific optical logic gates and their components. A low-speed I-V and L-I system permits much better current, voltage, and optical power resolution at a much slower data acquisition rate. A chart has been developed to easily verify how much of an L-V loop is due to hysteresis and how much is due to RC effects in the system. Also, computer code has been developed to control the tests and manipulate the retrieved data.

VI. CHARACTERIZATION OF A SEMICONDUCTOR OPTICAL AMPLIFIER FOR USE IN OPTICAL COMPUTING SYSTEMS

A semiconductor optical amplifier was characterized for use in optical computing systems. The functional dependence of gain on bias current, input optical power, polarization and wavelength was determined. The total power, the full-width at half-max. (FWHM) and the peak wavelength of the spontaneous emission was measured. Most experimental results were found to be in agreement with the specifications supplied by the manufacturer. The theory of semiconductor optical amplifiers is also discussed.

A. INTRODUCTION

Optical attenuation and losses are serious problems in the fabrication of optical communications, switching and computing systems. Long distance fiber communications, for example, require the use of electronic repeater stations to compensate for signal degradation caused by fiber losses. Severe fan-in / fan-out losses occur in optical crossbar switching networks where several input channels carrying signals must be switched or interconnected between a selection of output channels. Overcoming optical attenuation is also a major hurdle in optical computing. Optical computing elements such as optical logic gates and spatial light modulators exhibit large optical losses which limit the degree to which they may be cascaded.

Optical amplifiers are a potential solution to these problems. These relatively new devices can provide gain for optical signals without the aid of electronic subsystems. This chapter briefly describes the characterization of a BT&D semiconductor optical amplifier (SOA), the only commercially available SOA at the time of this experiment, for use in optical computing systems. The theory of operation of the SOA and the apparatus used to measure the operating parameters of the SOA are presented first. Experimental results on the polarization sensitivity, spontaneous emission and gain of the amplifier are then discussed.

B. THEORY

A semiconductor laser amplifier is similar in structure to a laser diode; figure 6.1 is a schematic of

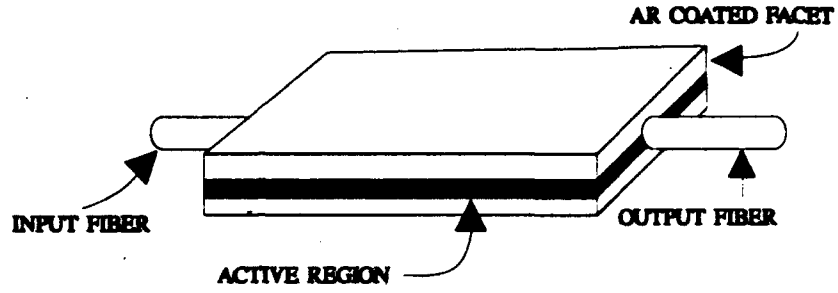


Figure 6.1: Schematic of SOA Amplifier.

an optical amplifier. An external current source is

connected to the device and injects carriers into the active region. The number of carriers injected is proportional to the bias current i_b and provides for a population inversion. Light signals enter the active region of the SOA via a single mode input fiber and interact with the excited carriers in the SOA cavity causing stimulated emission and hence gain. In addition to stimulated emission, there is also spontaneous emission due to the random recombination of carriers. Thus, the total optical signal exiting the amplifier via a single mode fiber is composed of both stimulated and spontaneous emission components. The total optical output power P_O emitted by the device for an optical input power P_i is

$$P_O = P_i G(\omega) + P_{sp} \quad (6.1)$$

where the first term represents the stimulated component of the output and the second term represents the spontaneous component. The net gain of the amplifier $G(\omega)$ is a function of optical frequency and is equivalent to the transmission of a Fabry-Perot cavity with single pass gain given by³²

$$G(\omega) = \frac{G_s(1-R_1)(1-R_2)}{(1-G_s\sqrt{R_1R_2})^2 + 4G_s\sqrt{R_1R_2} \sin^2(\frac{\omega nd}{c})} \quad (6.2)$$

where R_1 and R_2 are the facet reflectivities, d the cavity length, G_s the single pass gain of the device, n is the index of refraction and $\omega = 2\pi f$. G_s is dependent on the degree of confinement of the TE and TM modes in the wave guide and the average intensity of light in the cavity. It is given by:

$$G_s = \exp \frac{(\Gamma g_0 - \alpha)L}{1 + I/I_s} \quad (6.3)$$

where Γ is the mode confinement factor, g_0 is the unsaturated gain coefficient (per unit length), α is loss in the cavity (per unit length), L is the length of the cavity, and I and I_s are the light intensity and saturation light intensity in the cavity, respectively.³³

Gain in the SOA monotonically increases with the population inversion created by the bias current i_b . As the intensity of the light I in the cavity increases, the population inversion in the cavity becomes depleted. As seen from equation 6.3, the single pass gain of the SOA will decrease as I approaches I_s causing the net gain of the amplifier to decrease. I_s is defined to be the intensity at which the SOA gain is reduced by 3 db and it is the point where gain saturation occurs. Hence gain saturation is a function of input optical intensity.

The mode confinement factor, Γ , also effects the gain of the SOA. The mode confinement is dependent on the polarization of the signal input to the SOA and will have different values for TE and TM input modes. Since the gain of the SOA is dependent on the mode confinement factor as seen from 6.3, and the mode confinement factor, in turn, is dependent on polarization, the SOA has polarization dependent gain. The mode confinement factor is typically larger for the TE mode than the TM and hence an input signal with TE polarization experiences a higher gain than one with TM polarization. Another source of gain dependence on polarization stems from a difference in facet reflectivity for the TE and TM modes that is due to Fresnel reflection.³⁴

Despite its many dependencies, the gain of the SOA is ultimately limited by losses due to coupling fiber with the SOA. These losses arise from the fact that light is being coupled from a circular fiber into a rectangular waveguide causing mode mismatching to occur. Coupling losses on the order of 5 db are typical at each fiber interface.³⁵

Semiconductor optical amplifiers generally fall into two main categories depending on the values of their facet reflectivities: Fabry-Perot and traveling wave. An ideal traveling wave amplifier has end facets with zero reflectivities to suppress oscillations in the cavity. Setting $R_1 = R_2 = 0$ in equation 6.2 gives

$$G(\omega) = G_s \quad (6.4)$$

Hence, the net gain of the device is just the single pass gain of the cavity. This is the ideal configuration for an SOA because the amplification is caused only by single pass gain, differentiating the operation of the amplifier from that of an oscillator such as a laser diode. In reality, however, there is residual facet reflectivity on the order of $R = 1 \times 10^{-4}$ and the actual device is termed a near traveling wave amplifier. An SOA must have a gain modulation (peak to peak passband ripple) of less than 3 db to be categorized as a near traveling wave amplifier. This corresponds to having reflectivities which satisfy the condition³⁶

$$G_s \sqrt{R_1 R_2} < 0.17 \quad (6.5)$$

The near traveling wave amplifier has a wide bandwidth, less temperature and polarization sensitivity, and higher saturation output powers than the Fabry-Perot amplifier. It does, however, have an increased sensitivity to reflections from fiber coupling and requires a larger bias current for operation. The larger bias current will, in turn, mean a larger spontaneous noise component.³⁷

A Fabry-Perot SOA, on the other hand, will have a gain modulation greater than 3 db with facet reflectivities typically on the order³⁷ of 0.01 - 0.3. The device is operated near laser threshold and resonance for maximum gain. Near the resonance of a Fabry-Perot, integral numbers of wavelengths occupy the cavity. Thus, the gain of the SOA near resonance can be approximated from (2) by,

$$G(\omega) = \frac{G_s(1-R_1)(1-R_2)}{(1-G_s\sqrt{R_1 R_2})^2} \quad (6.6)$$

Operating near resonance causes the Fabry-Perot SOA to be extremely sensitive to bias current and narrow in bandwidth. The gain of the Fabry-Perot amplifier is also more sensitive to polarization effects due to larger values of facet reflectivities.

C. APPARATUS

The semiconductor optical amplifier used in this evaluation is the BT&D model SOA3100, which was the only commercially available SOA at the time of this experiment. The device comes mounted in a module containing a thermoelectric cooler and two single mode fiber pigtails. Table 6.1 lists some important manufacturer's specifications for the device. The SOA was driven by an ILX model LDX-3670

Ultra Low Noise current source. Temperature stability was maintained via an ILX model LDT-5910 temperature controller set at 20 °C.

Data was taken with an Anritsu optical spectrum analyzer model MS9001B1. A Hewlett Packard optical average power meter model 8152A and optical attenuator model 8158b were also used. The laser source for the experiment was a Laser Diode Corporation model LANA-2013 thermoelectrically cooled laser diode with a center wavelength of 1316.7 nm.

Input polarization into the SOA was controlled using a fiber polarization controller consisting of three paddles. Each paddle can be made to represent a quarter wave plate by looping single mode fiber in it and using stress on the fiber to induce birefringence. The stress induces two orthogonal axes in the fiber, each with a different index of refraction. Laser light input into the controller can be decomposed into two orthogonally polarized states with each parallel to one of the two orthogonal axes. Since these axes correspond to different indices of refraction, the input components travel at different speeds through the fiber creating a net phase delay between them. This phase delay results in a change in polarization of the input light. By moving the paddles and changing the stress on the fiber, any desired output polarization state can be achieved.

<u>PARAMETER</u>	<u>TYPICAL VALUE</u>
Center wavelength	1300 nm
Peak gain	12 db
Ratio of peak of TM gain envelope to TE envelope	5db
Peak to Peak passband ripple	3 db
Operating current	50 mA
Lasing threshold current, I_{th}	70 mA
Optical power @ I_{th} - 20 mA (no input)	25 μ W

The optical amplifier and polarization controller were functionally placed in line between two optical isolators. These isolators prevented back reflections into the amplifier that would cause the SOA to have a lower threshold current. Figure 6.2 is an illustration of the setup. All fiber connections between the

optical isolators were fusion spliced to avoid reflections from fiber connectors. The isolators were found to have a total of 2.3 db loss and the data was adjusted to compensate for this loss.

D. EXPERIMENT

This section presents data for the polarization sensitivity, spontaneous emission measurements and gain measurements. The section on spontaneous emission measurements contains data for the spontaneous emission spectra, peak wavelength, power and FWHM all as a function of bias current. The section on the gain measurements contains gains vs. bias current and gain vs. input power. A typical L-I curve is presented for the SOA tested.

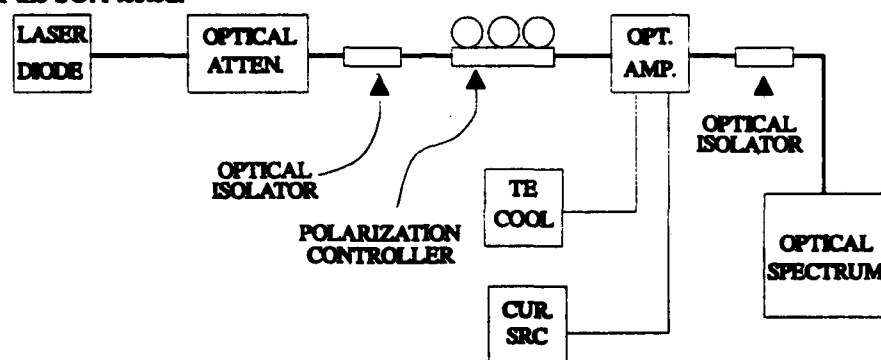


Figure 6.2: Experimental setup.

D.1 Polarization Sensitivity

As discussed previously, semiconductor optical amplifiers exhibit polarization dependent gain. Using the fiber polarization controller, this polarization dependence was examined so the experimental set-up could be optimized for maximum amplifier gain. All fiber interconnects shown in figure 6.2 were secured to prevent movement and thereby preclude a stress induced change of polarization in the fiber. The positions of the paddles on the polarization controller were moved until a minimum in amplifier gain was achieved. The polarization controller was then adjusted to find the position of maximum amplifier gain. A 6 db change in gain with polarization was observed.

D.2 Spontaneous Emission Measurements

The effect of the drive current on the spontaneous emission profile was examined using the same setup in figure 6.2. The laser diode module was turned off for this experiment and figure 6.3 shows the results. As can be seen from the figure, the spectral peak of the spontaneous

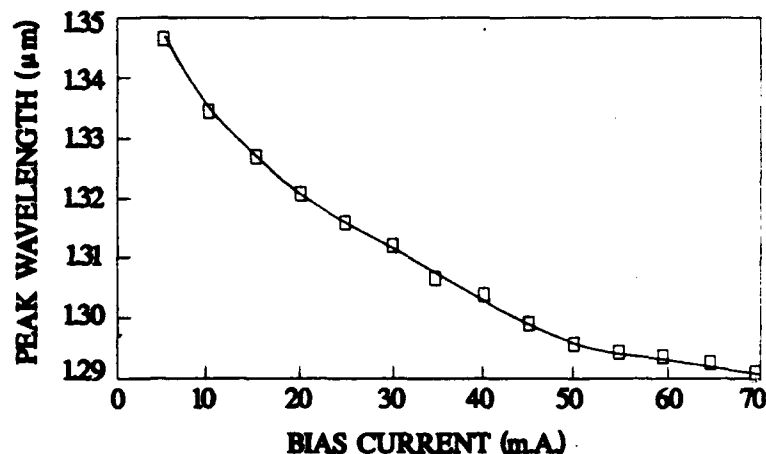


Figure 6.3: Peak wavelength of Spontaneous Emission Vs. Bias Current

emission shifts towards shorter wavelengths as the bias current is increased. This shift is due to band filling. As the drive current increases, the number of injected carriers increases, and higher states in the conduction band, as well as lower states in the valence band, become filled. Since these carriers are further from the maximum of the valence band and the minimum of the conduction band, they "see" a larger effective band gap, and radiation of a shorter wavelength is emitted.

Figure 6.4 shows the actual spontaneous noise spectra for several bias currents. Not only does the spectral peak shift, but the actual size of the noise spectrum increases with drive current. The power of this noise spectra was computed via two methods and then compared. In the first method, data was read from the spectrum analyzer into a computer. Using Simpson's rule, the data was integrated to find the power

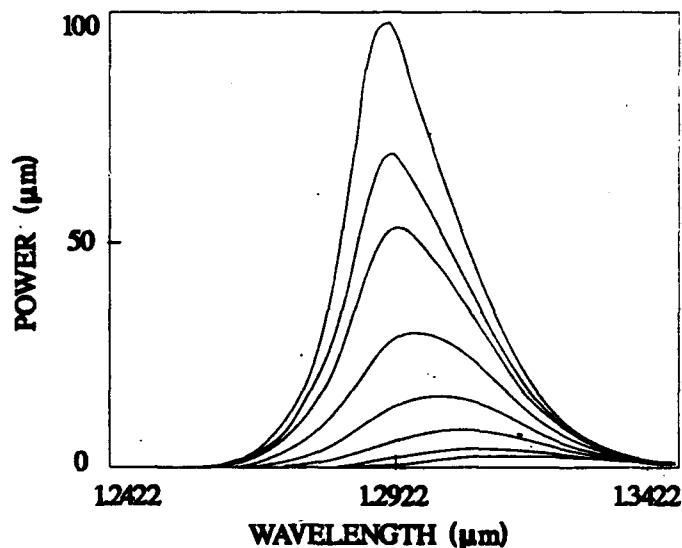


Figure 6.4: Spontaneous emission spectra for various bias currents. The bias current is incremented in 10 mA steps up to 70 mA. The spectra increase with increasing values of bias current.

under the spontaneous emission curve. The second method was to simply use an optical average power meter. Results obtained by both methods were found to be in agreement. The result is given in figure 6.5. It should be noted that the manufacturer specifies an output of 25 μW at 50 mA. We measured 310 μW for the same value of bias current. We confirm this value with both measurement techniques and cannot provide an explanation for this large difference.

The FWHM of the spontaneous profile was observed as a function of bias current. As the SOA is driven closer to resonance, the Q of the device increases and hence the FWHM should decrease. The measurements shown in figure

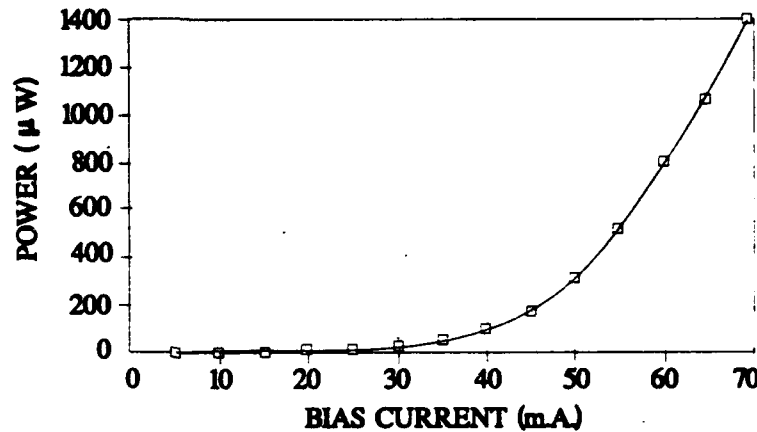


Figure 6.5: Power of spontaneous emission vs. bias current.

6.6 agree with this prediction. Of particular interest is the knee of the curve at 55 mA. This change in behavior marks the start of lasing in the amplifier and is I_{th} .

D.3. Gain Measurements

To measure the gain of the SOA, the laser diode module shown in figure 6.2 was turned on and used to provide an optical signal into the SOA. The amplifier gain was measured as a function of both drive current and optical input power. The optical attenuator, which was functionally placed between

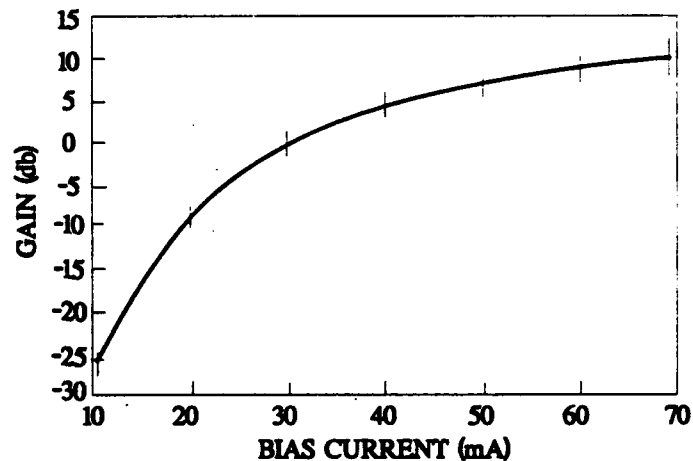


Figure 6.8: SOA Gain vs. Bias Current.

the laser source and the SOA, was used to vary the optical power incident on the SOA. Figure 6.7 is an example of the output of the SOA when an input signal is present for several different bias currents.

The relationship between gain and bias current was first determined. The input optical power was fixed and the injection current was varied. As seen from figure 6.8, transparency for the device occurs at approximately 30 mA.

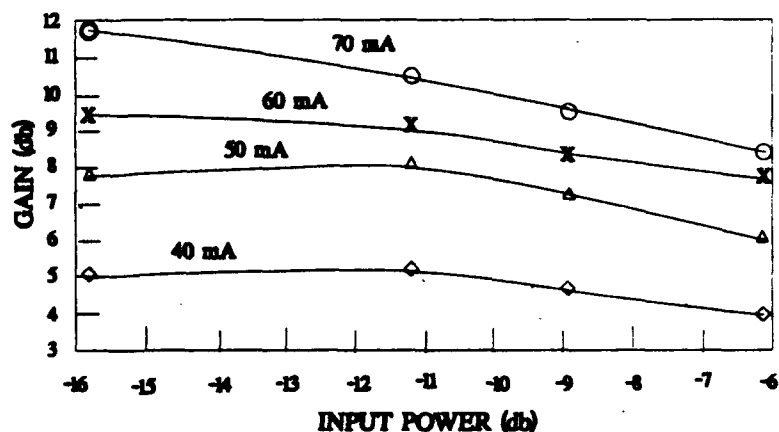


Figure 6.9: Gain vs. Input Power curves as a function of bias current.

This is the point where the absorption and emission rates balance and the gain is therefore unity. The saturation drive current, i_{bsat} , is the value of drive current where the gain begins to level off because stimulated emission has reached a maximum. From figure 5.8, the saturation drive current occurs at approximately 50 mA. Gain saturation effects were determined by varying the optical power incident on the amplifier while holding the bias current fixed. As discussed previously and shown from equation 6.3, gain in the SOA increases with the degree of population inversion in the SOA cavity. As the intensity of the light in the cavity increases, the population inversion in the cavity becomes depleted, causing the gain to saturate.

Gain saturation can be found from figure 6.9, which is the gain versus input power characteristic of the SOA as a function of bias current. As expected, the gain decreases with input power once saturation is reached. The emitted light versus drive current for the device appears as the L-I curve in figure 6.10. The output

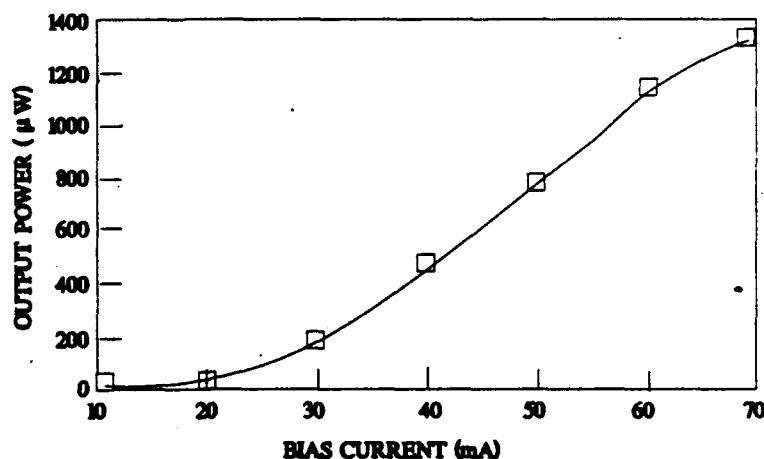


Figure 6.10: L-I curve for the SOA.

power increases with bias current as expected. The growth of the output power is due to both the amplification of the input signal and the increase of the spontaneous output with increased bias current.

E. CONCLUSIONS

In summary, the theory of operation of semiconductor optical amplifiers have been discussed. The gain was shown to depend theoretically on the reflectivity of the facets, the mode confinement factor and the saturation current. Measurements were made of the gain for various values of the bias current, input optical power and polarization. Saturation effects were observed in the gain for sufficiently high levels of bias current and optical power.

The effects of spontaneous emission from the semiconductor amplifier were discussed. The total power, FWHM and the peak wavelength of the optical spectrum of the spontaneous emission were determined. The total power was found to increase exponentially with bias current while the peak wavelength decreased due to band filling effects. The FWHM decreased with bias current since the device was being driven closer to resonance.

The spontaneous emission was seen to be the major source of noise. A normalized signal to noise ration $(S/N)_n$ for the amplifier can be defined as

$$(S/N)_n = \frac{G(\omega)}{P_s} \quad (6.7)$$

The signal to noise ratio at the output of the amplifier is then

$$S/N = \frac{P_i G(\omega)}{P_s} \quad (6.8)$$

where P_s is the power of the spontaneous emission. A plot of the normalized signal to noise ratio of the SOA is given in figure 6.11. As the level of injection increases, the gain saturates while the power in the spontaneous emission curve rapidly increases; these two processes lower the normalized signal to noise ratio. Similarly, the normalized signal to noise ratio decreases at low levels of bias current due to the decreased gain of the optical amplifier. A value of 310 μ W for the spontaneous emission at 50 mA was measured compared with the manufacturer's stated value of 25 μ W.

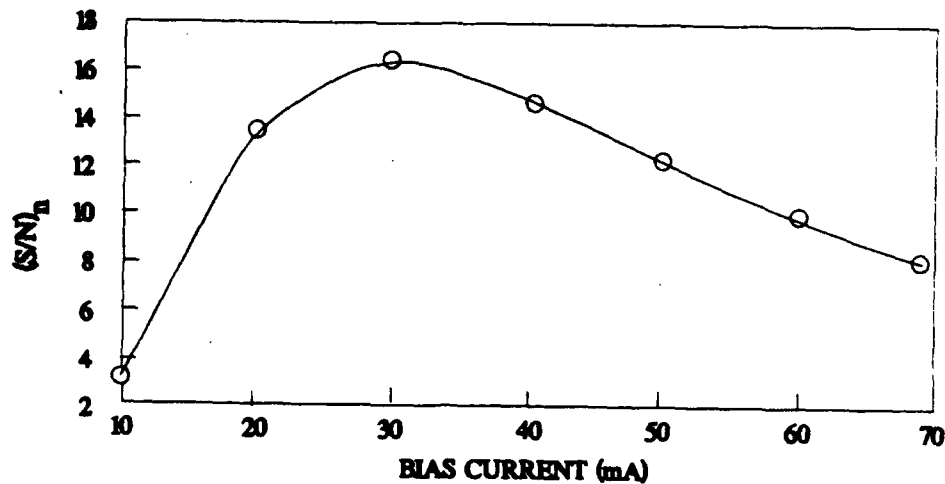


Figure 6.11: $(S/N)_n$ of the SOA.

We found about 11 db of gain for the TE mode. This value exceeds the manufacturer's minimum value of 10 db but the typical value of 12 db was not obtained. This discrepancy might be attributable to differences in bias current, input optical power or wavelength between the manufacturers measurements and those presented here. The wavelength in these experiments was not exactly 1300 nm and hence was not exactly matched to the peak in the gain spectrum. The gain, however, does increase with increasing bias current and decreasing input optical power.

Further work will be done with the semiconductor optical amplifier in the Photonics Center in future. Optical amplifiers might provide a convenient method of amplifying attenuated signals from optical logic elements and these devices could be monolithically integrated with the logic elements. In addition, the SOA could be used to compensate for $1/N^2$ fiber losses in optical crossbar switches. The gain as a function wavelength should be determined in order to deduce the reflectivity of the mirrors and to determine the optical bandwidth. Also, measurements of the temperature dependence of the gain spectrum is important for determining the stability of the amplifier during its operation for long periods of time. This information could lead to improved designs for amplifiers that are monolithically integrated with optical switches.

VII. GaAs - AlGaAs LASER AMPLIFIER WITH ANGLED FACETS

Multimode laser amplifiers were fabricated from GaAs-AlGaAs Graded Index Separate Confinement Heterostructure (GRINSCH) which luminesce near 850 nm. The uncoated facets were angled with respect to the cavity with angles in the range of 0 to about 25° in steps of 0.5° . The amplifiers were tested for (1) lasing threshold current and differential efficiency as a function of facet angle, (2) gain as a function of injected current and facet angle. This chapter contains the device design, fabrication and preliminary results.

A. INTRODUCTION

Optical attenuation and loss limit the performance of communications, switching, and computing systems. The present performance of optical fibers, optical wave guides, and holographic optical interconnects reduce the distance over which communications may take place without a repeater station. Further prohibitive losses occur when several channels carrying signals must be switched or interconnected between a selection of output channels. Such an additional loss is inherent in a crossbar switching device, for example. The main hurdles in optical computing result from the same deficiencies: the most common switches have no optical gain. These devices can not be cascaded with any efficiency without the use of electronic subsystems.

Laser amplifiers potentially solve these problems. These devices have extremely large bandwidths and can provide optical gain in an all optical computer.³⁶ The gain can be 10 dB or higher and the bandwidth can greatly exceed that of semiconductor lasers. However, optical amplifiers produce signals which are large in intensity and relatively broad in wavelength even at quiescence due to spontaneous emission. This spontaneous emission degrades performance by reducing the signal to noise ratio. Furthermore, the residual reflectivity of the facets limits the useful gain of the amplifier.

The logic gates and memory elements presently under development in the USAF Photonics Center require amplification. Integrating multiple devices on a single wafer reduces the likelihood of using AR coatings on the amplifier facets. For this reason, an array of multimode, ridge waveguided laser amplifiers with varying facet angles was designed and fabricated to perform signal restoration in integrated, optical logic gates. The work presented here evaluates these amplifiers for threshold current versus facet angle,

differential efficiency versus facet angle, and gain versus wavelength. The remainder of this report contains the background including the fabrication process, experimental testing procedures, and results and discussions for these laser amplifiers. Finally, we make some general conclusions and present some possible future work and modifications in this area.

B. BACKGROUND

Due to the low fan out of current optical logic gates, laser amplifiers are needed for signal restoration in potential integrated optical processors. Laser amplifiers use a gain section to boost the input signal in a single pass and require end facets that prevent Fabry-Perot resonance.

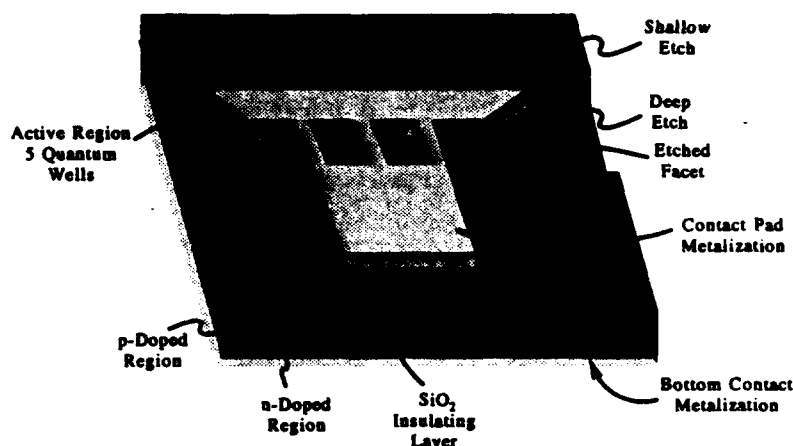


Figure 7.1: The laser amplifier with angled facets.

For multiple devices fabricated on the same wafer, it is difficult to AR coat the end facets. Therefore, one solution is to use angled facets to inhibit Fabry-Perot resonance while still providing the gain necessary to restore the input signal. Figure 7.1 shows such a structure that can easily be integrated onto a wafer of optical logic elements.

The laser amplifier arrays are fabricated from GaAs-AlGaAs Graded Index Separate Confinement Heterostructure (GRINSCH)⁹ which luminesce near 850 nm when electrically pumped. The array consists of amplifiers (figure 7.1) with various angles between the principle axis and the normal to the surface; these angles range from 0.5° to 21.8°. The angled facets reduce the amount of emission coupled

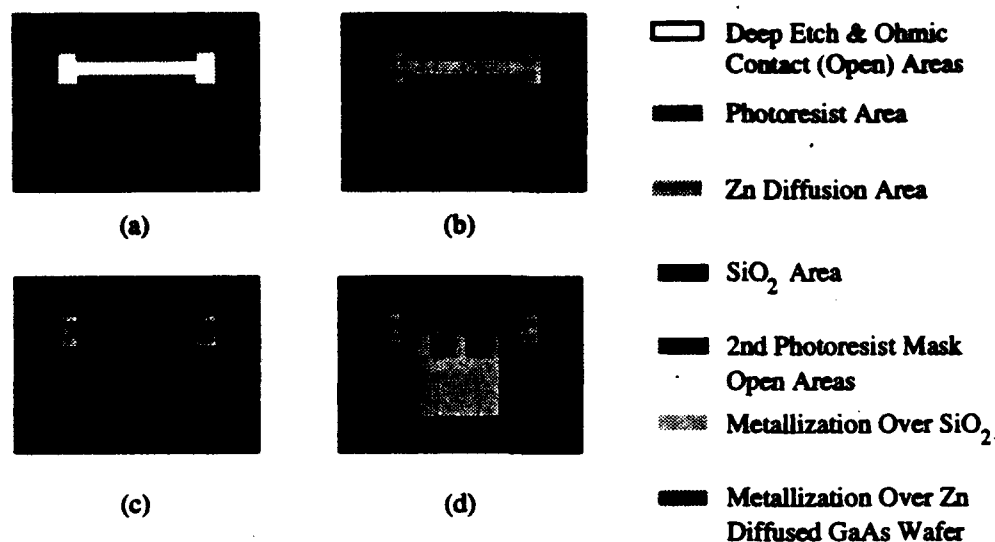


Figure 7.2: Fabrication Processing Steps: (a) 1st Photolithographic Mask, (b) Zn diffusion after RIE and Photoresist removal, (c) 2nd Photolithographic Mask for Contact Metallization, (d) Before CAIBE

back into the cavity.³⁸ The amplifier is electrically connected to a contact pad metallization by three narrow metal strips. The strips are narrow to minimize the influence on the waveguiding in the amplifier.

The amplifiers have CAIBE etched facets and ridge waveguides which are $20 \times 200 \mu\text{m}$ in area. The facets are formed by deep etches of $4.5 \mu\text{m}$.^{9,17} An SiO_2 layer performs electrical isolation as well as an etch retardation mask for the shallow etch process.^{9,16} The large metal pads supply the external bias to the devices; a layer of SiO_2 , 1300 Angstroms thick, electrically isolates the pads from the GaAs. The top P^+ and bottom N^- Ohmic contacts are made as discussed in reference 9.

Figure 7.2 displays the major steps in patterning the GRINSCH wafer. An SiO_2 layer is deposited on the wafer through Plasma Enhanced Chemical Vapor Deposition (PECVD). The 1st photolithographic mask (figure 7.2a) is patterned and developed leaving an open area for the deep etch and Ohmic contact. The SiO_2 in the dumbbell shaped open area is removed using Reactive Ion Etching (RIE), the photoresist is removed, and Zn is diffused to improve the electrical connection (figure 7.2b). A second photolithographic mask step is performed leaving open the area for contact pad and Ohmic contact metallization (figure 7.2c). A standard GaAs p-type metallization⁹ is deposited on the structure and the photoresist liftoff is performed leaving the structure in figure 7.2d. The metallized areas act as a mask for the Chemically Assisted Ion Beam Etch (CAIBE) while the SiO_2 retards the etch process slightly, and the Zn diffused portion is easily etched. Therefore, the exposed Zn diffused wafer is deep etched forming the

angled facets, the SiO_2 covered wafer is shallowly etched for electrical isolation and waveguiding, and the metallized areas are not etched at all forming the contact pad and Ohmic contact. Finally, the backside N^- Ohmic contact is deposited and alloyed⁹. Figure 7.1 shows a completely processed and etched laser amplifier.

C. EXPERIMENTAL PROCEDURES

Once fabricated, the laser amplifiers described above are cleaved and mounted for testing. Threshold current versus facet angle and gain versus wavelength are of primary interest with these devices. Figure 7.3 shows the setup used to test the amplifiers. The Argon pumped Ti-Sapphire laser system provides a range of optical wavelengths for optical probing. The amplifier is electrically driven by either the HP 8116A Pulse/Function Generator or the Keithley 238 High Current Source-Measure Unit, depending on the test being performed. Electrical and optical measurements are accomplished with the HP 54111D Digital Storage Oscilloscope (DSO) and the Anritsu MS9701B Optical Spectrum Analyzer (OSA), respectively. Included in the array of measurement equipment is a calibrated wide-area photodetector (PIN) for measuring emitted power.

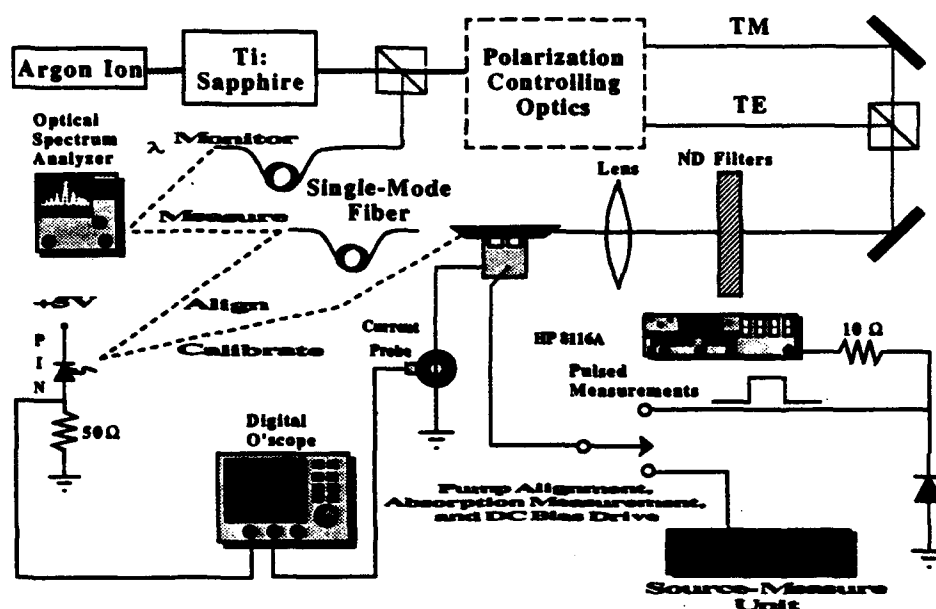


Figure 7.3: Test Setup for Basic Device Optical and Electrical Characterization

The threshold current versus facet angle tests are performed by measuring the emitted power L as a function of drive current I (L - I characteristics) for the different amplifiers. In this test, the pulse generator

(8116A) applies a triangular pulse to the amplifier. The PIN detects the emitted light, and the magnetic current probe monitors the drive current from the back N⁻ contact. These signals drive channels 1 and 2 on the digital oscilloscope, respectively, to produce the L-I curve. Threshold current and differential efficiency are measured from the L-I curve. The slope of the L-I curve's linear portion is the differential efficiency, while the threshold current is obtained by extrapolating the linear portion back to the current axis.

The gain versus wavelength measurements are performed as follows. The input beam from the Ti-Sapphire is aligned to the input facet of the amplifier by applying a reverse DC bias to the amplifier (using the source-measure unit) and observing the photocurrent from the reverse biased junction. When the photocurrent reaches a maximum, the beam is aligned with the input facet and maximum absorption occurs. Next, the input laser beam is blocked and a single-mode optical fiber probe is aligned with the output facet. This signal is maximized by applying a forward bias square pulse (using the HP 8116A) to the amplifier and adjusting the position of the fiber until the maximum signal from the photodetector circuit is observed.

Once the fibers have been aligned, the optical gain, defined as the ratio of the output I_{out} to input I_{in} intensities, is determined as follows.

- 1) The input intensity is determined by measuring the photocurrent J from the amplifier under reverse bias, converting this number to the amount of light absorbed in the amplifier and then dividing out the facet reflectivity R .

$$I_{in} = \frac{Jhc}{2e\eta\lambda R} \quad (7.1)$$

where h , c , e , η , λ are Planck's constant, the speed of light, the elementary charge, the quantum efficiency (assumed equal to unity) and the wavelength of the incident light respectively. R is a function of wavelength, facet angle, and polarization. For these preliminary measurements, both TE and TM laser light was used and R was set equal to unity.

- 2) The output intensity is obtained from the following equation:

$$I_{out} = (P - S - B) K \quad (7.2)$$

P is the peak power density obtained from the optical spectrum analyzer when the amplifier was forward biased and the laser light was applied to the input facet. S is the peak power density of the spontaneous emission from the amplifier with the same forward bias but without the input beam. B is the power density of the light scattered over the P⁺ side of the laser into the fiber. K is a calibration factor for the amount of light coupled into the fiber from the laser amplifier. To acquire this calibration factor, the emission spectrum through the fiber from the amplifier, which is operated at a fixed DC current level, is integrated over wavelength and the resulting power is divided into the power obtained by using the wide-area detector in place of the fiber.

D. RESULTS and DISCUSSION

The setup in figure 7.3 acquires the data for the L-I curves and saves it to disk for analysis. Figure 7.4 shows data obtained for amplifiers with two different angles.

The top L-I curve is for an amplifier with nearly perpendicular facets; this almost qualifies as a laser. It is easy to see the sharp knee at approximately 27 mA; the lasing threshold for this particular amplifier. The bottom curve shows a much more rounded threshold. Through extrapolation, the threshold current for this device is 44 mA. The differential efficiency for the top and bottom amplifiers is 205.5 and 115 mW/A, respectively. This shows that at higher facet angles the threshold current increases, the threshold knee is less distinct,

and the differential efficiency and emitted power decreases. This data is quantified for the complete range of facet angles in more detail below.

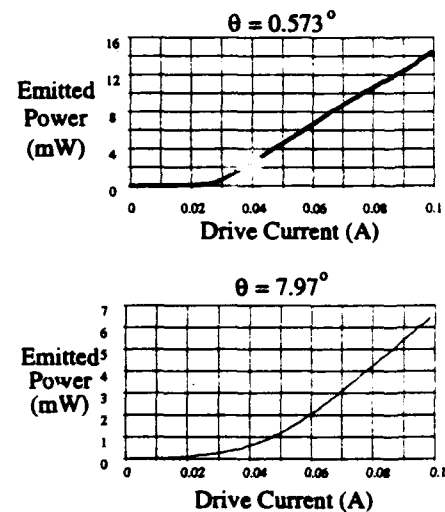


Figure 7.4: L-I Curves for Amplifiers with 0.573° (top) and 7.97° (bottom) Facet Angles

The method described above was performed on 2 sets of 40 laser amplifiers. For each set, a two point running average was performed according to

$$\langle J_{th}(\theta_i) \rangle = \frac{J_{th}(\theta_{i-1}) + J_{th}(\theta_i)}{2} \quad (7.3)$$

where J_{th} is the threshold current and θ_i are the facet angles. Threshold current versus facet angle for all 40 laser amplifiers is plotted in figure 5 and the differential efficiency appears in figure 7.6. The threshold current increases from about 25 mA to nearly 45 mA as the facet angle increases, whereas the differential efficiency is seen to decrease. Note the dip in the threshold current near 7° and the scatter for angles approaching 17° . The differential efficiency increases and then decreases over the range of facet angles with a maximum near 7° .

Gain measurements are made as stated in the experimental procedures section. Figure 7.7 shows typical raw data used to determine the gain of an amplifier. The top curve shows the spectrum with the amplifier biased and the input beam applied. These data are used to obtain P and S in equation 7.2. Essentially, the quantity $(P - S)$ is the height of the spike on the top curve. The bottom curve shows the input beam signal without the amplifier biased. These data are used to determine the value of B in equation 7.2. B is an indication of the amount of



Figure 7.5: Laser Amplifier Threshold Current versus Facet Angle

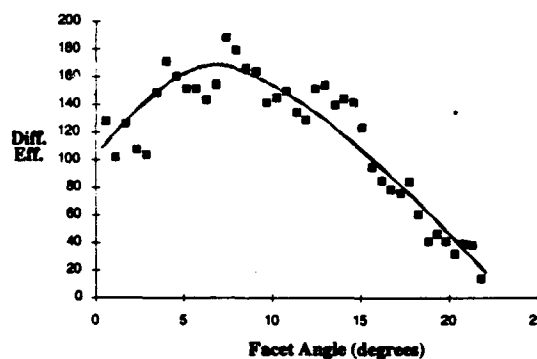


Figure 7.6: Differential Efficiency versus Facet Angle

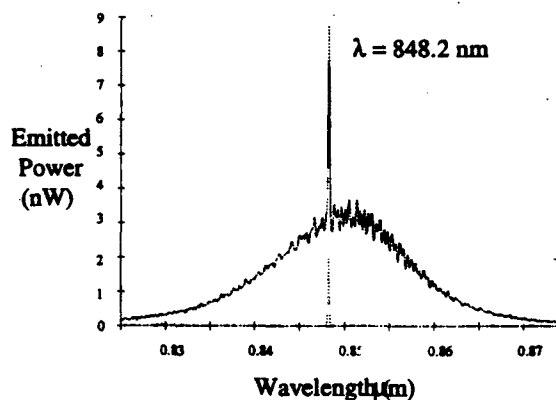


Figure 7.2: Amplifier Gain Measurement

input signal passing over the top of the amplifier. These two values are combined with the fiber coupling calibration factor, K , to determine the output intensity. This value is compared to the input intensity obtained from the photocurrent measurement to determine the amplifier's gain.

Figures 7.8a,b show the results of these gain measurements and the insets show the emission spectra of each particular amplifier at different DC current levels. Figure 7.8a and b are graphs of gain versus wavelength for the laser amplifier with 1.1° and 6.8° facet angles respectively. To obtain the figure, the noise in the raw data was averaged according to

$$\langle G(\lambda_i) \rangle = \frac{G(\lambda_{i-1}) + G(\lambda_i) + G(\lambda_{i+1})}{3} \quad (7.4)$$

where i labels the sequence of data points taken by the optical spectrum analyzer.

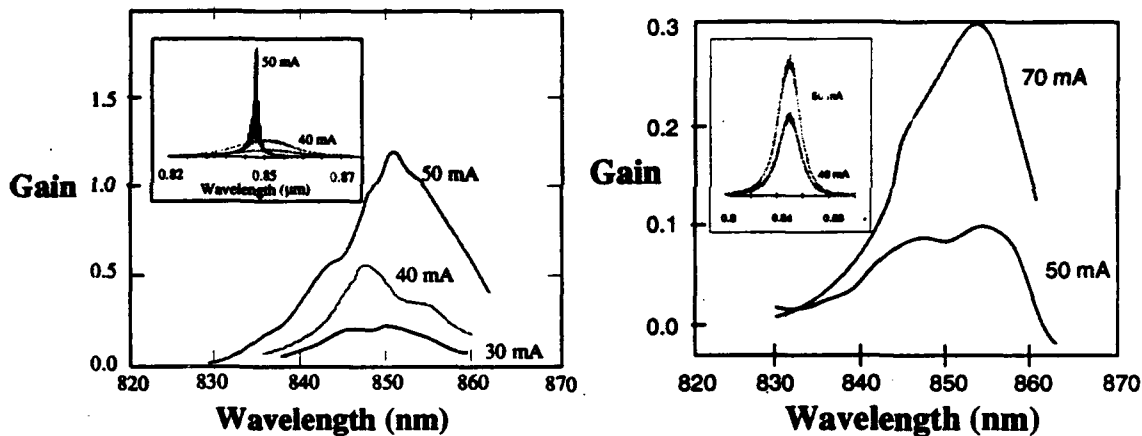


Figure 7.8: Gain vs. Wavelength for Laser Amplifiers with (a) 1.1° and (b) 6.84° Facet Angles (Insets show spectra at different bias currents for each laser amplifier.)

These gain curves are not particularly encouraging; however, they do display some expected characteristics. The spectra of the smaller facet angled amplifiers indicates that it lases with a DC bias at 50 mA. Also, the spectrum at 50 mA shows the multimodal behavior of these $20\text{ }\mu\text{m}$ wide amplifiers. The amplifiers with larger angles do not lase even at 70 mA. The gain curve of the 1.1° amplifier shows a slight amplification with a 50 mA bias current. Both amplifiers display greater amplification in their operating region of approximately 845 to 855 nm. As expected, increasing the bias current increases the gain, and larger angles provide less gain at the same bias current.

The maximum attainable gain, threshold current, and differential efficiency are controlled by the amount of optical feedback of light in the laser amplifier due to the facets. In general, the attainable gain will increase with decreasing facet reflectivity before the amplifier begins to oscillate on its own. The threshold current should increase and the differential efficiency should decrease with increasing mirror reflectivity³⁹; this is confirmed by the preliminary data presented. The dip in the threshold current near 7° is believed due to the mode in the waveguide reflecting once off the upper sidewall in figure 7.1. For angles near 17° , the spontaneous emission in the cavity is totally internally reflected from the facets. The scatter is believed due to the fact that no clear linear portion in the L-I curve was observed for which a reliable threshold current could be extrapolated. The differential efficiency showed a rise as the facet angle increased to 7° and then a gradual decrease. This behavior is in agreement with figure 7.3 in reference 39.

E. CONCLUSIONS

These multimode laser amplifiers did not perform as well as expected with the best attainable gain of slightly over 1. However, some generalizations can be made for future developments. Increasing the facet angle inhibits Fabry-Perot resonance, causes a decrease in total emitted power, increases lasing threshold with the exception of around 7° due to the single reflection off the upper sidewall, and slightly increasing then decreasing differential efficiency. The gain measurements displayed increasing gain with decreasing facet angle and increasing DC bias current. The center of the gain curves is 845 to 855 nm.

There were a number of difficulties during testing these amplifiers that the next fabrication run will overcome. The amplifiers have a multimode emission. There is the dip at 7° in the threshold versus facet angle plot. It is difficult to determine the amount of light coupled into the amplifier (input intensity) and the amount of light passing over the structure can cause erroneous gain measurements. To eliminate these problems, the next round of fabrication will include the following modifications.

- 1) $4\text{ }\mu\text{m}$ wide active region amplifiers will provide single-mode operation.
- 2) Opposing angled facets will eliminate the possibility of modes bouncing off the upper sidewall and causing lower thresholds at increasing facet angles.

- 3) Some amplifiers will be constructed with a 90° bend to eliminate the coupling of the input beam over the top of the device.
- 4) Some amplifiers will have lasers integrated for the input so that the amount of light coupled into the amplifier is easily determined by measure the power out of the opposite side of the laser.
- 5) An attempt will be made to AR coat integrated laser amplifiers by depositing an AR coat across the entire wafer and using e-beam lithography to define the AR coating at the facets.

These modifications should prove to eliminate the majority of problems encountered during testing and should provide a more accurate measurement of the amplifiers' gain.

VIII. A SQUARE BROAD-AREA MULTIPLE QUANTUM WELL LASER

A new single element broad area laser has been designed, fabricated and tested for use as an integrated optical memory element or logic gate. The design incorporated a square gain section and an intracavity saturable absorber for each of the two orthogonal cavities. The devices lased in two spatially orthogonal modes which could be independently modulated by the two saturable absorbers.

A. INTRODUCTION

Broad area lasers to date have consisted of devices with fairly large length to width ratios.^{40,41} Recently, broad area lasers have been fabricated with a length to width ratio of unity. With mirrors on all four sides, these lasers can operate in orthogonal directions competing for the same gain.²

These new single element, broad area, semiconductor lasers are suitable for optical memory elements, optical logic gates and modulators. Two variations of the laser were designed, fabricated and tested. One laser consisted of a Gain-Guided Arrayed (GGA) gain section and the other had a Uniformly Pumped (UP) gain section. Primary attention focused on the GGA laser but the results were compared with those from the UP laser. The GGA laser, shown in Fig. 8.1, is square in shape with laser emission possible in either of two orthogonal directions. Each of the two orthogonal cavities contains a saturable absorber which can modulate the laser emission. A patterned SiO₂ layer under the current carrying metalization on the gain section provided an Ohmic contact and some degree of gain guiding for both directions. The UP laser does not have the SiO₂ on the gain section; consequently, that entire section is electrically pumped.

This publication consists of three sections. The Fabrication section details the fabrication process used. The Experimental Result section contains a discussion of the experimental procedures and results for tests of the laser and saturable absorbers. The Discussion and Conclusion section contains the authors' interpretation of the results and possible future work on memory elements.

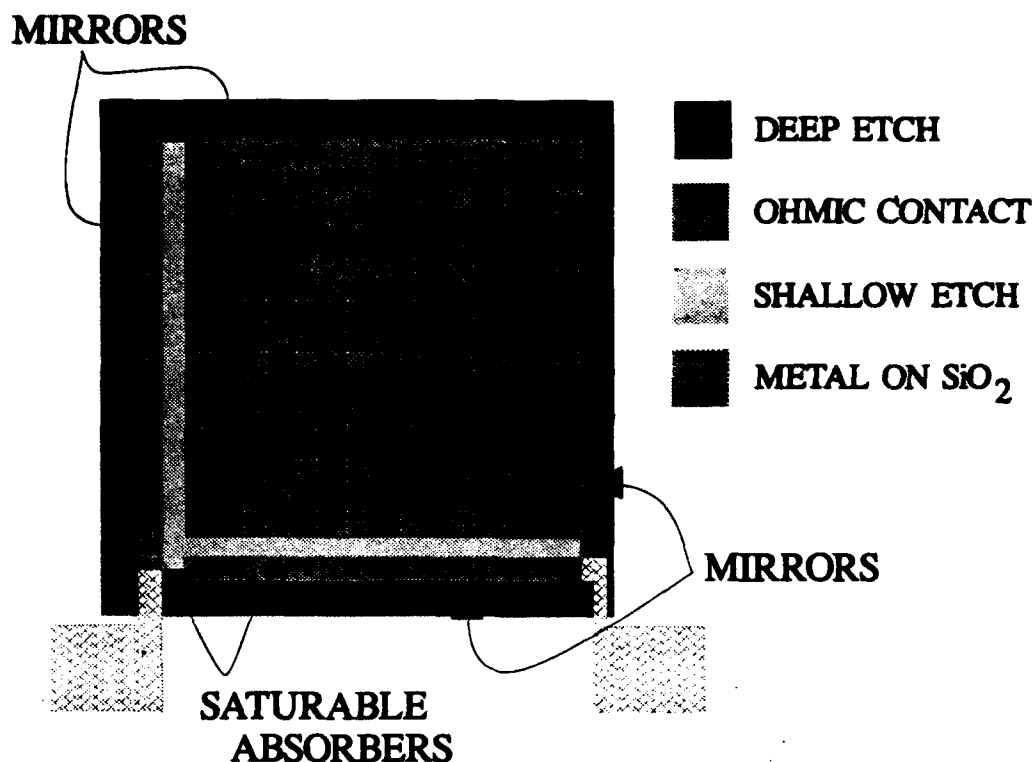


Figure 8.1: A mode switched optical memory element incorporating a Gain Guided Arrayed (GGA) broad area laser capable of lasing in either of two orthogonal directions. The saturable absorbers control stimulated emission in the two directions. The four mirrors are formed by deep etches through the active region by Chemically Assisted Ion Beam Etching. Shallow etches into the top cladding layer provide electrical isolation between the saturable absorbers and the gain section. For the GGA laser, a patterned SiO_2 layer under the metallization allows for gain guiding. The Uniformly Pump (UP) laser (not shown) does not have the SiO_2 gain masking on the central square gain section.

B. FABRICATION

The devices were fabricated from a GaAs-AlGaAs graded index, separate confinement, multiquantum well heterostructure with five quantum wells.¹¹ The main laser was $200 \times 200 \mu\text{m}$ in area and the modulators were $3 \times 200 \mu\text{m}$. Shallow etches of $3 \mu\text{m}$ wide and $1.75 \mu\text{m}$ deep through the cap and half way into the $\text{P}^+ \text{Al}_{0.5}\text{Ga}_{0.5}\text{As}$ cladding layers provided electrical isolation between the modulators and the laser. The four mirrors were formed by deep etches of $4.5 \mu\text{m}$. A 1300 angstrom SiO_2 layer was used as electrical isolation as well as an etch retardation mask for the shallow etch process.¹⁶ Isolated metal pads were provided to supply external bias to the modulator sections. The top P^+ Ohmic contacts were made by diffusing zinc through openings in the SiO_2 layer to the depth of $0.3 \mu\text{m}$, evaporating Ti, Pt, Au over the surface, and using a liftoff process to remove regions of unwanted metal. A bottom N^- contact was made by depositing layers of Ge, Ni, Ag and Au after lapping the bottom of the wafer so that the total

wafer thickness was about 150 μm . Both the P and N Ohmic contacts were simultaneously alloyed prior to cleaving out and testing the devices. Devices were patterned with both uniform gain over the 200 μm square region and with the gain section patterned into two intersecting gain guided arrays. These arrays consisted of two orthogonal sets of seven 15 μm wide guides on 25 μm centers as depicted by Fig. 8.1.

C. EXPERIMENTAL RESULTS

Lasers were tested for (1) the power output vs. injected current (L-I), (2) the emission spectra, (3) the divergence angle, and (4) the effect of the modulators on the lasing state and the spectrum. A comparison was made between the UP and GGA lasers.

The measurements were performed as follows. (1) L-I curves were obtained by cleaving one of the heterostructures through the deep etch, thereby exposing one of the facets. A fast, large area photodetector was moved to within 0.5 cm of the laser facet. A series of low duty cycle triangular current pulses was applied to the lasers. The data was displayed as photodetector current vs. pump current on a digital oscilloscope. (2) Optical emission spectra were obtained by angling an optical fiber with a 60 μm core just above the deep etch and within 10 to 20 μm of the laser facet. The drive current consisted of rectangular current pulses with the same temporal profile as those for the L-I curves. The spectrum of the light from the fiber was measured using an Anritsu optical spectrum analyzer set in an averaging mode. (3) The divergence angle was obtained by placing a CCD camera next to the laser with the cleave through the deep etch. After photographing the transverse mode pattern, the camera was displaced away from the laser by an additional 5 mm and the pattern was again photographed. The separation of two lateral lobes was then compared between the two photographs to determine the divergence angle. (4) The effect of the modulators on the lasing state and spectra was obtained in a manner similar to the emission spectra except that the voltage on the modulators was varied.

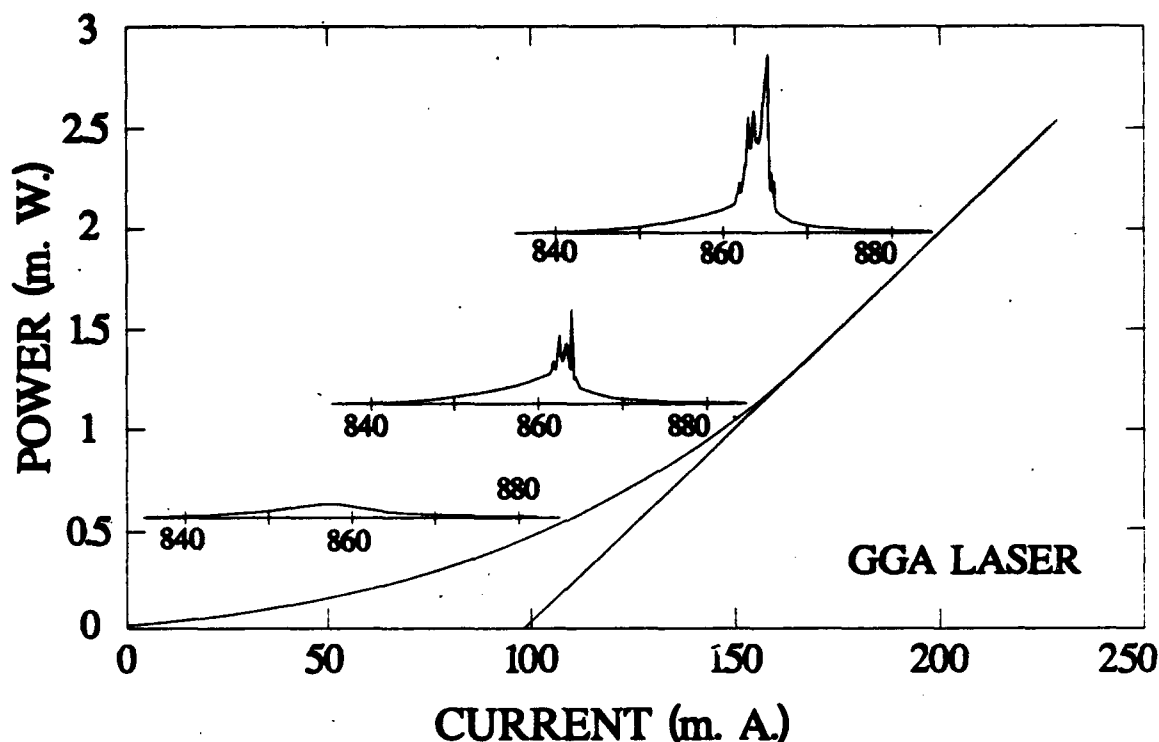


Figure 8.2: Emitted optical power versus drive current for the GGA laser. The tangent line yields the extrapolated threshold current of 100 mA. The inset plots show the spectra at currents of 100, 150 and 200 mA.

Figure 8.2 shows the L-I curve for the GGA laser with both modulators grounded. The straight line portion of the graph yields a differential efficiency of 0.02 W/A and an extrapolated threshold current of 100 mA. The straight-line construction for extrapolating the threshold current is also shown in the figure. The inset graphs show the emission spectra for 100, 150 and 200 mA. The emission is entirely spontaneous at 100 mA. For 150 and 200 mA, the dominant lasing mode occurs near 865 nm.

The transverse mode pattern was obtained as previously discussed. It showed many closely spaced nodal points and yielded a divergence angle of 30 degrees.

The emission spectra for the GGA and UP lasers with drive currents of 150 mA were measured for various modulator biases. The insets in Figs. 8.3 and 8.4 show the block diagram of the broad area laser with two orthogonal directions defined. The laser emission in the forward direction of the fiber, denoted by F, is coupled into the multimode fiber and monitored. Laser emission from the orthogonal cavity, denoted by X and termed the crossed cavity, is not monitored. The results of varying the voltage V_f on the modulator within the GGA laser appear on the left side of Fig. 8.3. The GGA laser is extinguished in the direction F for reverse bias voltages V_f larger than -2.5 volts. Applying reverse

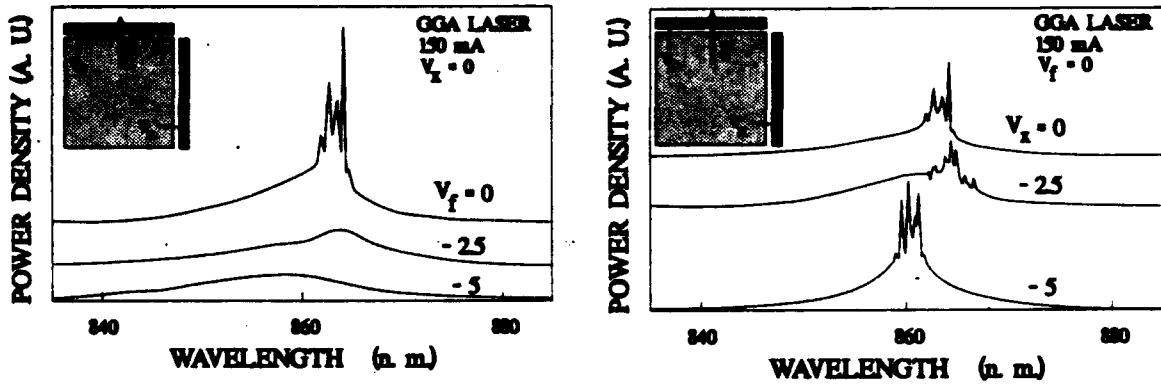


Figure 8.3: LEFT: Spectra for GGA laser emission through the saturable absorber with variable voltage V_f ; the other saturable absorber is grounded. Reverse biasing V_f cuts off laser oscillation. RIGHT: Spectra for GGA laser emission through the grounded saturable absorber; the voltage on the other saturable absorber varies. Reverse biasing the spectrum to red shift and changes the peak intensity.

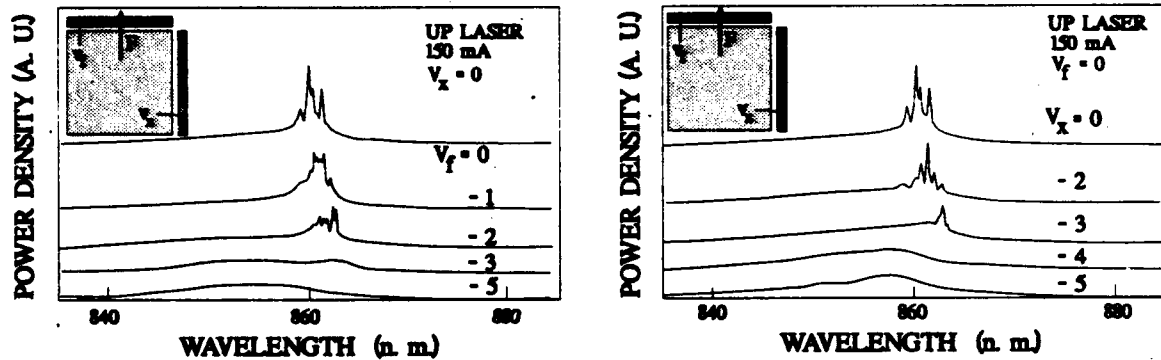


Figure 8.4 LEFT: Spectra for UP laser emission through the saturable absorber with variable voltage V_f ; the other saturable absorber is grounded. RIGHT: Spectra for UP laser emission through the grounded saturable absorber; the voltage on the other saturable absorber varies.

bias V_x to the modulator in the crossed cavity produces remarkably different behavior as shown in the right side of Fig. 8.3. The GGA laser generates stimulated emission in the F direction for all values of reverse bias V_x ; the intensity is maximum and the spectrum is blue shifted for voltages near $V_x = -5$. Thus, the forward cavity of the GGA laser produces peak emission when the stimulated emission in the crossed cavity falls off. In contrast to the GGA laser, reverse bias applied to either modulator of the UP laser extinguishes the laser oscillation. The dominant mode is near 865 nm for the GGA laser and 860 nm for the UP laser.

D. DISCUSSION AND CONCLUSIONS

The broad area lasers appear to lase simultaneously in two orthogonal directions when the modulators are grounded. However, the spectra show that the GGA and UP lasers operate differently. The fact that the GGA laser reaches peak intensity in one direction when the intensity in the other direction

falls off suggests that the emission from the two cavities can be independently controlled by the two modulators; these results imply that two distinct cavities exist for the GGA laser. For the proper choice of modulator bias voltages, it is possible to switch lasing directions; however, latching was not observed. The situation is different for the UP laser. Each saturable absorber affects the oscillation in both directions. Increasing the reverse bias on either modulator decreases the emitted power with negligible shift of the operating wavelength. Thus the two cavities are coupled. The data suggest that two distinct cavities do not exist for the UP laser and that it oscillates in a spatial mode which, in part, might consist of a closed path with near total internal reflection at the four mirror facets. Apparently, the geometry of the wave guiding for the GGA laser suppresses this ring mode. Both types of lasers produce stimulated emission simultaneously in the two orthogonal directions when the two modulators are grounded. However, it is yet to be determined whether the GGA laser is randomly switching between two orthogonal spatial modes or if the two modes use different portions of the same gain curve to sustain oscillation.

The broad area laser shows promise for use as an optical memory element. The saturable absorbers stabilize the switching of the laser by providing bistability in the lasing characteristics. Under proper biasing conditions, the saturable absorber in the path of a laser beam is bleached, resulting in an increased gain for that direction. The other saturable absorber is highly absorbing, resulting in a lower gain for oscillation in that direction. As a result, one cavity has a higher Q than the other. Switching then occurs by introducing light into the cavity or by changing the voltages on the saturable absorbers. Such behavior has been shown to exist in the GGA laser but not the UP design. Further work will be required to determine the conditions for latching.

IX. AN OPTICAL NOR GATE BASED ON GaAs-AlGaAs HETEROSTRUCTURE LASERS

This chapter discusses the design, fabrication and test of an optical NOR gate consisting of three GaAs-AlGaAs heterostructure lasers. The lasers have etched ridge waveguides and total internal reflection mirrors. Either of two *quench* lasers can optically quench a *main* laser to achieve the NOR operation. Data is presented for the quench phenomenon and for the characteristics of the emitted optical flux versus the injected current for the main lasers.

A. INTRODUCTION

Considerable effort has been invested in the development of optical logic gates and memory elements for the possible future development of an integrated optical computer.^{1,2} High laser threshold currents and the lack of integration techniques have limited the usefulness of early designs for logic gates and memory elements based on semiconductor lasers. Recent developments in the epitaxial growth techniques for quantum well heterostructures and the processing techniques have since made the early designs attractive for optical computing purposes. One such device is the optical inverter which consists of semiconductor laser diodes and operates on the principle of laser quenching.⁴²

An optical NOR gate (figure 9.1) has been designed, fabricated and tested which operates similarly to the optical inverter.¹⁵ The gate consists of three GaAs-AlGaAs heterostructure lasers which emit at 860 nm. The main laser can be quenched off by either of the two side lasers for the NOR operation. Each quench laser is divided into two parts across the gain region of the main laser so that the quench and main

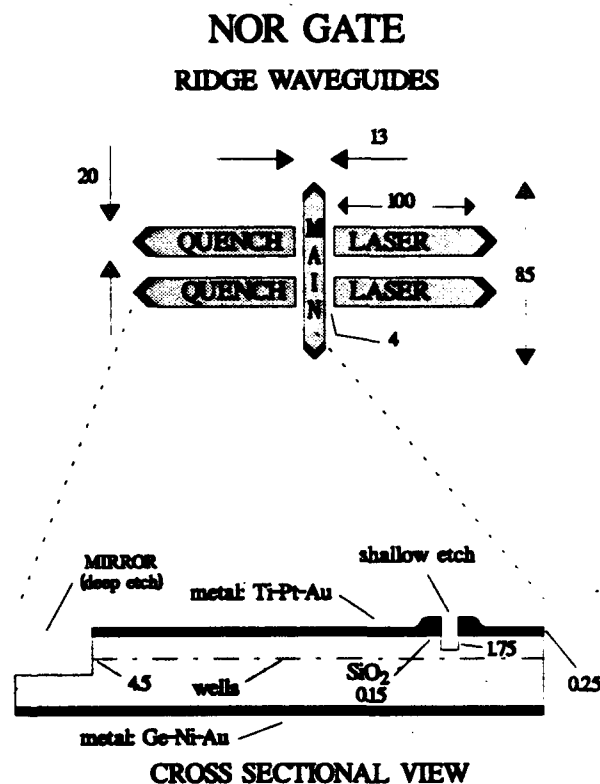


Figure 9.1: The optical NOR gate (top) and the cross sectional view (bottom) showing the layers and the etch depths for the mirrors and waveguides. The sizes are in microns.

laser cavities overlap; the two halves of the quench laser are electrically connected in parallel. The lasers employ Total Internal Reflection (TIR) mirrors⁴³ to improve the laser threshold currents and decrease the power consumption of the device. In principle, the reflectivity of a TIR mirror can approach 100% while the etched flat mirrors can have intrinsic reflectivities no larger than about 34%. The lasers have ridge waveguides and mirrors which were etched in a Chemically Assisted Ion Beam Etcher (CAIBE). The inset to Figure 10.1 shows the various layers of the device and the depths of the etch for the mirrors and the waveguides.

The next three sections contain discussions of the fabrication process,^{9,16} experimental procedure¹⁰ and conclusions.

B. FABRICATION

The NOR gates were fabricated from Graded Index Separate Confinement Heterostructure (GRINSCH) GaAs-AlGaAs Multiple Quantum Well wafers as described in chapter 3. The NOR gates had CAIBE etched mirrors and ridge waveguides. The main lasers were $13 \times 85 \mu\text{m}$ long and the quench lasers were about $20 \times 200 \mu\text{m}$. Shallow etches of $2 \mu\text{m}$ wide and $1.75 \mu\text{m}$ deep into the P^+ GaAs, shown in the expanded cross sectional view of figure 9.1, provided up to $1\text{K}\Omega$ of electrical isolation between the top pads for the lasers. The mirrors were formed by deep etches of $4.5 \mu\text{m}$.^{9,17} An SiO_2 layer was used as electrical isolation as well as an etch retardation mask for the shallow etch process.^{9,16} Large metal pads (not shown) were connected to the devices to supply the external bias; a layer of SiO_2 , 1300 Angstroms thick, electrically isolated the pads from the GaAs. The top P^+ and bottom N^- Ohmic contacts⁴⁴ were made as discussed in chapter 3.

C. EXPERIMENTAL

Two series of experiments were performed. The first series of experiments obtained the optical flux (L) from the main lasers as a function of the bias current (I). The main lasers were pulsed with $5 \mu\text{sec}$ wide pulses, separated by 2 msec. The pulse was approximately Gaussian in the time domain. A 50Ω sampling resistor was used to determine the current. Light escaping from the tip of the main laser TIR mirror was coupled into a single mode fiber and to a pin photodiode circuit. A single mode fiber, with one

end positioned next to a facet of the main laser, routed the illumination to a pin photodiode circuit. The second series of experiments tested the laser quenching effect. Again a single mode fiber monitored the main laser response; this time with both main and side lasers being pulsed. A square pulse was applied to the main lasers for 10 microseconds. During this time, a triangular pulse was synchronously applied to the quench lasers for 10 microseconds. In both cases, signals proportional to the optical flux and the current were plotted on a digital oscilloscope.

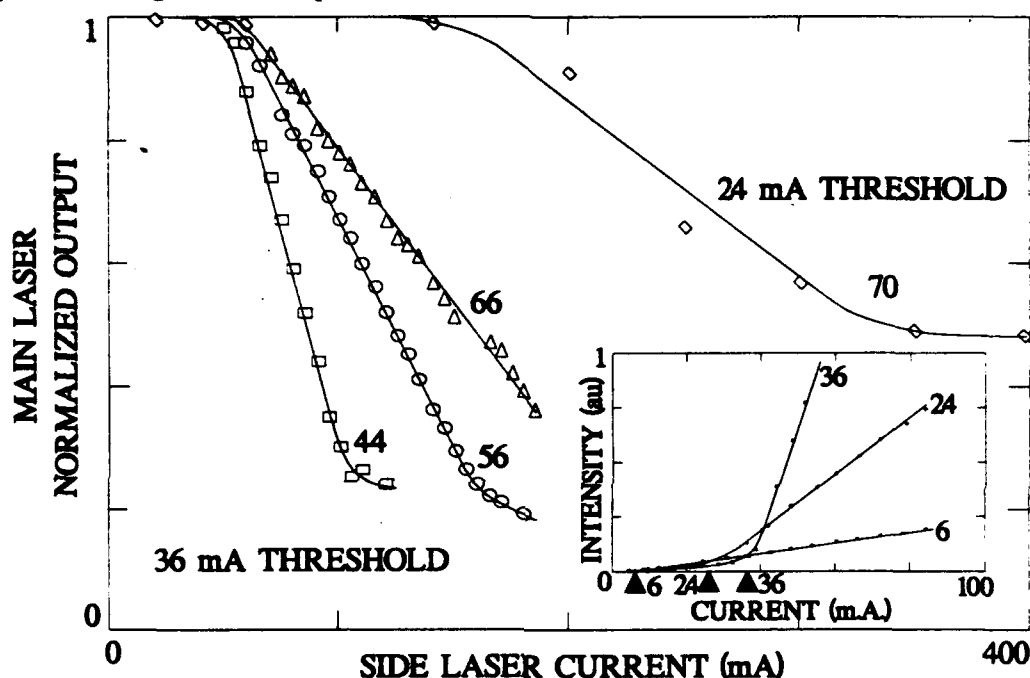


Figure 9.2: Normalized emitted optical flux from the main lasers of two NOR gates as a function of the current into the quench lasers; the NOR gates have main lasers with threshold currents of 24 and 36 mA. The quenching effect was observed for the 36 mA NOR gate with 44, 56 and 66 mA of current in the main laser and for the 24 mA NOR gate with 70 mA into the main laser. The inset shows the L-I curves for the main lasers in three different NOR gates; the numbers next to the shaded triangles indicate the threshold currents.

The L-I curves for three different main lasers with TIR mirrors and etched ridge waveguides appear in the inset to figure 9.2. Thresholds of 6, 24, and 36 mA were observed. The variation in threshold current stems from the variation in processing across the surface of the wafer; the lasers with the lower threshold currents most probably had more reflective mirrors. It was conjectured that rounding at the tip of the mirror increased the light transmitted through the mirror, thus increasing the required threshold current.

Of the NOR gates tested, the results from two with differing threshold currents for the main laser appear in figure 9.2. The graph plots the emitted power from the main laser as a function of the current injected

into one of the quench lasers; the power has been normalized to unity. The set of three curves correspond to the device with the 36 mA threshold current for the main laser, while the right most curve corresponds to the device with the 24 mA threshold current. The optical flux from the 6 mA threshold device was too small for accurate measurements. The values of the current injected into the main laser parameterize the curves. Approximately 80% of the optical power from the main laser with the 36 mA threshold can be quenched. Note the linear decrease in main laser intensity as the side laser current increases. Also note that more side laser current is required for larger main laser currents in order to maintain a constant amount of quench. The gate with the 24 mA threshold for the main laser required larger quench currents than the gate with the 36 mA threshold for the main laser; in addition, the main laser could be quenched by no more than about 50%.

The quenching cannot be attributed to electrical crosstalk between the metal pads on the P^+ side of the wafer. Both the main and side lasers must be electrically biased in the same way. Therefore, electrical crosstalk would cause the current in one laser to increase as the current in the others increase. In this case, the power emitted from both must increase. Any resistance in the N^- layer or in the circuit connecting the metal on the N^- layer could give rise to curves which resemble the quench curves of figure 9.2; this N^- layer and its metallization serves as the common electrode for all of the devices. An increase of current through the quench laser would (1) increase the voltage drop across this common N^- resistance, (2) lower the voltage across the main laser, and therefore, (3) lower the emitted irradiance. But, based on the doping level, the thickness of the N^- layer, and the device sizes, the typical resistance in this layer is on the order of 0.1Ω .²⁷ Any voltage drop across this resistance would be relatively small and could not account for the quench data.

D. DISCUSSION

The lasers with TIR mirrors have lower threshold currents but also lower differential efficiency (dI/dI for I above threshold in the inset to figure 9.2) than similar lasers with flat etched mirrors. Optical losses such as scattering in the cavity, diffraction and mirror transmittance determine the differential efficiency,

and the threshold current.³⁹ The differential efficiency and threshold current decrease as the quality of the mirrors increases.

The quench curves in figure 9.2 consist of the Spontaneous Emission Region (SER), the Linear Region (LR) and the Saturation Region (SR). The SER corresponds to side laser currents smaller than about 50 mA; this region is due to the lack of stimulated emission in the quench lasers. The irradiance from the main laser can increase to values larger than 1 if the resistance between the main and quench lasers is sufficiently small or if the spontaneous emission from the quench laser aids the pumping of the main cavity.² LR refers to that part of the graph where the irradiance from the main laser linearly decreases. For this region, a photon from either the quench or main laser cavity can stimulate the emission of a photon from electron-hole recombination in such a way that the wave vector of this emission is parallel to either the quench or main laser cavity respectively.⁴⁵ However, above threshold, the photon density in the quench laser is linearly proportional to the quench laser pump current. Thus, the probability of interaction between the photons from the quench laser and electron-hole pairs in the common cavity increases linearly. As a result, the gain of the main laser linearly decreases to a fixed value. Main lasers operating at higher current densities require larger quench laser currents to achieve the same amount of quench. The SR, the region where the irradiance saturates, occurs for relatively large values of the quench current. For small common cavity volumes, the main laser cannot be quenched and the intensity of the stimulated emission corresponds to the observed saturation level. For volumes of the common cavity sufficiently large to quench the main laser, the observed saturation level is due to the spontaneous emission from the main laser.

E. CONCLUSIONS

An optical NOR gate has been designed and presented for use as an optical logic element in an integrated optical processor. The design incorporated TIR mirrors. The laser quenching was tested in logic gates with coupled cavities and TIR mirrors. Further work will be required to satisfactorily explain the larger quench laser current required to quench the main lasers with better mirrors.

X. AN OPTICAL RS FLIP FLOP

We discuss the design, fabrication and test of an optical RS Flip-Flop as an integrated optical memory element. The Flip-Flop has three GaAs-AlGaAs heterostructure lasers with total internal reflection mirrors. A main laser incorporates a saturable absorber to develop the bistable output characteristics. A pump laser bleaches the absorber to set the logic 1 state. A third laser quenches the main laser to reset the device to logic 0. Experiments and data for the laser quenching were presented in the previous chapter. The experiments and data for the bistability are presented here.

A. INTRODUCTION

Considerable effort has been invested in the development of optical logic gates and memory elements for the realization of an integrated optical computer.¹ High laser threshold currents and the lack of integration techniques limited the usefulness of early designs for logic gates and memory elements based on semiconductor lasers. Recent developments in the epitaxial growth techniques for quantum well heterostructures and the processing techniques have since made the early designs attractive for optical computing purposes.

An optical RS Flip-Flop has been designed to function as an optical memory element. The flip-flop can be divided into 3 functional blocks (refer to figure 10.1). (1) A main laser cavity contains *gain* and *saturable absorber* sections^{7,42,46,47} which induce bistable output characteristics; this functional block provides the logical 0 or 1 state. (2) An external laser *pumps* the saturable absorber and *sets* the output to the logic 1. (3) A second external laser quenches^{15,43} the main laser and *resets* the output to the logic 0. These lasers are monolithically integrated on AlGaAs-GaAs quantum well heterostructure and they emit at 860 nm. The main cavity has one Total Internal Reflection (TIR) mirror⁴³ and a flat etched mirror which separates it from the pump laser. Reflections can occur at the discontinuity in the index of refraction accompanying the electrical isolation between the pumped and unpumped regions; thus the cut across the electrode is angled to inhibit the formation of a shorter cavity within the main cavity. The quench laser is divided into two parts across the gain region of the main laser⁴³ so that the quench and main laser cavities

overlap; the two halves of the quench laser are electrically connected in parallel. All four gain sections have ridge waveguides but the voltage controlled saturable absorber is unguided when it is reverse biased.

The operation of the flip-flop depends on the ability of the pump and quench laser to set and reset the output state of the main cavity respectively. Figure 10.1 shows a qualitative plot of the intensity of the light emitted from the main laser versus the current into the gain section. The current in the main laser gain section is adjusted to point *M* where the output intensity can be in either of two states. Assume that initially the output of the main laser corresponds to a point on the lower branch of the hysteresis loop. A momentary optical pulse from the pump laser bleaches the absorber, lowers the threshold current below point *M* and, therefore, sets the output to the upper branch of the hysteresis loop. The bistable nature of the gain-absorber pair ensures that the output will remain on the upper branch for times longer than the width of the pulse. When a momentary optical pulse from the quench laser stimulates emission in the common cavity, the wavevector of this stimulated emission is parallel to the cavity of the quench laser instead of the main laser. This process reduces gain in the main cavity, raises the lasing threshold current and, thereby, resets the output of the main laser to the lower branch of the hysteresis curve.

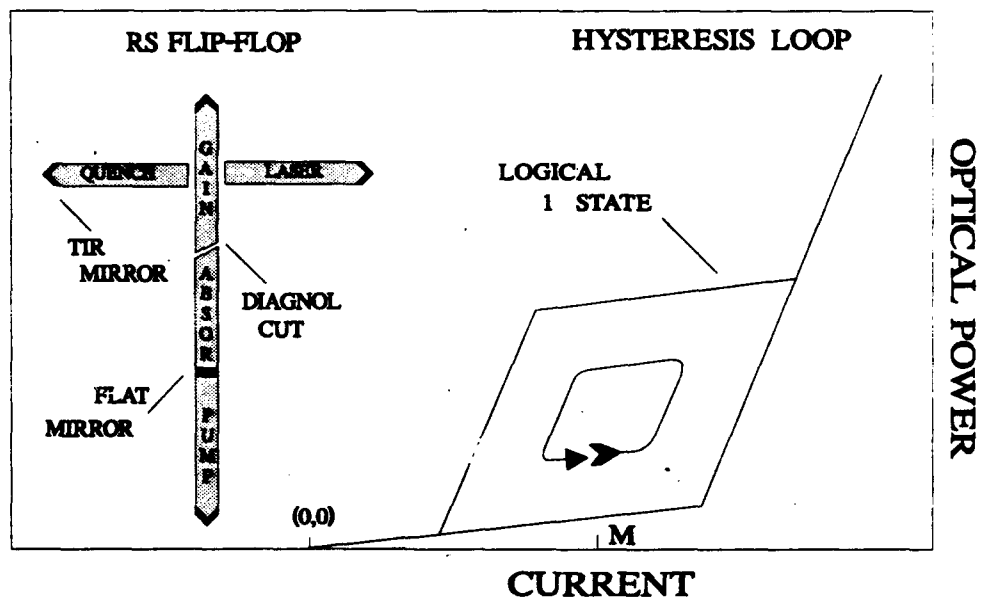


Figure 10.1: The RS Flip-Flop and the hysteresis in the L-I characteristics. Scale: each section is on the order of $5 \times 100 \mu\text{m}$.

Two of the three functional blocks of the RS flip-flop were fabricated and tested. Optical NOR gates were fabricated to test the effects of quenching as discussed in the previous chapter. Gain - absorber pairs were constructed to test for the hysteresis effects. The NOR gates had ridge waveguides and mirrors which were etched in a *Chemically Assisted Ion Beam Etcher* (CAIBE). The gain - absorber pairs had gain guided lasers, unguided saturable absorbers and cleaved mirrors; these devices were constructed with a variety of lengths for the gain and absorber sections. Both quenching and hysteresis were observed.

The remainder of this chapter is divided into three sections: fabrication, experimental and discussion. The Fabrication section briefly describes the fabrication process.⁹ The Experimental section contains a brief discussion of the experimental apparatus¹⁰ and the results of the hysteresis experiments. The Discussion section contains the authors' interpretation of the data.

B. FABRICATION

All of the devices were fabricated from GaAs-AlGaAs quantum well as shown in chapter 3. The NOR gates and gain-absorber pairs fabricated (refer to figure 10.2) had CAIBE etched mirrors and ridge waveguides¹⁶. For further information on the fabrication of the NOR gates, refer to the previous chapter.

The gain-absorber pairs were fabricated with gain-guided gain sections and unguided, voltage controlled saturable absorbers. The processing steps were the same as for the NOR gate excluding the dry etching used to delineate the waveguides and mirrors. The structure appears in figure 10.2. The lengths in microns of the saturable absorber and gain sections are given by $L_a = 150 + 50n$ and $L_g = 350 - 50n$ for the integers $n \in [0,3]$. These devices had 10 μm wide, multimode waveguides.

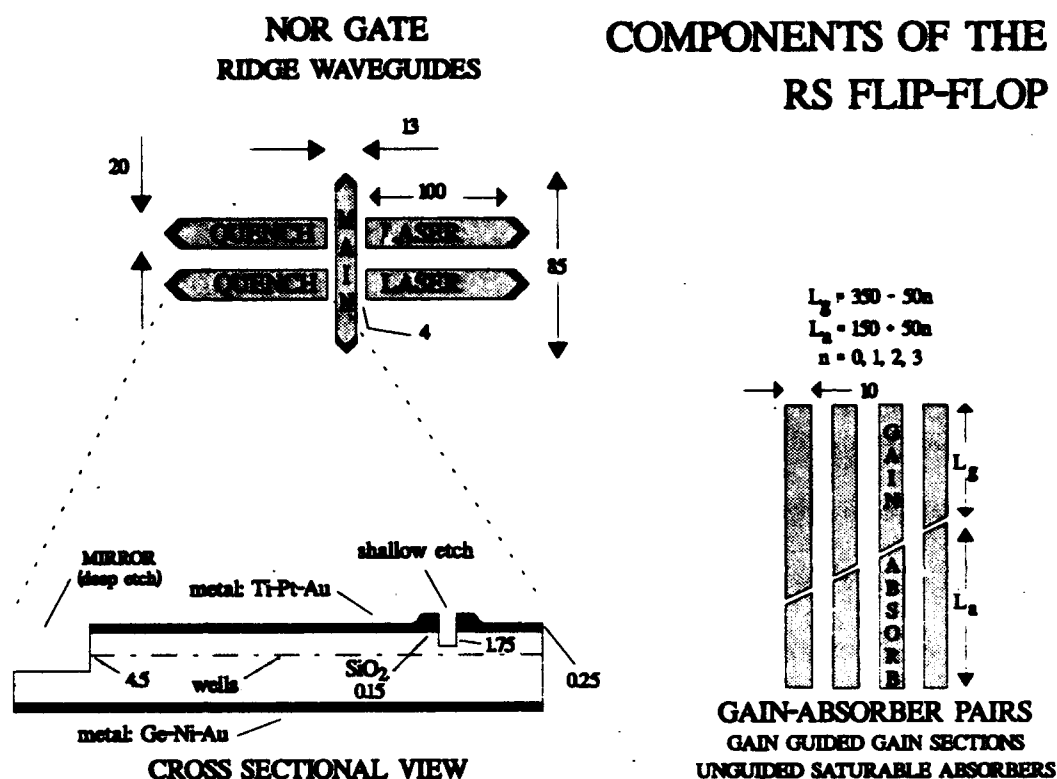


Figure 10.2: The components of the RS flip-flop. Laser quenching was tested with the NOR gates. The cross sectional view shows the layers and the etch depths for the NOR gate. The gain absorber pairs had gain-guided gain sections and unguided saturable absorbers.

C. SATURABLE ABSORBER EXPERIMENTS

The saturable absorber plays the key role in the RS flip-flop. It must induce the hysteresis loop shown in figure 10.1 and it must be capable of being bleached by illumination from a secondary laser in such a way that the main cavity begins to lase from an initially off state. The saturable absorber experiments include tests for (1) the hysteresis induced in the L-I curve of the main laser and (2) the width of the hysteresis loop as a function of the applied voltage.

In one series of experiments, ridge guided gain-absorber pairs were tested for hysteresis in the L-I characteristics. These pairs included those with (1) wet and CAIBE etched waveguides, (2) various lengths of gain and saturable absorber sections and (3) single and multimode waveguides. Hysteresis was not observed in any of the ridge guided devices. In another series of experiments, hysteresis was observed in devices with gain guided gain sections and unguided saturable absorbers; these devices are depicted in figure 10.2.

Intensity-Voltage curves (I-V) were determined for the gain and saturable absorber sections. Hysteresis was observed at peak current levels approaching 400 mA in the gain section. The experimental setup appears in the inset to figure 10.3. A pulse from a function generator was amplified and applied to the gain section of the laser cavity. The pulse consisted of the positive half of a sine wave and was generally 15 μ s long with 2 ms between pulses. The saturable absorber was reverse biased by a DC supply. The current injected into the gain section was determined by monitoring the voltage developed across a 10 Ω resistor placed in series with that section. One end of a single mode fiber probed the optical emission from the saturable absorber; the other end applied the optical signal to a PIN diode. The drive voltage and PIN signals were viewed on a dual trace digital oscilloscope as ch 1 vs. ch 2.

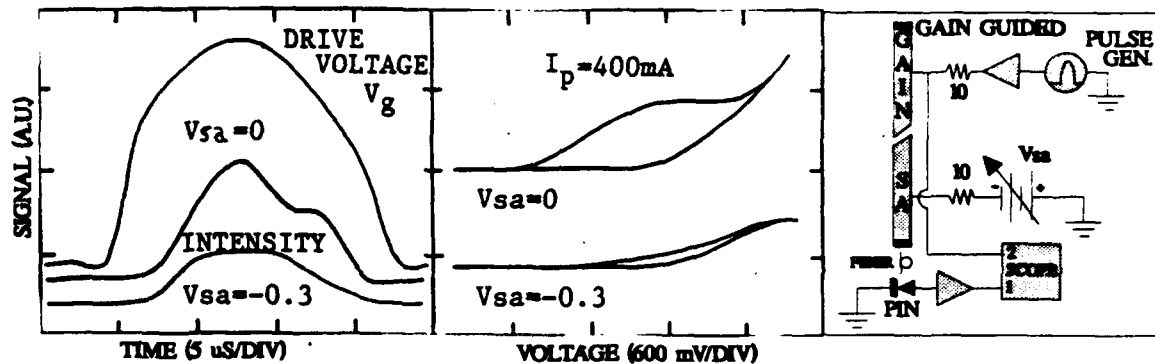


Figure 10.3: The left side shows plots of the timing relation between the drive voltage to the gain section of the gain-absorber pairs and the emitted irradiance from the pair; the irradiance is shown for two voltages on the saturable absorber. The middle panel shows the hysteresis loop for the emitted irradiance vs. drive voltage. The experimental setup is shown on the right.

The results for a typical device appear in figure 10.3. The vertical axis has arbitrary units in either voltage or irradiance. The left side of the plot shows the timing relation between the drive voltage to the gain section and the irradiance emitted through the saturable absorber. The hysteresis curves on the right hand side are plots of the irradiance vs. the drive voltage. The two intensity plots correspond to two different voltages applied to the saturable absorber. The slight asymmetry of the drive voltage results from the I-V and L-I characteristics of the laser diode as can be seen by comparing the drive voltage curve to the intensity curves.

Of particular interest is the hump on the right side of the $V_{sa}=0$ intensity plot. Once the saturable absorber is bleached, it remains in that state for values of current into the gain section which are less than

the initial threshold current. It is this hump which produces the upper hysteresis loop in figure 10.3. An increase of the reverse bias voltage causes the irradiance, the width and height of the loop to decrease. The loops can not be attributed to heating effects as the system would transverse the loop in a clockwise direction rather than the counter clockwise direction observed for these loops. No attempt was made to correct for RC effects present which probably dominated beyond about -0.6 volts; these effects can not explain the loops¹⁰ for saturable absorber voltages less than about -0.6 volts. The $V_{sa} = -1$ volt loop appears to be mostly a result of RC effects. We did note that the position of the single mode fiber strongly influenced the shape of the observed L-I curves. We attributed this behavior to the occurrence of bistability for only certain modes present in the multimode structure.

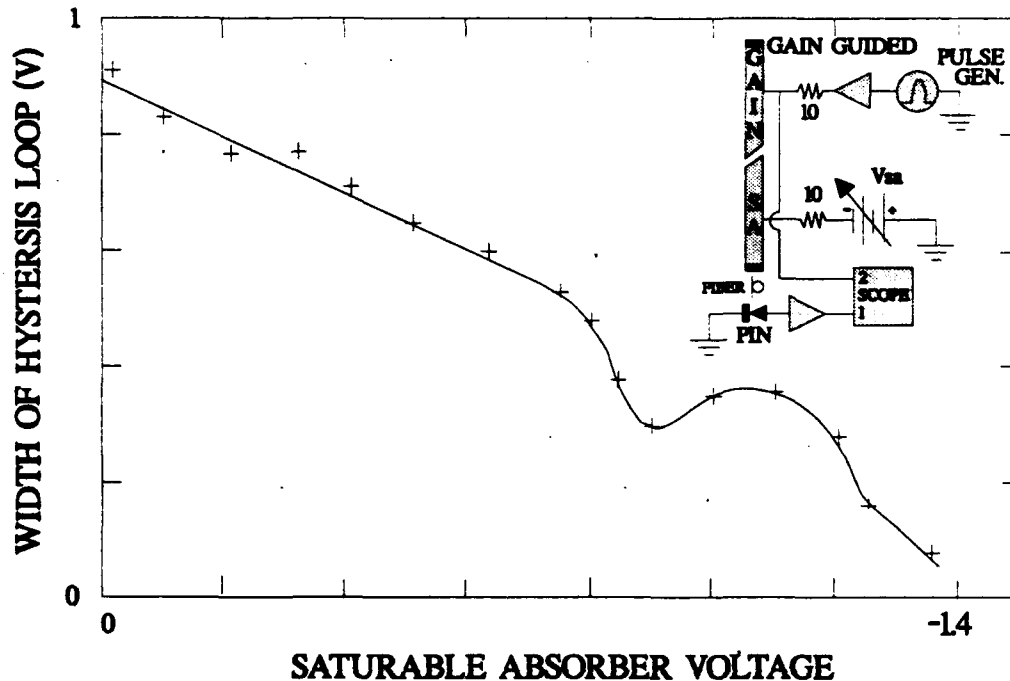


Figure 10.4: The width of the hysteresis loop as a function of the voltage applied to the saturable absorber. The effects of RC time delays have not been removed from the data which probably dominate the other effects in determining the width of the observed loops beyond about -0.6 volts. The inset shows the experimental setup used to observe the hysteresis loop.

The bistable characteristics were further investigated. The width of the loop was plotted as a function of the voltage applied to the saturable absorber as shown in figure 10.4. The width of the loop changed by an order of magnitude for a 1.4 volt change in the voltage applied to the saturable absorber. RC effects were probably responsible for the non-linear portion of the curve beyond about -0.6 volts.

D. DISCUSSION

Hysteresis in the L-I characteristics of the gain-absorber pair can be attributed to the characteristics of the saturable absorber. Below laser threshold, the saturable absorber presents a loss to the cavity which sets the threshold current at J_1 (for example). For currents just above J_1 , the photon density abruptly jumps to the upper branch of the hysteresis loop. Once the output state of the device corresponds to a point on the upper branch, the current can be decreased to values somewhat smaller than J_1 without significantly affecting the emitted flux because, on the upper branch, the saturable absorber is still bleached for currents near J_1 . At some current $J_2 < J_1$, the emitted flux will suddenly transition to the lower branch.

The hysteresis loops present in this paper are believed to be due to the mechanism described above. In this case, the voltage dependence of the loop width can be attributed to the quantum confined stark effect. The fact that the hysteresis was not observed for saturable absorbers with ridge waveguiding might be due to relatively low intensities necessary to saturate the absorption. The unguided saturable absorber sections would be less likely to mask the effect because the intensity of the light in the saturable absorber would be smaller due to diffraction effects. Another possibility consists of the self focusing of the light in the saturable absorber due to spatial hole burning.⁴⁸

E. SUMMARY

An optical RS flip-flop has been designed and presented for use as an optical memory element in an integrated optical processor. The design incorporated TIR mirrors, a main cavity with a gain section and a voltage controlled saturable absorber, a quench laser and a pump laser. Experiments tested for hysteresis in the L-I characteristics of ridge guided single and multimode waveguides with negative results. Hysteresis was found in gain-absorber pairs which had no waveguiding in the saturable absorber. The laser quenching was tested in logic gates with coupled cavities and TIR mirrors. The effect of the pump laser on the output state of the devices which exhibited hysteresis was not tested.

The final version of the optical RS flip-flop will employ a silicon diffusion process to delineate the waveguides and provide electrical isolation rather than the shallow etches presently used. The electrical isolation between the devices should increase to about 1 M Ω from the present value of 300 to 1000 Ω .

The poor electrical isolation makes it difficult at times to distinguish between the optical and electrical effects. The use of this silicon diffusion process should dramatically improve the situation. The hysteresis and quenching obtained from these new devices will be modeled and then simulated on a computer.

XI. MULTIQUANTUM WELL PHOTODETECTORS

Arrays of multiquantum well photodetectors with various areas for the active region were monolithically integrated with lasers, optical logic gates and optical memory elements. The detectors were tested for capacitance as a function of area, responsivity as a function of wavelength and linearity in light intensity.

A. INTRODUCTION

Electro-optic devices integrated onto AlGaAs-GaAs multiquantum well heterostructure used for digital signal processing applications generally require photodetectors to determine the output state of the devices. It is well known that photodetectors can be monolithically integrated with lasers and waveguides. The

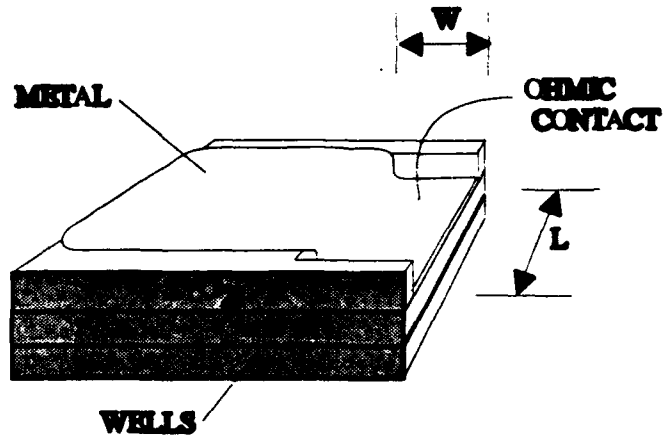


Figure 11.1: The multiquantum well photodetector. A square region of the SiO_2 is etched to the heterostructure for the Ohmic contact with the metallization.

main thrust of this project is to characterize the photodetectors which are monolithically integrated with other devices.

The characterization of the photodetectors for this chapter focuses on the scaling of capacitance and responsivity with the area of the active region of the photodetector. Figure 11.1 shows the structure of one of the photodetectors in the array. The five quantum well heterostructure has an SiO_2 layer which serves as a zinc diffusion mask and as electrical isolation. The SiO_2 is etched through to the heterostructure so that the metallization Ohmically contacts the active region of the photodetector. Light illuminates the detector on the right hand side. The photodetectors have active areas

$$\text{RECTANGULAR} \quad W L = 100 (75 + 25 n) \mu\text{M}^2 \quad \text{for } n = 0, \dots, 5 \quad (11.1a)$$

$$\text{SQUARE} \quad W L = (25 + 25 n)^2 \mu\text{M}^2 \quad \text{for } n = 0, \dots, 3 \quad (11.1b)$$

and the electrical contact pads have areas of about $22 \times 10^3 \mu\text{M}^2$.

The remainder of this chapter presents the fabrication process, the experiment and results of the test of capacitance and responsivity as a function of area, a discussion of the results and conclusions.

B. FABRICATION

The photodetectors were fabricated from Graded Index Separate Confinement Heterostructure (GRINSCH) GaAs-AlGaAs Multiple Quantum Well wafers as described in chapter 3. The detectors had CAIBE etched facets shown on the right side of the device in figure 11.1. An SiO_2 layer was used as electrical isolation as well as an etch retardation mask for a shallow etch process. For the shallow etch, the SiO_2 is etched through to the heterostructure so that the metallization Ohmically contacts the active region of the photodetector. Large metal pads were connected to the devices to supply the external reverse bias; the layer of SiO_2 , 1300 Angstroms thick, electrically isolated the pads from the GaAs. The top P^+ and bottom N^- Ohmic contacts were made as discussed in chapter 3. The detectors were epoxied to copper blocks with conductive epoxy after cleaving.

C. EXPERIMENTS

The capacitance as a function of area, reverse bias and frequency was determined for the photodetectors as discussed in subsection 1 below. The responsivity as a function of wavelength and the linearity was tested for one of the detectors.

C.1 Capacitance

The capacitance as a function of area, reverse bias and frequency was measured for the photodetectors using an HP 4061A Semiconductor Component Analyzer. The photodetectors were mounted in a test fixture and probed with Alessi

Micropositioning Probes. The capacitance between the probe and ground was determined to be about 100

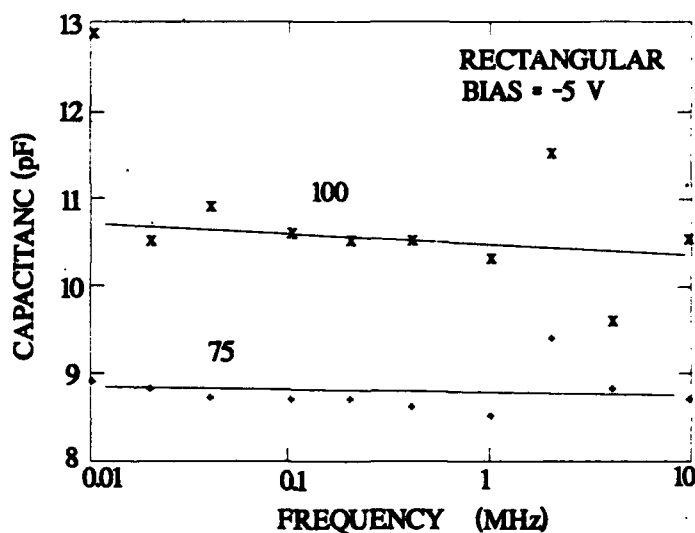


Figure 11.2: The frequency dependence of the capacitance of two of the rectangular style photodetectors with active areas of 75,000 and 100,000 μm^2 . The photodetectors were reversed biased at -5 volts.

fF and was negligible. Figure 11.2 shows the frequency dependence of the capacitance for two of the rectangular style photodetectors where were reversed biased at -5 volts. For the 75,000 and

100,000 μM^2 active areas, there is little frequency dependence over the range of 10 kHz to 10 MHz. Figure 11.3 shows the frequency dependence of the capacitance of the square style photodetectors with active areas of 50, 75, 150, 175, 200 $\text{k}\mu\text{M}^2$ and reversed biased at -5 volts. The three curves

which rise as the frequency decreases were on the same piece of heterostructure while all the others were on separate pieces. We believe that poor mounting between the photodetectors and the copper block might account for the low frequency rise. Figure 11.4 shows the voltage dependence of two rectangular photodetectors with active areas of 75 and 100 $\text{k}\mu\text{M}^2$; the frequency was fixed at 400 kHz.

The capacitances for reverse bias voltages are on the order of 10 pF. The curves show the expected

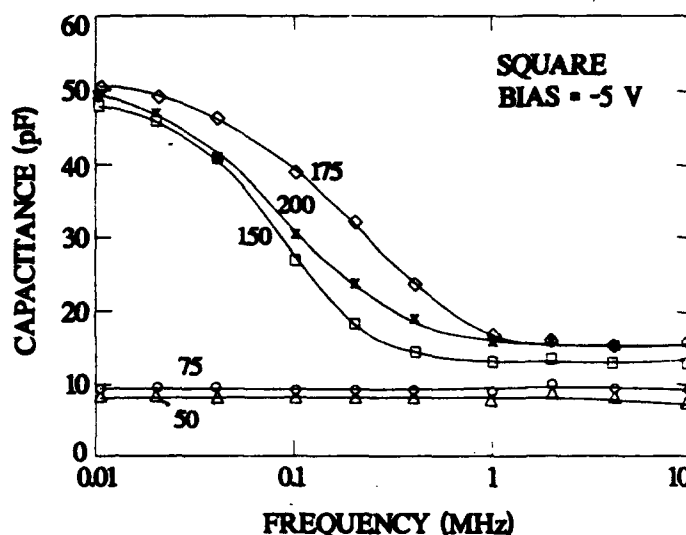


Figure 11.3: The frequency dependence of the capacitance of the square style photodetectors with active areas of 50, 75, 150, 175, 200 $\text{k}\mu\text{M}^2$. The photodetectors were reversed biased at -5 volts.

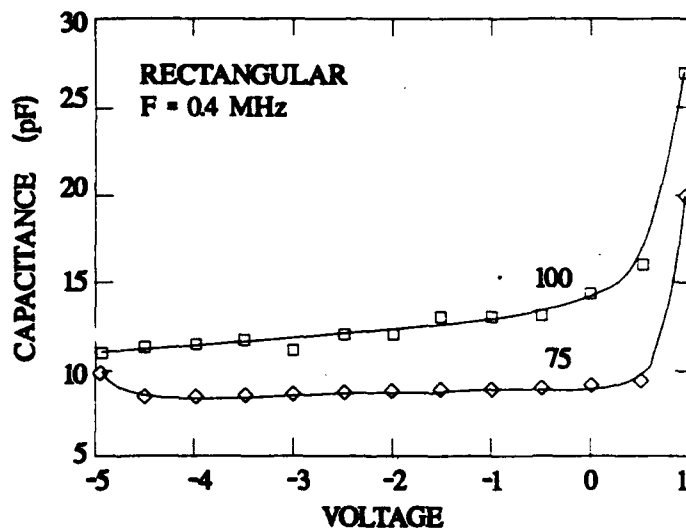


Figure 11.4: The voltage dependence of the capacitance of two of the rectangular style photodetectors with active areas of 75,000 and 100,000 μM^2 . The frequency was fixed at 0.4 MHz.

rise in capacitance for a forward biased diode. Figure 11.5 shows the voltage dependence of the capacitance of the square style photodetectors with active areas of 50, 75, 150, 175 and 200 $\text{k}\mu\text{M}^2$. The capacitance for reverse bias voltages was relatively flat and exhibited the typical rise for forward bias.

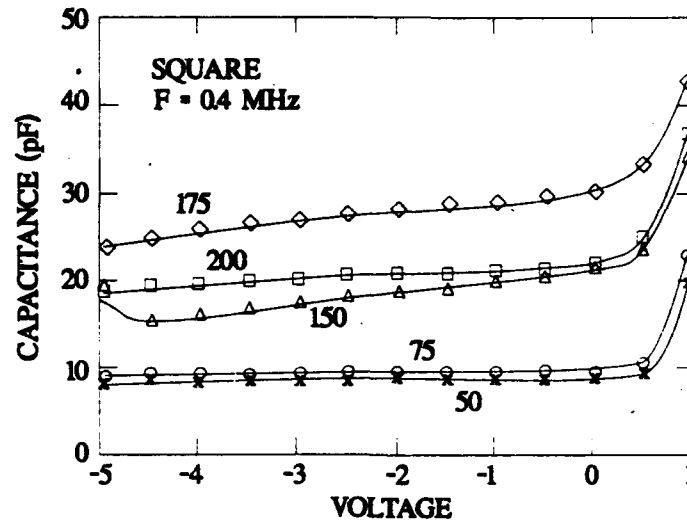


Figure 11.5: The voltage dependency of the capacitance of the square style photodetectors with active areas of 50, 75, 150, 175 and 200 $\text{k}\mu\text{M}^2$. The frequency was fixed at 400 kHz.

The flat portions of figures 11.2 to 11.5 yield capacitances which should scale with detector area.

Figure 11.6 shows the capacitance of the square style contacts plotted as a function of area. The top

and bottom lines represent the capacitances obtained

from the plots of capacitance versus voltage and frequency respectively. The point where the two lines intersect the capacitance axis represent the capacitance C_{pd} between the probe contact pad and ground.

For the photodetectors tested here, $C_{pd} = 7 \text{ pF}$.

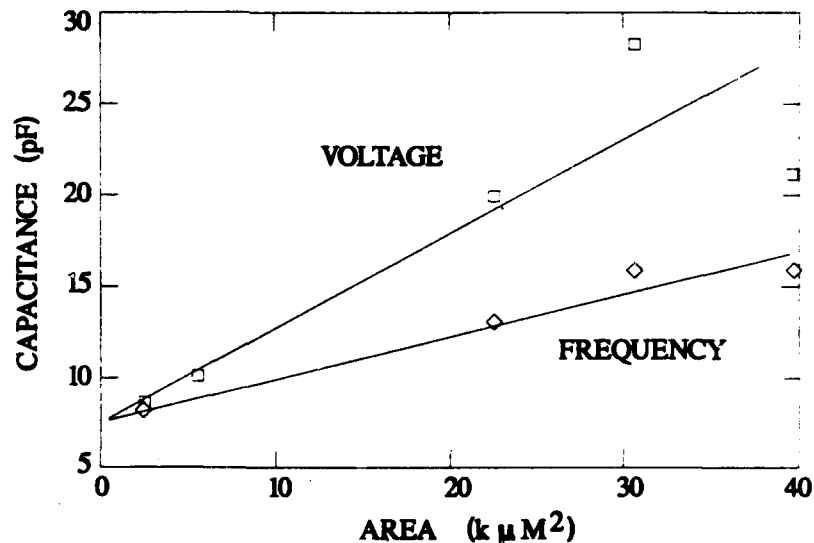


Figure 11.6: Plots of the capacitance of the square style photodetectors obtained from the flat portions of the voltage and frequency plots.

C.2 Responsivity

The linearity and responsivity were determined for a photodetector with an approximate active area of $100 \times 100 \mu\text{M}^2$. No attempt was made to calibrate the amount of light incident on the photodetector facet for these preliminary measurements. Both TE and TM modes from an argon pumped Ti-Sapphire laser system were used simultaneously. Figure 11.6 shows the results of the linearity test.

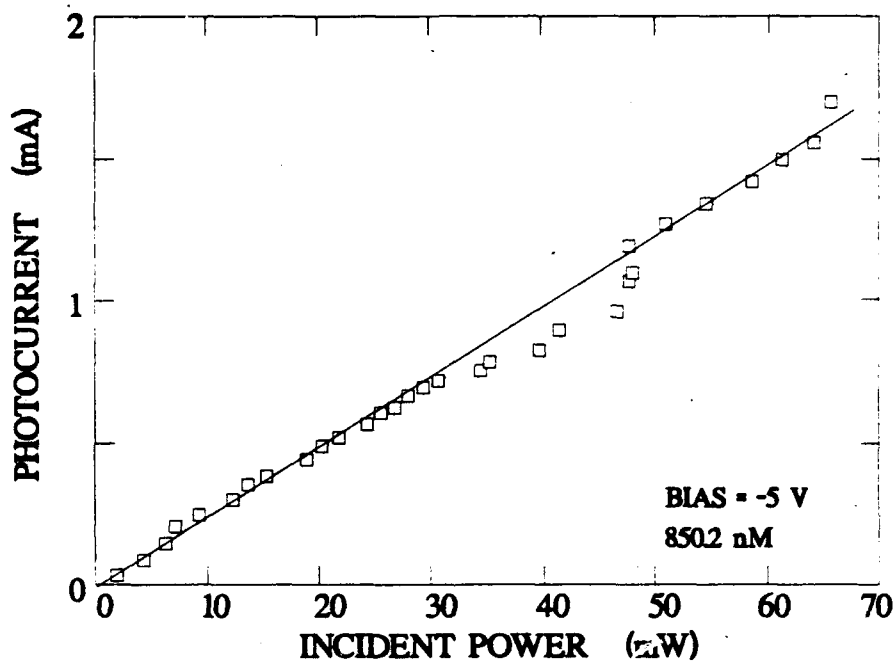


Figure 11.6: Plot of photocurrent versus total power in the incident beam (not the power incident on the photodetector facet). The bias was -5 volts and the wavelength of the incident illumination was 850.2 nM.

The small dip in the photocurrent current near 40 mW might be due to drift in the experimental apparatus.

Figure 11.7 shows the preliminary results for the responsivity as a function of wavelength. Once again the bias was set at -5 volts and no attempt was made to calculate the actual power incident on the photodetector facet.

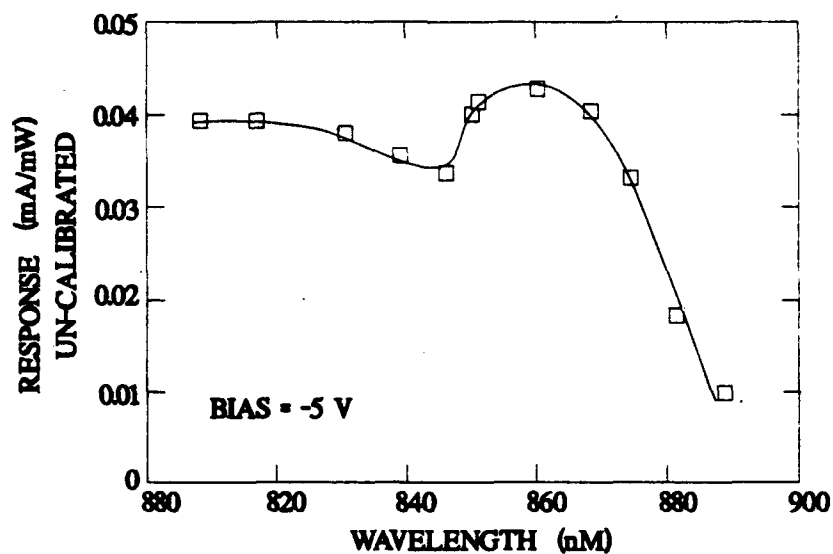


Figure 11.8: Plot of response vs wavelength. The power actually incident on the photodetector facet was not determined.

D. DISCUSSION AND CONCLUSIONS

Preliminary tests on the integrated photodetectors show that the devices are promising for use with optical logic gates and memory elements which use multiquantum well heterostructure lasers. With smaller probe contact pads, they can be made to have a relatively fast response time. The response tests will require more work especially to determine the amount of illumination incident on the facet. For the detectors to be useful, better methods of electrically isolating one device from the other must be employed. To this end, a lattice disordering process will be developed.

XII. AN ACOUSTO-OPTIC BISTABLE SWITCH

Presented are the results of an investigation into the behavior of a hybrid optical switch. The device is based on Bragg diffraction and utilizes an acousto-optic modulator with an electronic feedback system. It is analogous to an electronic Schmitt trigger circuit. Our primary interest in the device was its characteristics during transition between stable states. Transient behavior characteristics predicted by theory were verified. Stable, bistable and periodic behaviors were observed.

A. INTRODUCTION

Optical bistability has recently attracted much attention. Devices based on the phenomenon are of interest because they will lead to the development of optically operated switches, optical logic gates, amplifiers and memories. Photonic switching elements have very fast nonlinearities, in the picosecond range, and an inherent ability for parallelism, with throughput capabilities in terms of number of spatially resolvable spots. For these reasons, optical switches offer the possibility of manipulating optical information at high speeds and broad bandwidths. Another significant advantage is the ability to operate directly on a signal that is already in the form of light. Hence, optical switches will be key components for optical computing, optical signal processing and beam shaping. In terms of technology, problems may be approached optically that may not be solved otherwise.^{49,50}

The phenomenon is of theoretical interest as well, due to the existence of optical chaos, period-doubling bifurcations leading to chaos, for example. It is important that these regions of instability in parameter space be identified, as one may want to either avoid these regions and operate in a portion of the parameter space with well-behaved, stationary conditions or use the unstable regions for their self-oscillatory behavior as an optical clock generator for example.⁵¹

Not only can such a device be used as an optical switch or optical memory but it also offers a convenient means of verifying some of the existing theoretical knowledge regarding the optical switching phenomenon. In this investigation, stable, bistable and periodic behaviors were observed which verifies transient behavior characteristics predicted by theory.

The acousto-optic (AO) bistable device is based on the interaction of light and sound, the underlying mechanism being the diffraction of a light beam by an acoustic wave. The basic principle is shown in figure 12.1. The AO cell itself is driven with an RF signal. As electrical energy is converted into acoustic energy, an upward traveling pressure disturbance is created. This disturbance produces regions of compression and rarefaction within the crystalline material of the cell. This moving, periodic variation in density induces a moving periodic change in the dielectric properties of the material and in the index of refraction (the photoelastic effect). A light beam now incident on the cell will be scattered under interaction with the sound field traveling through the cell. In this way a traveling diffraction grating or *acoustic grating* is created.

The basic scheme behind the experimentation with the device is to enhance the nonlinearity of the transmitting medium with electronic feedback, as described below. The setup is shown in figure 12.2. The transducer of an AO cell is driven with a signal generator. The light source is a He-Ne laser. The device is operated in the Bragg regime. That is, the incident light with electric-field amplitude E_{inc} enters at a known angle Θ_B and is scattered predominantly into two beams -- a zeroth-order undiffracted beam with electric field amplitude E_0 and a first order diffracted beam with amplitude E_1 . A photodetector placed to receive the first order light converts its intensity to an electronic signal. The signal is then amplified by passing it through an amplifier of gain constant β_0 . The amplified signal is then fed back to the transducer in unison with an external bias voltage proportional to α_0 . This increases the strength of the modulating signal which, in turn, increases the intensity of the first order diffracted light thus forming a positive feedback loop. The resulting system is bistable. It has nonlinearity and feedback. We expect it to exhibit hysteresis in its input-output characteristics.

The remainder of this chapter is divided into 4 sections. The Principles of Operation section contains a summary of the diffraction model. The Experimental section describes the experimental apparatus, equipment characterization and results. The last two sections are the Discussion and Conclusion sections.

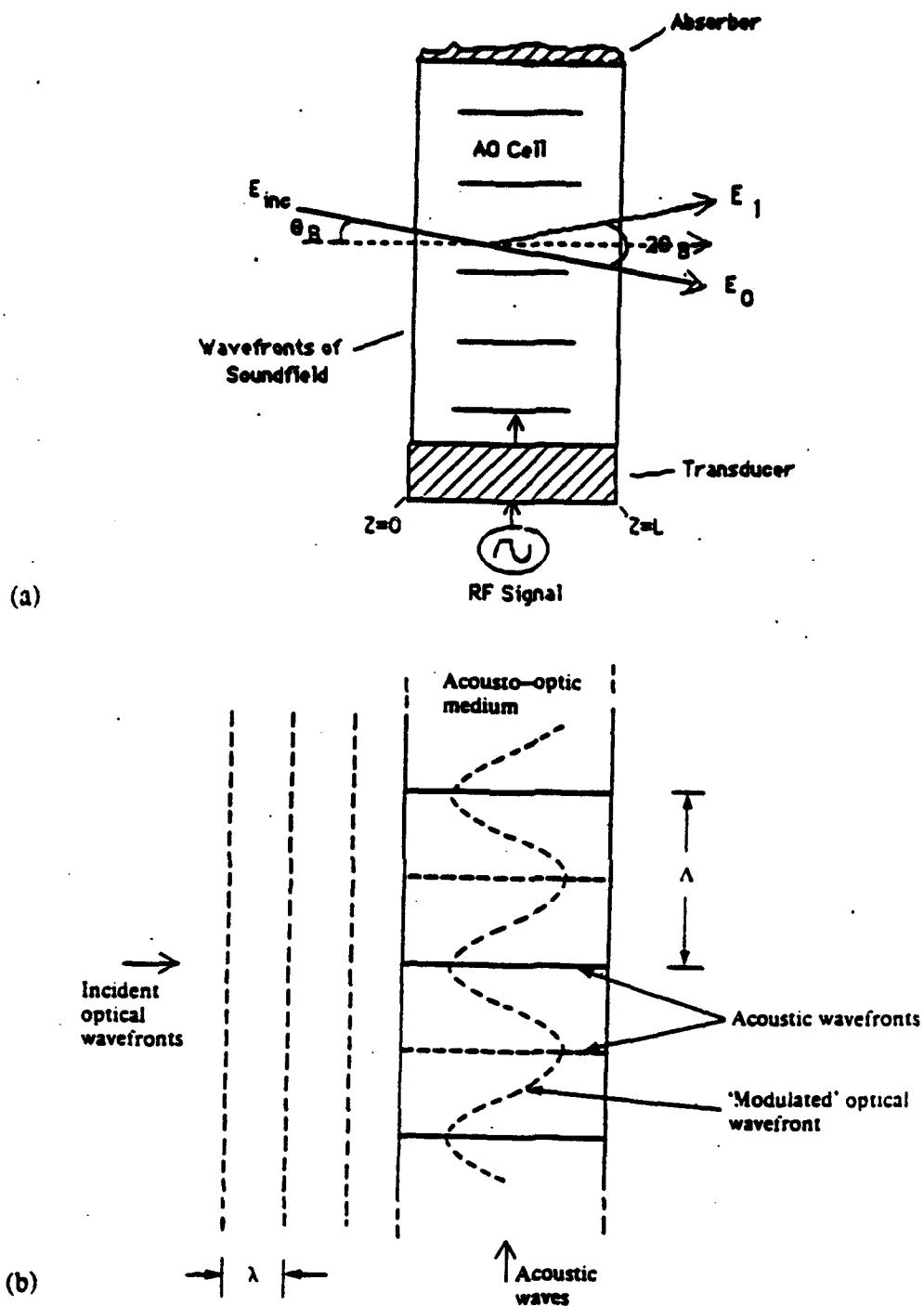


Fig 12.1 Basic Principles of AO Operation.

(a) The incident light beam E_{inc} is scattered under interaction with the sound field traveling through the cell (not drawn to scale). Constructive interference occurs for $\sin \theta_B = \lambda / 2 \Lambda$, where λ is the wavelength of light and Λ the wavelength of sound. (b) The acoustic wave changes the refractive index of the medium in a periodic way so that the plane optical wavefronts are phase modulated, taking on the "wavy" appearance shown (very much exaggerated) as they propagate through the medium.

AO SWITCH: PRINCIPLE OF OPERATION

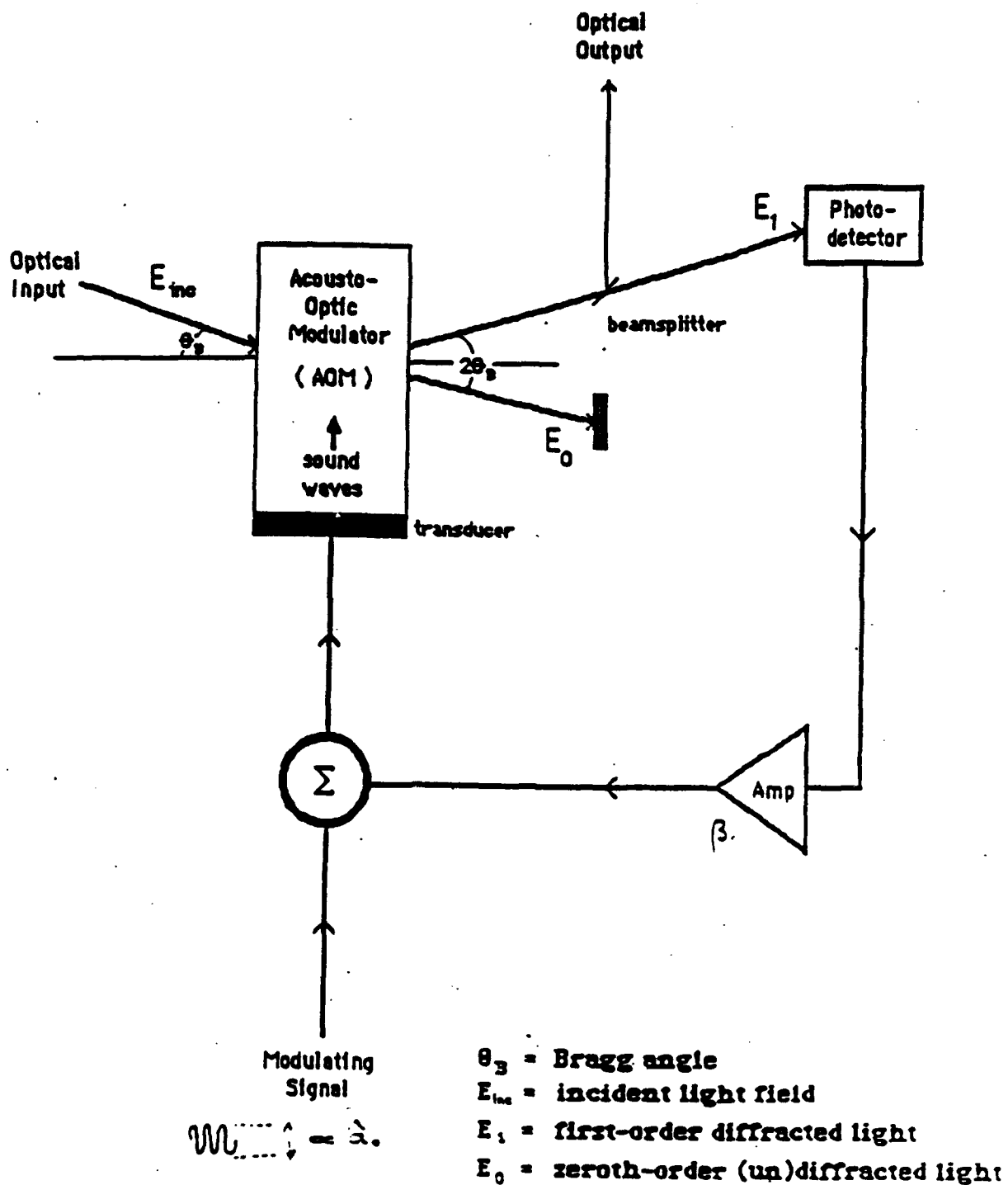


Fig 12.2 Basic Set-Up for Bistable Operation.

B. PHYSICAL PRINCIPLES OF OPERATION

Optical bistability refers to the existence of two stable states of an optical system for a given set of input conditions. Most bistable systems combine nonlinearity with feedback, for example, Fabry-Perot resonators. All exhibit abrupt switching and hysteresis.

The first step in the analysis of the optically bistable system is the calculation of the stationary solutions. One starts with a model that adequately describes the dynamics of the system. With the time variable taken to be very large, the stationary solutions are obtained. The stability against small perturbations is then checked.

In the system presented here, the dynamics involve coupling matter to radiation and are nonlinear. The system also has delayed feedback, which is added to enhance the nonlinearity of the interaction. The transient behavior of such a system is described by a nonlinear second order delay-differential equation.⁵² The equation incorporates the AO interaction in the Bragg regime, the feedback action and the various time delays in the feedback circuit.

In our modeling of the system, the differential equations were converted to difference equations rather than delay-difference equations. The model allows for a comparison of predictions and observations regarding the onset of instability.

Some approximations and assumptions have been made regarding the transducer width and the beam shape: the width of the transducer is finite and the beam is Gaussian. This means that other orders are observed even when in the ideal Bragg regime.

Following Korpel⁵³, and more completely summarized in a Rome Laboratory Technical Memorandum by Maurice and Parker (published in 1992), the time independent dynamics of the AO interaction process for the ideal Bragg regime case can be summarized by a set of coupled differential equations:

$$\frac{dE_1}{dw} = -i \frac{\alpha}{2} E_0 \quad (12.1a)$$

$$\frac{dE_0}{dw} = -i \frac{\alpha}{2} E_1 \quad (12.1b)$$

where $i = \sqrt{-1}$, $w = z/L$ is the normalized distance in the direction of light propagation through a cell of width L , $E_0(w)$ is the amplitude of the zeroth order undiffracted light field, E_1 is the amplitude of the first order diffracted light field, $\alpha = (k_v/2) L / C / S$ is the sound induced peak phase delay encountered by the light in the acousto optic interaction region and is proportional to the sound amplitude, C is a material constant, k_v is the light propagation constant in vacua, S is the plane wave sound amplitude, and L is the length of the interaction region (width of the AO cell).

The exit diffracted light field has amplitude E_1 , obtained by solving equation 12.1a and 12.1b subject to the initial conditions

$$E_0 = E_{inc} \text{ and } E_1(0) = 0$$

where $w = 0$ is $z = 0$ and $w = 1$ at $z = L$ as shown in figure 12.1.

The solution for the exit diffracted light in terms of intensity is

$$I_{E_1}/2 = I_{E_{inc}}/2 \sin^2\left(\frac{\alpha_0 + \beta I_{E_1}/2}{2}\right) \quad (12.2a)$$

and from energy conservation

$$I_{E_1}/2 + I_E/2 = I_{E_{inc}}/2 \quad (12.2b)$$

where the effective α is given by

$$\alpha = \frac{\alpha_0 + \beta I_{E_1}/2}{2} \quad (12.c)$$

α_0 is proportional to the external bias shown in figure 12.2 and β , the gain coefficient, denotes the product of the gain constant β_0 and the efficiencies of the photodetector and other equipment.

Note that under feedback action, α can no longer be treated as a constant. However, it is acceptable to do so during an interaction time, because the interaction time interval, equal to the laser beam width divided by the speed of sound in the crystal medium (about 0.5 μs), is much smaller than the response time of the photodetector and other delays in the feedback path (on the order of tens of microseconds). In effect, we assume that the sound pressure remains constant during an interaction time.

Equations 12.2 describe the system shown in figure 12.2. Three parameters are involved $/E_{inc}^2$, α_0 , and β . Depending upon which is varied, three modes of operation are possible, each leading to bistable operation:^{52,54}

- (i) change in the input light intensity $/E_{inc}^2$
- (ii) change in the modulator bias voltage α_0 , and
- (iii) change in the gain of the feedback loop β .

The transient response of the system is studied by varying on of the parameters above. In this experiment, the modulator bias voltage α_0 was varied, which was equivalent to varying the input sound intensity. This involved a minor change in the figure 12.2 operation that incorporates incremental α_0 . Figure 12.3 shows the modified operation for variable bias voltage in the feedback loop. The magnitude of α_0 is our input. For a given $/E_{inc}^2$ and β , α_0 is to be plotted against $/E_1^2$.

The equations are approximated by recursion relations.

$$/E_1(n+1)^2 = /E_{inc}^2 \sin^2\left(\frac{\alpha_0 + \beta/E_1(n)^2}{2}\right) \quad (12.3)$$

Under feedback action, E_1 will undergo a series of iterations corresponding to each updated value of α . Note that in the steady state (n approaches infinity), equation 12.2a is recovered from 12.3.

A similar expression can be written for trips down the hysteresis loop⁵⁵ as shown in figure 12.4. The points along the midsection, between turning points C and D, where the S-shaped curve, equation 12.2a, folds upon itself, are unstable and unphysical. The resultant curve is a hysteresis loop as shown, consisting of two stable branches, A-B-C and D-E-F, with movement occurring along either the upper or lower branch in a counter clockwise direction.⁵⁶

The onset of hysteresis can be predicted. As indicated in figure 12.4, the onset of hysteresis corresponds to the turning points C and D of the S-shaped function which assumes infinite gradients. To predict where in parameter space these points are, one determines where in parameter space the curve assumes infinite gradients. The derivative of $/E_1^2$ with respect to α_0 defines the critical relationship between the parameters of the space. Setting the reciprocal of this derivative to zero yields the necessary expression. The results show that for $\beta > \beta_c = 2$, the system exhibits bistable behavior.

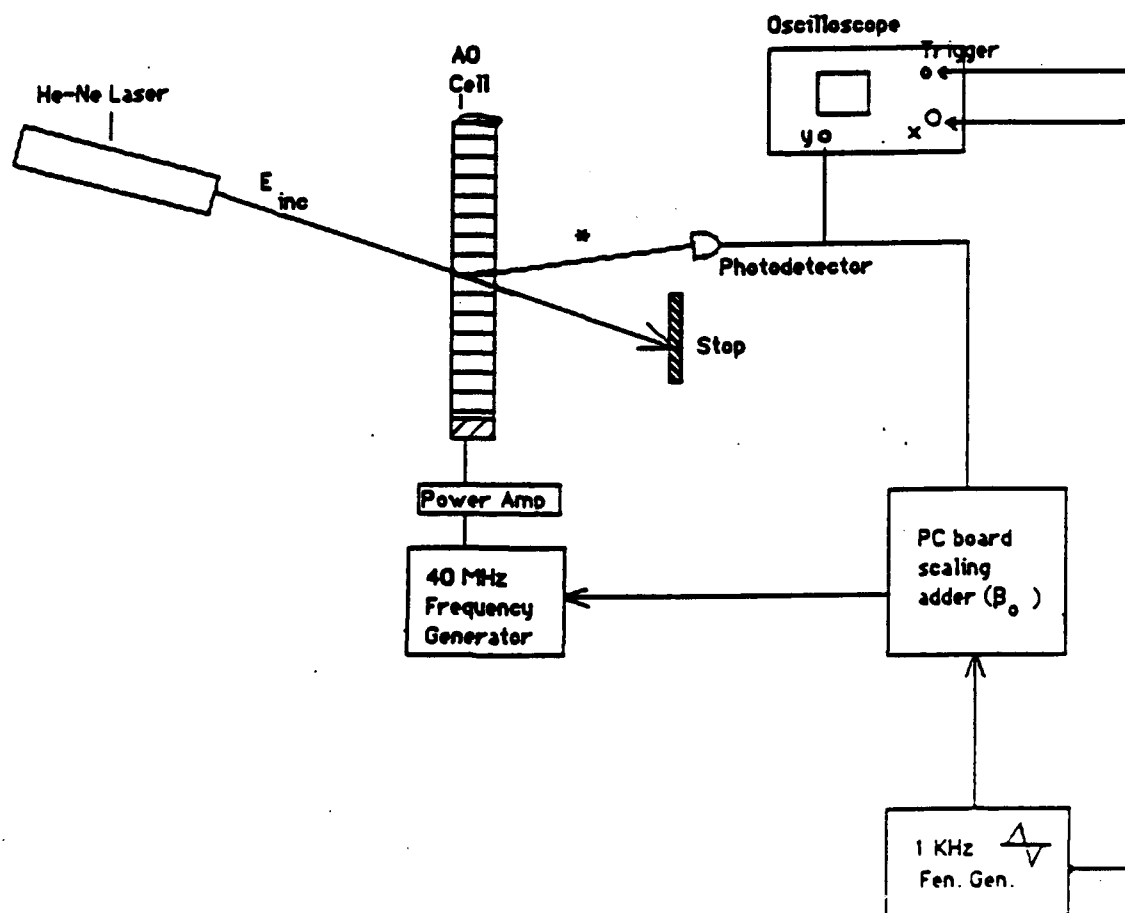


Fig 12.3 Experimental Set-Up (Modified Set-Up for Incremental α).

* It was necessary to insert a 0.5 neutral density filter here.

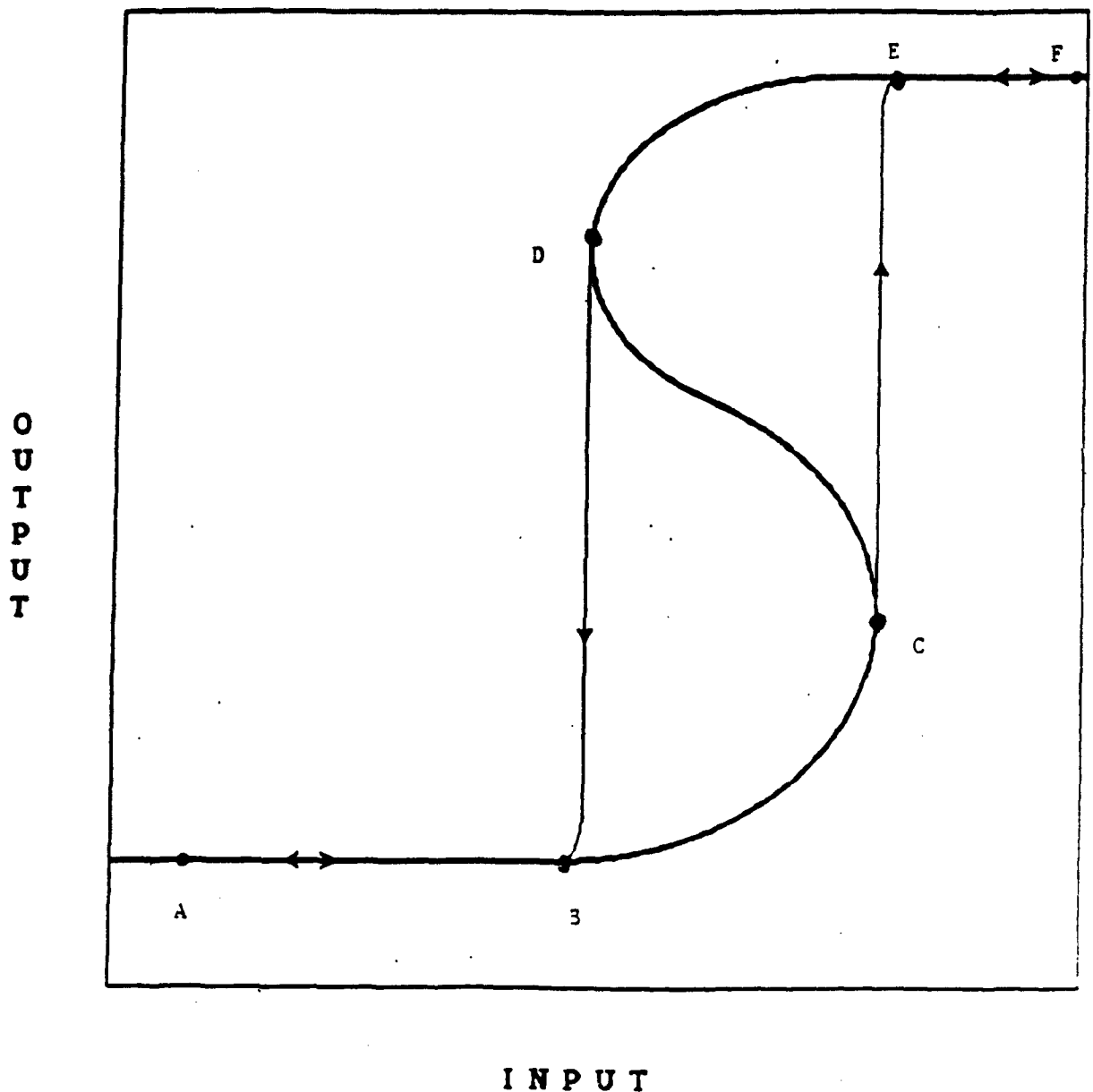


Fig 12.4 Illustration of Hysteresis Loop.
The illustration is qualitative only. The segment of curve between points C and D represents instability and is physically unattainable.

The dynamic properties of the system can be obtained from equation 12.3. By expanding the sine-squared term, truncating and regrouping the first and second order terms, equation 12.3 can be recast into the standard form:^{57,58}

$$Y_{n+1} = (a - b Y_n) Y_n \quad (12.4)$$

where $Y_n = |E_1(n)|^2$, a and b are polynomials in the variables α_0 and β and E_{inc} has been normalized to unity. This is a logistic difference equation. In the limit of b approaching 0, for $a > 1$, it describes a purely exponential growth. For b different from zero, however, the quadratic nonlinearity produces a *humped* growth curve much like sine-squared along an interval (such as $[0, \pi]$), the slope of which corresponds to the severity of the nonlinearity and is tuned by the parameter a .

By defining $X = bY/a$, equation 12.4 can be written in its canonical form

$$X_{n+1} = a X_n (1 - X_n) \quad (12.5)$$

It is convenient to depict this graphically as shown in figure 12.5, where, for particular a and the equilibrium constraint $X_{n+1} = X_n$, two points of intersection exist corresponding to the existence of two fixed points in the behavior of the functional iterates of equation 12.5. Fixed points are possible constant, equilibrium values to which the sequence of iterates converges as in figure 12.6. A fixed point may be stable (damped oscillations when disturbed from equilibrium) or unstable (growing oscillations). Stability of the fixed point depends on the slope of the function at the point, the test being that the absolute value of the slope at the fixed point must be less than one.

The generating function for the iterates of the quadratic map in equation 12.5 have complex analytic properties.^{57,58} In this form, however, it is seen that the nonlinear function $F(x) = ax(1-x)$ attains a maximum value of $a/4$ at $x = 0.5$ and therefore possesses nontrivial behavior only if $a < 4$. Furthermore, all trajectories are attracted to $x = 0$ if $a < 1$. Thus, nontrivial dynamic behavior is predicted for $1 < a < 4$ only.

Now the two fixed points are $x^* = 0$, which is unstable, and $x^* = 1 - 1/a$, which is stable for $1 < a < 3$. For $a = 3$, both fixed points are unstable, while for $3 < a < 4$, no attracting (stable) fixed points exist. Thus,

stable dynamic behavior is predicted for 1 < a < 3.

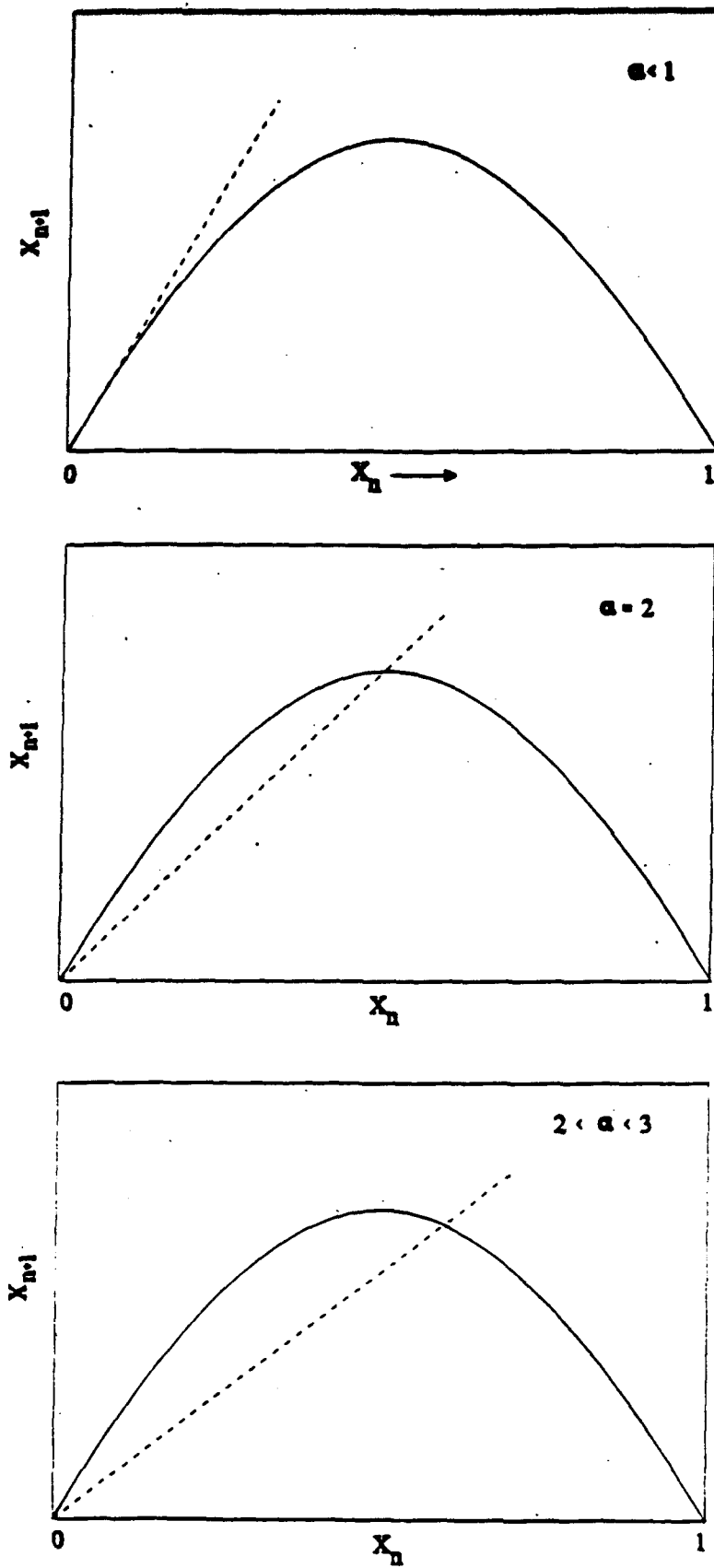


Fig 12.5 Typical Form of the Relationship between X_{n+1} and X_n .

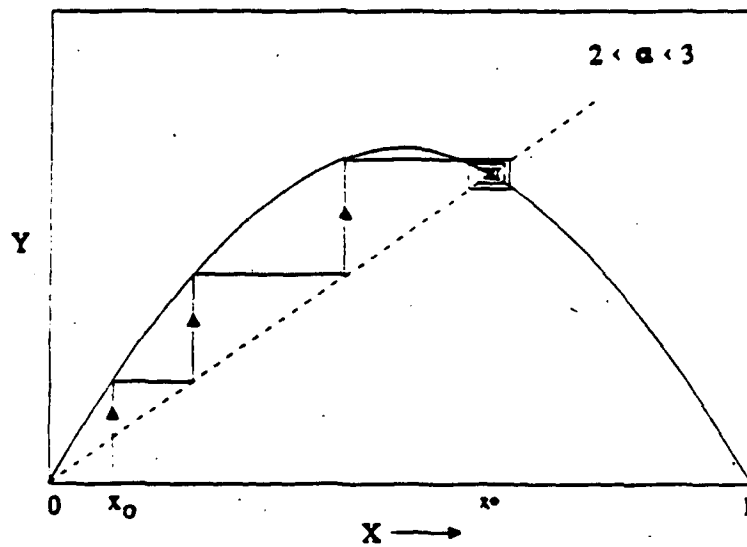
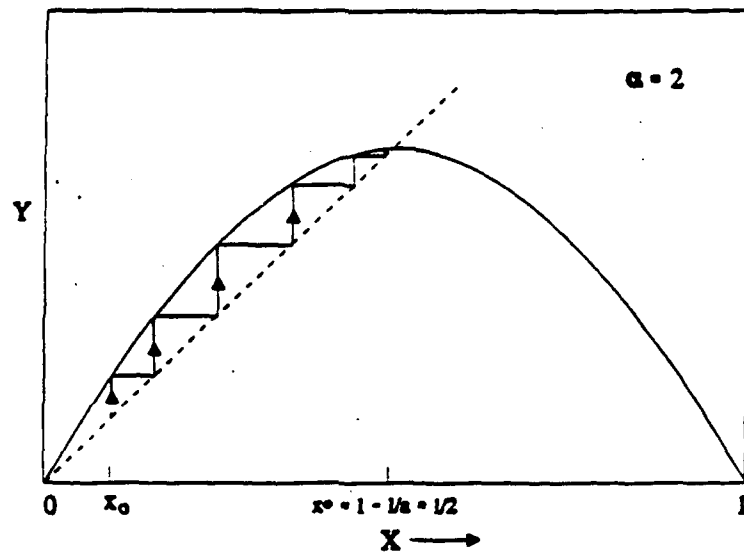
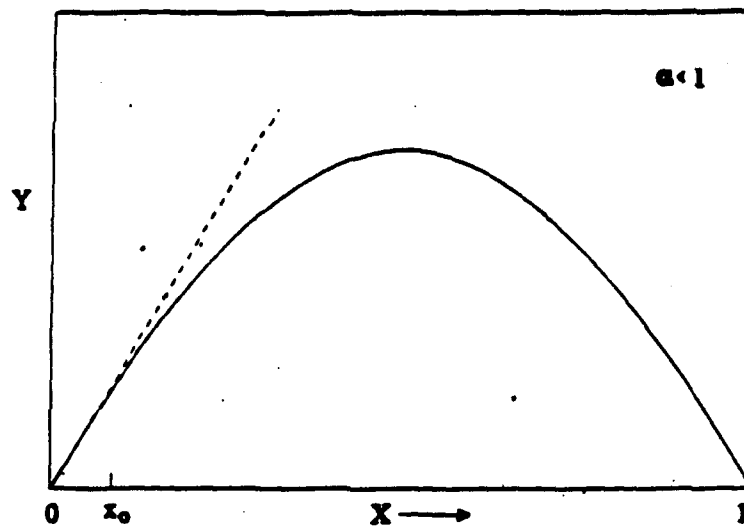


Fig 12.6 Illustration of the Iterates of x_0 .

As the relevant parameters are tuned and the function $F(x)$ becomes more steeply humped, the fixed point $x^* = 1 - 1/a$ becomes unstable ($a=3$). Slightly beyond the point in parameter space where this occurs ($a>3$), two new initially stable fixed points are born. Tuning the hump more steeply yet, each of these two points will, in turn, become unstable and bifurcate, giving rise to two more new and initially stable fixed points, etc. With increasing nonlinearity, an infinite number of fixed points with different periodicity's and an infinite number of different periodic cycles are possible. The regime becomes chaotic.⁵⁷

C. EXPERIMENTAL

The experimental setup is shown in figure 12.7 which is essentially figure 12.3 with the various gains and other parameters now labeled. Let I_0 , I_1 and I_2 represent optical powers in mW. I_0 is proportional to $/E_{inc}^2$ and I_1 to $/E_1^2$. The I_0 beam (approximately 6.34 mW at 632 nm) is incident upon the AO cell at approximately the Bragg angle and exits in two beams separated by twice the Bragg angle. As before, we are interested in the first order diffracted beam I_1 . A 0.51 neutral density filter ND reduces I_1 according to $I_2 = I_1 10^{-0.51}$. I_2 is detected by a silicon photodiode circuit with transfer function g_p and converted to the voltage V_1 . The RC combination that follows forms a high pass filter with 160 Hz cutoff frequency to reduce the influence of background illumination. The signal V_1 then enters a scaling-summer circuit consisting of two amplifiers with variable gain and a resistor-based adder (R_1, R_2, R_3) as shown in figure 12.8. The amplifiers are 741 op amps in standard amplifier configurations; D1 and D2, their corresponding variable resistors. The signal is scaled both before and after the summer with scaling factors G_1 and g_2 , respectively, converting it first to V_2 and then to V_4 . The output V_3 is obtained from signal generator voltage V_s and V_2 according to the relation $V_3 = g_{\Sigma s} + g_{\Sigma 2}$. The output V_4 then modulates a Fluke 6060B RF generator. Finally, the signal is amplified at the power amplifier by a factor of 100, and the resultant V_{rf} is sent to the AO cell, which operates at a 40 MHz center frequency. A complete diagram of both photodiode and scaling-summer circuits appears in figure 12.8

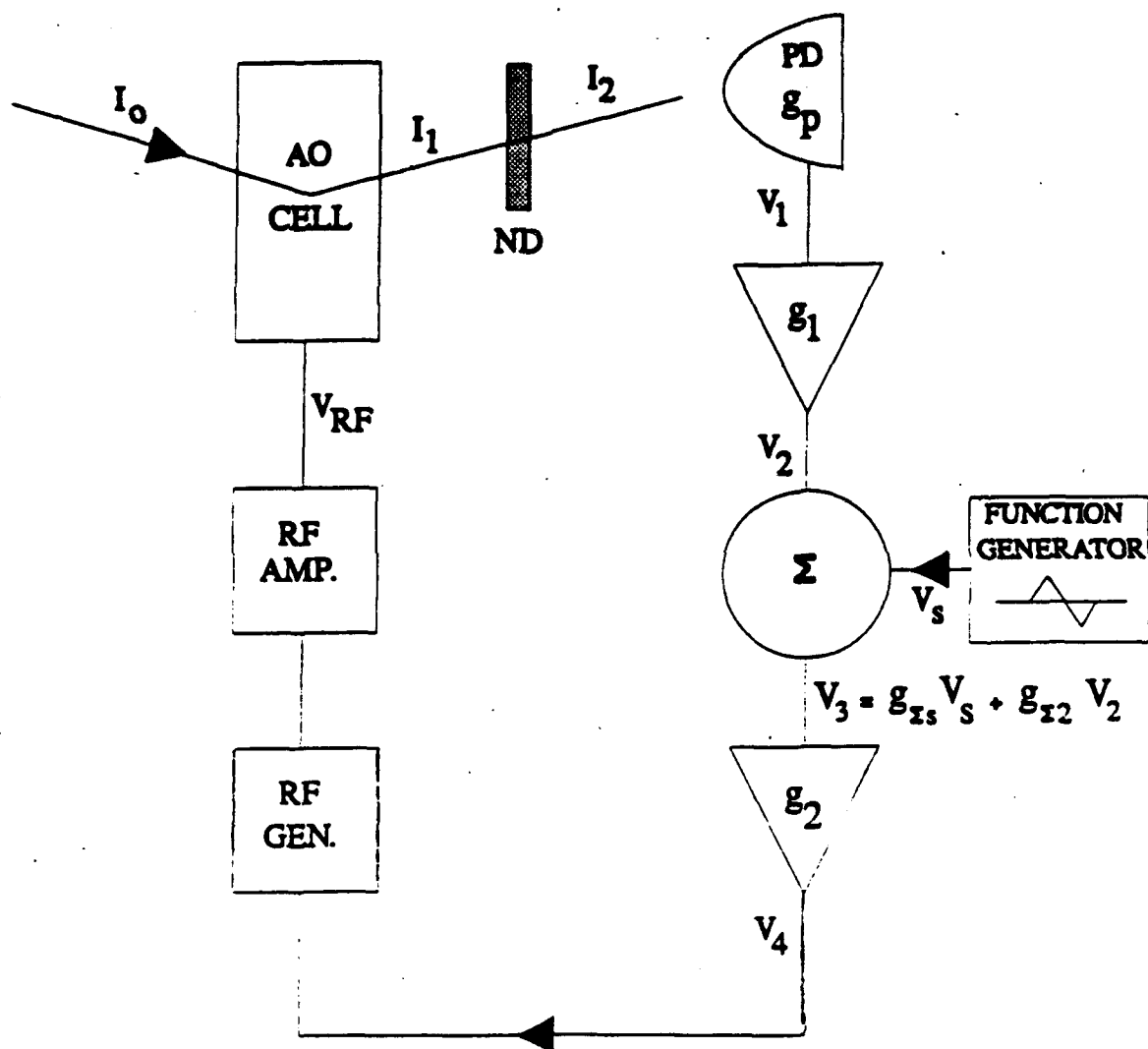


Fig 12.7 Experiment with Parameters Labelled.

Now in order to observe the hysteresis loop, the 40 MHz signal was amplitude modulated with a 1 kHz triangular waveform with peak to peak voltage of approximately 4.4 volts. This forms the envelope of the 40 MHz carrier frequency.

All instruments were characterized. These included the Si photodiode circuit, RF generator, function generator, power amplifier and AO cell. Also, the scaling-summer circuit that constitutes β_0 was characterized and all equation verified. Figure 12.10 shows the linearity test for the pin diode circuit. The gain and linear region of the RF generator and power amplifier were identified. These were never operated in a nonlinear regime. The regime of operation was also carefully chosen to ensure that operation of the cell remained along the near-linear, ramping-up portion of the cell's sine-squared characteristic. That is, for $I_1 = I_0 \sin^2(kV_{rf})$, where the argument kV_{rf} is the experimental equivalent to the α/s argument for some constant k , operation of the RF generator / power amplifier pair was chosen so as to produce an argument kV_{rf} confined to the midsection of the interval $(0, \pi/2)$.

We then varied β , first increasing it and then decreasing it, observing the transitions to bistability for various values of β . The value of β was varied by varying g_1 , above. The results appear in figure 12.10. We mention that, before observing anything, an RC high pass filter was necessary between the photodetector and scaling amplifier circuits, in order to block steady state currents and noise from the detector. Otherwise, the feedback signal was obscured and the useful gain of the scaling amplifier hindered.

The system is described by the set of equations:

$$\begin{aligned}
 I_2 &= I_1 10^{-0.51} \\
 V_1 &= g_p I_2 \\
 V_2 &= g_1 V_1 \\
 V_3 &= g_{\Sigma 2} V_2 + g_{\Sigma s} V_s \\
 V_4 &= g_2 V_3 \\
 V_{rf} &= V_0 [1 + (mV_4/V_{100})] \\
 I_1 &= I_0 \sin^2(kV_{rf})
 \end{aligned} \tag{12.6}$$

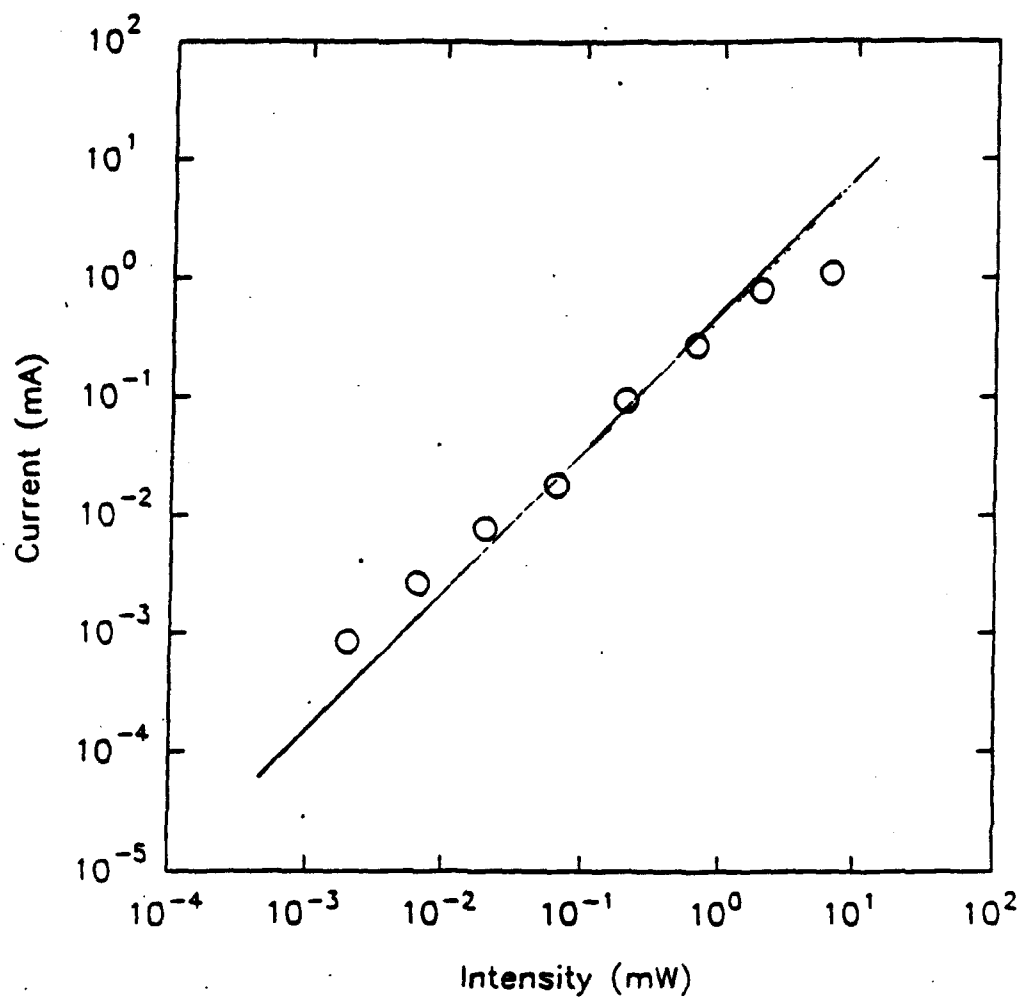


Fig 12.9 Linearity of the p-i-n Diode.

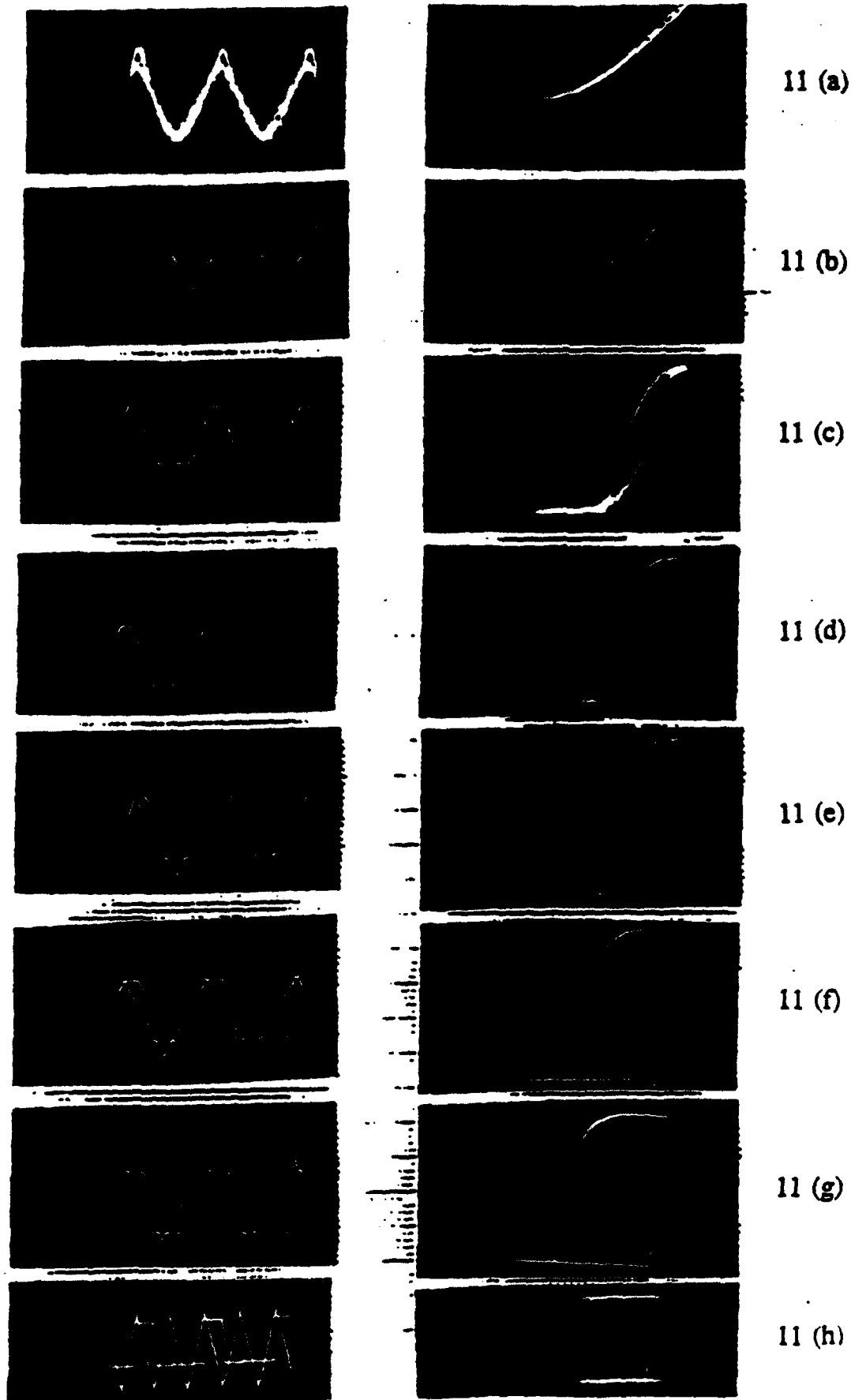


Fig 12.10 Photographs of Behavior: Minimum β to Maximum β . The photographs on the left show input (α_s) vs. time and output (E_s/β^3) vs. time on the same oscilloscope trace. The photographs on the right show corresponding input vs. output plots. Behavior under the minimum allowable gain, $\beta = 1.3$, is shown in 11(a), and here the output follows the input closely. In 11(b), the first bistable behavior occurs for $\beta = 2.8$. 11(c) - 11(f) show behaviors as β is further increased. Maximum bistable behavior is shown in 11(g), corresponding to $\beta = 5.8$. The first stable region beyond this is shown in 11(h) where $\beta = 6.2$.

where k is a parameter associated with the AO cell and m , V_{rf} , V_0 , and V_{100} are variable associated with the fluke RF generator / power amplifier pair defined as follows. The variable m is the modulation level on the Fluke, adjustable between zero and one. For minimum distortion, $m=0.21$ was chosen. The voltage V_{rf} is the voltage along the envelope portion of the RF signal. V_0 is determined according to the relation $V_0 = 100(AMPL/0.707)$, where the factor of 100 arises from the power amplifier and AMPL refers to a specific voltage control setting on the Fluke. Given the choice $m = 0.21$, it was found that $AMPL = 23$ mV was optimum. Thus, V_0 evaluates to 3.2V. V_{100} is the peak value of the input voltage V_4 which produces $V' = 0$ for V' the voltage level depicted below.

For the equipment used in this experiment, $V_{100} = 2.2$ V, as it is half the maximum peak-to-peak voltage of the triangular envelope wave. Finally, the constant k was found by noting a voltage V_{ao} such that $\sin^2(kV_{ao}) = 1$. For operation of the particular AO cell, it was determined that $k = 2.2$ V⁻¹.

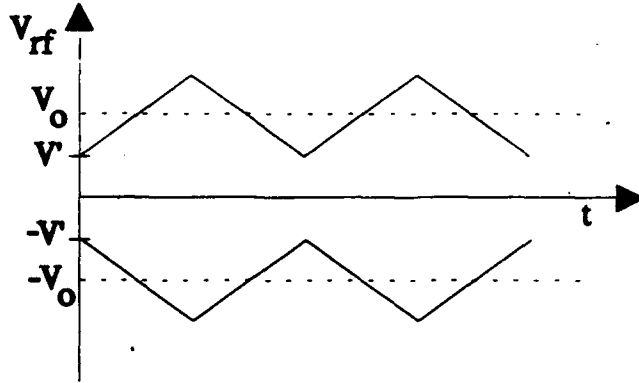


Figure 12.11: Definitions for voltages

Equations 12.6 can be combined to give:

$$V_{rf} = \frac{V_0}{V_{100}} (1 + m g_2 g_{\Sigma s} V_s + m g_p g_1 g_2 g_{\Sigma s} 10^{-0.51} I_1) \quad (12.6a)$$

where from 12.5

$$I_1 = I_0 \sin^2(kV_{rf}). \quad (12.6b)$$

Comparing equations 12.6 with equation 12.2a yields

$$\beta = 2 k \frac{V_0}{V_{100}} m g_p g_1 g_2 g_{\Sigma s} 10^{-0.51} \quad (12.7)$$

We solve for the remaining gain factors and substitute the results into 12.7. To obtain a value for g_p , we consider the current I induced in the pin diode:

$$I = \frac{I_2 e n \lambda}{hc}$$

where e is the elementary charge, $n = 0.76$ is the quantum efficiency for Si at 632 nm, h is Planck's constant, and c is the speed of light in vacuum. The evaluated transfer function g_p from equation 12.6 and figure 12.8 ($R = 5.1$ K Ohms) is then:

$$g_p = \frac{V_1}{I_2} = \frac{I R}{I_2} = \frac{enR}{hc} = 2.0 \text{ V/mW} \quad (12.8)$$

This agrees very well with experiment, as the linearity test on the pin diode, figure 12.9, also yields a transfer function equal to 2 V/mW. Next, referring to figure 12.8, the values of g_1 and g_2 at the observed onset of bistability are:

$$g_1 = 2.21 \quad \text{and} \quad g_2 = 3.13 \quad (12.9a)$$

Finally, the adder with values shown in figure 12.6 yields

$$g_{\Sigma 2} = g_{\Sigma s} = 0.5 \quad (12.9b)$$

Expression 12.7 can now be evaluated for β_c . Recalling $V_0 = 3.2$ and $V_{100} = 2.2$, and incorporating the values from equations 12.8, 12.9 into 12.7 yields $\beta_c = 2.8 \text{ mW}^{-1}$. This agrees favorably with the theoretically predicted value of $\beta_c = 2 \text{ mW}^{-1}$. Poon and Cheung⁵⁸ report an experimental value $\beta_c = 2.52$ for a similar setup.

With an increase in β beyond the critical value of $\beta_c = 2.8$, the system becomes bistable and exhibits hysteresis. Samples of this behavior for various values of β are shown in figure 12.10 and the following remarks refer to photographs featured there.

The photographs in figure 12.10 show oscilloscope traces of electrical input α_0 and optical output $/E_1/2$ versus time on the left and the corresponding input α_0 versus output $/E_1/2$ curves (I-O curves) on the right. Figure 12.10a has the minimum allowable β for our system ($\beta=1.3$). The optical output signal from the cell closely follows the input, and the I-O curve is almost linear. The time delay due to feedback, which is approximately 20 μ s for our system, gives rise to a phase delay between the two signals. This is evident in the slight Lissajous figure shown on the right in figure 12.10a, its width corresponding to the delay. Next, in figure 12.10b, β has been increased to a value of 2.8. The output signal begins to bend and saturate. It clips and shifts with respect to the input signal, and the previously smooth I-O curve

acquires a slight S shape. The area under the curve widens beyond the slight width of the Lissajous figure. As mentioned above, this marks the onset of bistability, the observed threshold being β_c . With increased β beyond β_c , the system becomes bistable and exhibits hysteresis. Sample hysteresis curves are shown in figures 12.10c-g. The area under the hysteresis curve increases with increasing β . It was also observed that there is a value of β beyond which bistable behavior ceases. For the setup presented here, this value is $\beta = 5.8$. With a small increase in β beyond this, however, another interesting phenomenon occurs: the output signal undergoes a discrete period change. That is, the output signal with a previous 1 kHz oscillation began to oscillate at 0.5 kHz. This is shown in figure 12.10h, where $\beta = 6.2$. As β was allowed to increase, many such thresholds were crossed and higher order periods of oscillation were observed. Other researchers have also observed similar oscillations.^{51,52,58,59}

In summary, the results show that while the input versus output curve looks roughly linear for low values of β , it tends to curve and saturate for values of β greater than β_c . We found a regime of stable, linear operation exists for $1.3 < \beta < 2.8$, a regime of bistability for $2.8 < \beta < 6.2$, and a series of higher order oscillatory regimes for $6.2 < \beta$. There appears to be a region $5.8 < \beta < 6.2$ for which there are no observable oscillations.

D. DISCUSSION

The experimental transients described above compare well with those predicted by equation 12.5. In particular, the observed critical value, $\beta_c = 2.8 \text{ mW}^{-1}$, is well within experimental error of the predicted value $\beta_c = 2 \text{ mW}^{-1}$. Bistable and higher order oscillatory regimes were identified and discussed above. The appearance of frequency locked phenomena such as bifurcations is an interesting result that may be used for an optical clock. Our experimental findings, in general, are in good agreement with predicted behaviors and behaviors investigated by other researchers.

We point out that certain inexact factors are incorporated in the experimental formula for β_c , equation 12.7. Perhaps most noteworthy are values of the parameters k , V_0 and that of the attenuation factor due to the neutral density filter, $10^{-0.51}$. First, the value of k may be in error as it was difficult to determine. The parameter k was determined by observing saturation in operation of the AO cell at $\sin^2(kV_{ao})=1$, or

$kV_{ao} = \pi/2$. We could only observe a saturation point, however, by increasing slightly beyond it. That is, the voltage V_{ao} was increased till saturation was observed, which means a V_{ao} slightly greater than ideally desired. In this way, our measure of V_{ao} might be in error, and, because it is linked to k , k might be in error as well. Second, there is the voltage V_o which incorporates the gain of the power amplifier with fluctuations of 10%. Lastly, there is the exponential associated with the neutral density filter -- a factor extremely sensitive to positioning, with differences on the order of a db occurring regularly with use of a filter holder.

E. SUMMARY

In this memorandum, the theoretical and experimental research in the area of optical bistability has been reported. The dynamics of an acousto-optic device based on Bragg diffraction were investigated. The device was modeled as a nonlinear system with delayed feedback. The model predicted bistability. Bistable systems of this type are characterized by the existence of multiple critical points which mark transitions between stable states. In our system, stable, bistable and periodic behaviors were observed, in agreement with predicted behaviors, and the observed threshold marking the onset of instability compared well with that predicted by theory. Due to a large parameter space, however, the behaviors were difficult to obtain and analyze. It was necessary to eliminate fluctuations due to noise. It was found that this can dramatically alter the dynamics of the system and preclude observation of the predicted behaviors.

XIII. AUTOCAD TO SYMBAD CONVERSION UTILITY

The CAD package SYMBAD used for the design and fabrication of microelectronic and optoelectronic devices requires a mainframe computer and graphics workstation. This severely limits the utility of this CAD package. We have written an MS-DOS based utility called Autocon, which will translate AutoCAD generated DXF files to SYMBAD macro command language. Following the design rules and restriction listed, the user can design complex structures on a personal computer using AutoCAD, then translate and upload the file to the main frame computer for use in SYMBAD.

A. INTRODUCTION

Most microelectronic and optoelectronic fabrication work requires mask layout. This layout work is done on CAD packages (e.g. SYMBAD⁶⁰) specifically written to support and interface with microelectronic fabrication equipment. SYMBAD utilizes GDS-2, or "stream", which is the most popular of the available industry standards. Unfortunately, the really powerful and useful implementations of this standard are only available for use on mainframe computers. Also, they can be quite expensive to buy and maintain. A more reasonable solution for optoelectronic CAD tasks is to use programs available for the MS-DOS based personal computer (PC). The most powerful and flexible of the PC based CAD packages is AutoCAD⁶¹. While being reasonably priced and possessing all the functionality required of a micro-fabrication CAD package, it does not support the GDS-2 data file format.

Autocon is a file format conversion utility written in Microsoft QuickBASIC⁶¹. This utility translates AutoCAD generated DXF format file so SYMBAD macro command language. Once translated, the files output by Autocon may then be used to generate SYMBAD drawings. Thus, CAD work may be done on a PC using AutoCAD and then up-loaded to a mainframe for use in SYMBAD. This is much cheaper than doing all the CAD work on a mainframe since there is no user fee for the PC. Also, personal computer availability is much greater than that of a mainframe running SYMBAD. Autocon does not perform translation of SYMBAD files to DXF format.

This technical memo explains the design and operation of Autocon. An example of an actual translation is given. Source code for Autocon is in Appendix A. It is assumed that the user is familiar with AutoCAD and SYMBAD. No knowledge of Microsoft QuickBASIC is required to use Autocon.

Answers to questions regarding commands and procedures for these commercial packages should be sought in the appropriate manual or third party reference book.

B. AUTOCON CONVERSION UTILITY

Figure 1 shows the flow chart for Autocon. The user is prompted by Autocon to input the required file names. Once these have been entered, the program will proceed to translate the AutoCAD file to SYMBAD macro command language, without any further interaction with the user. Autocon searches the AutoCAD DXF file for layer information, block information, and finally for entity information. Blocks and entities are more fully discussed later. When each of these types of information is found, it is translated and recorded in the output file. All remaining information in the AutoCAD DXF file is extraneous and is ignored by Autocon. The AutoCAD DXF file is not modified by Autocon. Individual parts of the program will now be discussed.

The user is required to supply the name of the AutoCAD DXF file to be translated, the name of the output file in which the translation will be stored, the name of the appropriate SYMBAD library and the name of the SYMBAD cell in which the drawing will appear. The SYMBAD library must already exist within the user's mainframe account prior to executing the EXEC command, as described in the Operating Procedures section. In SYMBAD, a cell is a drawing file which may contain several objects, contain other cells, or be inserted itself into other cells (drawing files). The user must be careful not to use a cell name which already exists, or the EXEC command will over write the existing cell.

The bulk of the header information supplied by Autocon concerns identification of macro keys. The user may edit this information with an ASCII editor in the translated file if desired. For a permanent change to the macro key information, the source code of Autocon must be changed and re-compiled. Microsoft QuickBASIC does not allow use of double quotation marks (i.e. ") within source code. The double quotation marks identify the presence of literal string within the program. One set of double quotation marks identifies the beginning of the literal string and the next set the end of the string. Since the SYMBAD header requires that double quotes be supplied as needed, double quotation marks must be assigned to a variable through the ASCII character identification function CHR\$(34). The next to the last

header line allows for recording of SYMBAD system responses and can be very useful for identifying errors should they occur. The last header line contains commands required by SYMBAD as discussed in the SYMBAD users manual.

Both AutoCAD and SYMBAD require detailed information regarding each layer in the cad drawing. The conversion utility seeks out this information in the AutoCAD generated DXF format file and outputs the information in SYMBAD command language without any input from the user. Autocon first examines the entire DXF file and determines how many layers are present. This information is then printed on the screen for viewing by the user. Autocon ignores layer number 0. There is no way to translate the special properties of this layer as used in AutoCAD to SYMBAD. Therefore, layer number 0 must not be used within AutoCAD. The conversion utility next translates and outputs to the macro file each layer name, number and color. Since AutoCAD records layer color by assigning to each color a particular number, Autocon converts each layer's color number to text for SYMBAD. Autocon only supports seven colors and expects them to be assigned as explained below. As the information for each layer is output to the SYMBAD macro file, it is echoed to the screen for viewing by the user.

Drawings are stored in AutoCAD as entities and blocks. An entity is an individual object such as a rectangle or polygon. A block is a collection of entities (objects). As AutoCAD drawings increase in complexity, blocks may be nested within blocks. Autocon recognizes this and will translate the drawing data accordingly. SYMBAD stores all drawing data in cells. A cell in SYMBAD is analogous to a block in AutoCAD and may be nested in order to construct complicated drawings. Individual objects (as many as desired) are stored in each cell. Autocon stores AutoCAD block and entity information in SYMBAD cells. The conversion of nested blocks is handled by the subroutine ADD. Entity conversion is accomplished by the subroutine POLY. The master (top level) cell in SYMBAD may contain other (nested) inserted cells as well as individual objects. Autocon recognizes and translates AutoCAD data accordingly. Should the user accidentally supply Autocon with a corrupted DXF file containing no drawing information, Autocon will detect and report this on the screen. After all drawing information has

been processed, the conversion utility will report completion of the conversion to the user on the screen and allow conversion of more files.

With the exception of the user supplying a bad DXF file name, all errors cause termination of Autocon. An error reference number is reported during the termination sequence. The QuickBASIC manual lists the error codes and gives the most likely cause. Supplying Autocon with a bad DXF file name causes transfer to the part of the program called "errorhandler", which is the last section of code before listing of the subroutines. The bad file name error is trapped and causes Autocon to ask the user for a new file name.

Once an AutoCAD drawing has been generated, it must be prepared for conversion to SYMBAD format. This is done by using the "dxf out" command from within AutoCAD. This command Takes an AutoCAD file and converts it to the DXF text format. These file types are identifiable by the DXF extension AutoCAD adds to the file name.

The conversion utility is stored under the name autocon.exe. The program is started by typing Autocon (assuming that Autocon is in the current directory). The program will then type on the screen:

"Type the name of the AutoCAD file you wish to convert"

"Be sure to include the .dxf extension."

After the user supplies the name of the DXF file to be converted, Autocon will print to the screen:

"Type the name of the output file."

"BE CAREFUL!"

"IF THE FILENAME ALREADY EXISTS, IT WILL BE OVERWRITTEN!"

The output file name supplied here will be used from within the polygon editor of SYMBAD to create the actual SYMBAD drawing. The conversion utility next prompts the user for some information required by SYMBAD. Autocon will type on the screen:

"Type the name of the SYMBAD LIBRARY file"

After receiving this information, Autocon will type on the screen:

"Type the name of the SYMBAD CELL file"

This the last input required of the user by Autocon. The conversion utility will then inform the user of the number of layers found in the DXF file and the name and color of each layer. When conversion has been completed Autocon will print on the screen:

"dxf file name has been converted and saved in SYMBAD file output file name"

"Do you wish to process another file?"

Autocon will return the computer to the current directory after the last DXF file had been processed.

The output files generated by Autocon must now be placed in the user's directory on the computer which runs SYMBAD. File transfer may be done by ftp between main frames, or by direct up-load from an MS-DOS computer which is hooked up to the main frame computer. The directory must contain the SYMBAD technology file, as discussed in the SYMBAD user's manual. The final steps of conversion are accomplished from within the polygon editor of SYMBAD. After starting SYMBAD, the user types on the SYMBAD command line:

"EXEC file name"

File name here refers to the file output by Autocon. SYMBAD will open the file and read each line. As each line is read, it is typed on the command line and executed. SYMBAD may ask questions of the user just as it does during a normal session. For example, when a new cell is opened, SYMBAD will inform the user that the cell could not be found and will ask the user if the cell should be created. The user should answer yes to this and should answer all other questions as they would be answered during a normal interactive session. Should SYMBAD come upon a statement which requires the user to decide whether to abort or continue, continue should always be selected. When SYMBAD has EXECed the last line of the file, the entire drawing generated in AutoCAD should now be in the current open cell. All objects may now be manipulated normally within SYMBAD. A file named "Session," which SYMBAD generates, contains a transcript of the entire on-line session. This file should be examined if an error occurs.

SYMBAD and AutoCAD have same fundamental differences in operation and construction for which the conversion utility Autocon cannot compensate. A set of restrictions and design rules must be followed

by the user in order to prevent errors in translation. Such errors could result in misplaced objects in the converted SYMBAD drawing or other serious mistakes. The rules to follow are:

1. When a block is defined in AutoCAD, the x and y values used to define the block insertion point must correspond to the set of lowest coordinates of all the objects and inserted (nested) blocks within the block. This can usually be accomplished by locating the lower left most set of coordinates of all the entities used within a block and designating that set of coordinates as the block insertion point when defining the block.
2. Set the grid scale as required from within the SYMBAD polygon editor before using the EXEC command.
3. Be sure to use the following numbering convention for colors in AutoCAD when defining layers:
 - 1 = red
 - 2 = yellow
 - 3 = green
 - 4 = cyan
 - 5 = blue
 - 6 = magenta
 - 7 = white
4. The top level (master) block in AutoCAD should not have any rotated objects, entities or block insertions. Each object, entity and block needing rotation in the master block should be drawn, rotated, defined as a block, and then inserted into the master block. This precludes a simultaneous rotation and insertion in the master block which can lead to translation errors.
5. Do not use the WRB feature of AutoCAD. All block information must be contained within the file to be translated.
6. Do not use layer zero (0) in AutoCAD. This layer has certain properties that are not compatible with SYMBAD and cannot be translated.

AutoCAD is capable of generating CAD drawings with a level of complexity equal to that of SYMBAD. If the design rules stated above are followed, the user should not be restricted in terms of the

level of complexity in any particular drawing. However, practical experience shows that a more cautious approach should be followed. It is best to break up the AutoCAD drawing into smaller logical units rather than to try and put all the parts into one massive drawing. Each unit should be assigned its own SYMBAD cell name, translated and then assembled into the final master cell within SYMBAD. This way, an error in one part of the drawing can more easily be corrected.

C. SUMMARY AND CONCLUSIONS

A translation utility for converting DXF type data files to SYMBAD macro-command language format has been produced and tested. This translation utility, Autocon, has been written in Microsoft QuickBASIC for MS-DOS based PCs. Use of this utility enables the user to produce CAD files on the PC using AutoCAD, translate the data files to SYMBAD's macro-command language, and then execute the translated files from within SYMBAD. The result is a copy of the AutoCAD drawing that is usable from within SYMBAD.

Testing of Autocon has revealed that certain design rules and restrictions must be followed from within AutoCAD. These restrictions are a result of fundamental differences between the approaches taken by AutoCAD and SYMBAD with regard to the handling of drawn objects and reference coordinate systems. It has also been learned that breaking up a complex drawing into several smaller units makes error correction easier to perform. If the rules and restrictions are strictly adhered to, drawings of any complexity can be translated.

XIV. CONCLUSIONS / SUMMARY

The 4600P305 work unit presents some of the devices necessary to develop an integrated optical signal processor. Such a processor would have optical logic gates, memory elements, optical waveguides to interconnect the devices, I/O devices and electrical bias. The main problem with most of the devices presented in this report is the lack of gain. For without gain, the logic gates and memory elements can not be optically connected or cascaded with other such devices. A follow-on work unit is in the process of demonstrating a Configurable Optical Gate with optical gain in excess of 20 and on/off contrast ratios exceeding 500:1. A small integrated optical processor will be demonstrated.

A similar situation exists for the optical amplifiers. They can not be cascaded indefinitely due to the possibility of amplifying spontaneous emission. The bandwidth of the spontaneous emission is narrow compared with most filters and, for a variety of reasons, present optical filters are insufficient. The work in 4600P305 has demonstrated that the angled facets inhibit lasing and increase the threshold current as is required for laser amplifiers and has resulted in a new type of optical amplifier that includes an integrated spontaneous emission filter. Such a filter should eliminate the problem with cascading. The optical amplifiers should be cascaded and monolithically integrated for many applications. One problem here is that the cavity facets need to be Anti Reflection coated. A follow on work unit is developing a process to allow multiple in-plane devices to be simultaneously AR coated.

Thus the goal of a preliminary investigation of devices to produce a working optical signal processor has been met. Future work will include the new devices discussed above and also the integration of conventional electronics. A future optical processor will most likely have multiple planes of devices optically interconnected. Such an architecture naturally favors a Vertical Cavity Surface Emitting Laser (VCSEL) for the interconnect. If each VCSEL is also used for both interconnect and logic functions (smart pixels) then the packing density and throughput can greatly exceed present technology. Work units have been developed to investigate these issues.

REFERENCES

1. Feitelson, D. G., Optical Computing. A Survey for Computer Scientists. The MIT Press, Cambridge, MA, 1988.
2. Grande, W. J., A Study of Gallium Arsenide-Aluminum Gallium Arsenide Semiconductor Laser Devices for Monolithic Integrated Optical Circuits, PhD. Dissertation, Cornell University, Ithaca, NY 14853, 1989.
3. Arakawa, Y., and Yariv, A., IEEE J. Quantum Electronics, QE-22, 1887, 1986 and ref. therein.
4. Gao, D. S., Kang, S. M., Bryan, R. P., Coleman, J. J., IEEE J. Quantum Electronics, 26, 1206, 1990.
5. Yee, T. K., and Welford, D., IEEE J. Quantum Electronics, QE-22, 2116, 1986.
6. Kawaguchi, H., Appl. Phys. Lett., 45, 1264, 1984.
7. Ueno, M., and Lang, R., J. Appl. Phys., 58, 1689, 1985.
8. Eng, L., and Yariv, A., Darpa Optics Review, Melbourne Fl, 1992.
9. Swanson, P. D., Libby, S. I., and Parker, M. A., "The Fabrication of Ridge Waveguided Photonic Circuits with Chemically Assisted Ion Beam Etched Mirrors," RL Technical Report, Mar. 1992.
10. Libby, S. I., Swanson, P. D., and Parker, M. A., "Optical Logic Gate and Component Analysis Techniques," RL Technical Report, RL-TR-92-98, August 1992.
11. Parker, M. A., Libby, S. I., and Swanson, P. D., "The Components of an Optical RS Flip-Flop for an Integrated Optical Processor," RL Technical Report, RL-TR-92-87, July 1992.
12. Herzinger, C. M., Swanson, P. D., Tang, T. K., Cockerill, T. M., Miller, L. M., Givens, M. E., DeTemple, T. A., Coleman, J. J., and Luburton, J. P., Phys. Rev. B, 44, 13478, 1991.
13. Jackson, K. P., Harker, Ch., Buchmann, P., and Datwyler, K., IEEE Photon. Technol. Lett., 2, 832, 1990.
14. Ajiwara, A., Fujiwara, M., Shimizu, J., Sugimoto, M., Uchida, M., and Ohta, Y., Electron. Lett., 23, 1121, 1978.
15. Grande, W. J., and Tang, C. L., Appl. Phys. Lett., 51, pp. 1780, 1987.
16. Grande, W. J., Braddock, W. D., Sheally, J. R., and Tang, C. L., "One-Step Two Level Etching Technique for Monolithic Integrated Optics," Appl. Phys. Lett., Vol. 51, No. 26, pp. 2189-2191, Dec 1987.
17. Grande, W. J., Johnson, J. E., and Tang, C. L., "Characterization of etch rate and anisotropy in the temperature-controlled chemically assisted ion beam etching of GaAs," J. Vac. Sci. Technol., Vol. B8, No. 5, pp. 1075-1079, September/October 1990.
18. Marcuse, D., Theory of Dielectric Optical Waveguides, pp. 330-334, Academic Press, Inc., New York, 1991.
19. Lin, C. F., M. S. Thesis, Cornell University, May 1989.
20. Williams, R. E., Gallium Arsenide Processing Techniques, Artech House, Dedham, 1984.
21. Rhoderick, E. H., Metal-Semiconductor Contacts, Clarendon Press, Oxford, 1980.
22. Parker, M. A., and Schiff, E. A., Appl. Phys. Lett., 48, 1087, 1986.
23. Parker, M. A., Conrad, K. A., and Schiff, E. A., MRS Proceedings, Vol. 70, 1986.
24. Street, R. A., Phys. Rev. B, 32, 3910, 1985.
25. Abkowitz M., and Scher, H., Phil. Mag., 35, 1585, 1977.
26. Olbright, G. R., Private Communication, Photonic Research, Inc., Boulder, CO.
27. Sze, S. M., Physics of Semiconductor Devices, 2nd Ed., John Wiley & Sons, New York, 1981.
28. Parker, M. A., Libby, S. I., and Swanson, P. D., "An Optical NOR Gate Based on GaAs-AlGaAs Heterostructure Lasers," RL Technical Report (May 1992).
29. Libby, S. I., and Parker, M. A., "Low Duty-Cycle Device Tester," Rome Laboratory In-House Report, RL-TM-91-1.
30. Libby, S. I., Parker, M. A., and Swanson, P. D., "Preliminary Analysis of Multimode Semiconductor Laser Amplifiers with Angled Facets," Rome Laboratory In-House Report (Submitted).
31. Olbright, G. R., Bryan, R. P., Jewell, J. L., and Brennan, T. E., "Surface-Emitting Laser Logic for Digital Optical Computing," RL Technical Report, RL-TR-92-137.
32. Verdeyen, J., Laser Electronics, second edition, p129.
33. O'Mahony, M. J., IEEE J. Lightwave Technology, 6, 253, 1988.

34. G. T. E. Laboratories, Optical Amplifier Study - Final Report, Contract F30602-87-C-0107 (1989).
35. Fye, D. M., IEEE J. Lightwave Technology, LT-2, 1984.
36. Saitoh, T., and Mukai, T., "Recent Progress in Semiconductor Laser Amplifiers," IEEE J. of Lightwave Technology, Vol. 6, No. 11, pp. 1656-1664, November 1988.
37. O'Mahony, M. J., J. Lightwave Technology, 6, 531, 1988.
38. Zah, C. E., Osinski, J. S., Caneau, C., Menocal, S. G., Reith, L. A., Salzman, J., Shokoohi, F. K., and Lee, T. P., "Fabrication and Performance of 1.5 μ m GaInAsP Travelling-Wave Laser Amplifiers with Angled Facets," Electronics Letters, Vol. 23, No. 19, pp. 990-992, September 1987.
39. Parker, M. A., Libby, S. I., and Swanson, P. D., "The Importance of Optical Loss for the Differential Efficiency and Threshold Current in Multi-quantum Well Lasers," Rome Laboratory Technical Memorandum, RL-TM-92-13, July 1992.
40. Shigihara, K., Nagai, Y., Karakida, S., Takami, A., Kokubo, Y., Matsubara, H., and Kakimoto, S., "High Power Operation of Broad-Area Laser Diodes with GaAs and AlGaAs Single Quantum Wells for Nd:YAG Laser Pumping," IEEE J. Quantum Electr., 27, 1537, pp. 1537-1543, 1991.
41. Sakamoto, M., Welch, D. F., Harnagel, G. L., Streifer, W., Kung, H., Scifres, D. R., "Ultrahigh Power 38W Continuous-Wave Monolithic Laser Diode Arrays," Appl. Phys. Lett., 52, 2220, pp. 97-99, 1988.
42. Lasher, G. J., Solid-State Electronics, 7, 707, 1964.
43. Jung W., and Kwon, Y., Jap. J. Appl. Phys., 28, L1242, 1989.
44. Parker, M. A., Olewicz, A., Libby, S., and Honey, D., "P⁺ Electrical Contacts on GaAs for Semiconductor Lasers," RL Technical Report, RL-TR-92-242, October 1992.
45. Tang, C. L., Schremer, A., and Fujita, T., Appl. Phys. Lett., 51, 1392, 1987, and references therein.
46. Odagawa, T., and Yamakashi, S., Electronics Letters, 25, 1429, 1989.
47. Harder, C., Lau, K. Y., and Yariv, A., IEEE J. Quant. Elect., QE-18, 1351, 1982.
48. Lang, R., J. Appl. Phys., 19, L93, 1980.
49. Gibbs, H. M., McCall, S. L., and Venkatesan, T. N. C., Optical Engineering, 19, 463, 1980.
50. Smith, P. W., Optical Engineering, 19, 456, 1980.
51. Ikeda, K., and Kondo, K., Phys. Rev. Lett., 49, 1467, 1982.
52. Chrostowski, J., Delisle, C., and Tremblay, R., Canadian J. Phys., 61, 188, 1983.
54. Chrostowski, J., and Delisle, C., Optics Comm., 41, 71, 1981.
53. Korpel, A., Acousto Optics, Marcel Dekker, Inc., 1988.
55. Banerjee, P. P., and Poon, T. C., 30th Midwest Symp. on Circuits and Systems, Eds. G. Glasford and K Jabbour, pp. 820-822, Elsevier Science Publishing Co., Inc., 1988.
56. Banerjee, P. P., and Poon, T. C., Principles of Applied Optics, pp. 321, Irwin Inc and Aksen Associates Inc., 1991.
57. May, R. M., Nature, 261, 459, 1976.
58. Poon, T. C., and Cheung, S. K., Appl. Opt., 28, 4787, 1989.
59. Chrostowski, J., Vallee, R., and Delisle, C., Canadian J. Phys., 61, 1143, 1983.
60. SYMBAD Polygon Editor, Cadence Corporation, 555 River Oaks Parkway, San Jose, CA 95134
61. AutoCAD by AUTODESK Corporation, 2320 Sausalito, CA 94965
62. Micorsoft QuickBASIC Version 4.5, Microsoft Corporation, One Microsoft Way, Redmond, WA 98052-6399.

APPENDIX

(Note: Appendices are labeled according to their associated chapters.)

APPENDIX 2.A: Relation For Photon Density, Mirror Reflectivity, Irradiance and Flux

The power emitted from one of the laser facets can be related to the photon density inside the laser cavity. Photons in the cavity travel in either of two directions. Thus the number striking a given mirror per second in each unit area of the mirror is given by $(\gamma/2)v_g$ where v_g is the velocity of light in the gain medium. Each photon has the energy hc/λ where c and λ are the speed and wavelength of light in vacuum respectively. Thus the irradiance of light striking each mirror from within the cavity is $I_c = (\gamma/2)v_g hc/\lambda$. The irradiance from the laser facet I_r (Watts/cm²) and the optical flux L (Watts) are given by

$$I_r = (1-R) I_c = (1-R) \left(\frac{\gamma}{2} \right) v_g h \frac{c}{\lambda} \quad (2A1a)$$

$$L = I_r A_b = A_b (1-R) \left(\frac{\gamma}{2} \right) v_g h \frac{c}{\lambda} \quad (2A1b)$$

where the reflectivity R is between 0 and 1, and A_b is the cross sectional area of the beam.

APPENDIX 2B: Relation Between the Mirror Reflectivity and the Cavity Lifetime

A relation between the part of the cavity lifetime attributable to mirrors D_m and the reflectivity R must be determined; this can be accomplished by considering a Fabre-Perot cavity, which has no internal loss, with two identical mirrors of reflectivity R . The relation between D_m and R can be determined exactly, but the solution to the steady state form of equation 2.2 loses its simple form. The exact relation between D_m and R takes proper account of the propagation delay between the two mirrors for a given infinitesimal volume of optical energy. The actual photon density as a function of time can be bounded above and below by two approximate photon densities which are based on the approximate relation between D_m and R . The approximate relation obtains by calculating the optical energy remaining in the cavity at the end of each trip across the cavity and then extending the solution to intermediate times. This method takes into account the time required for the optical energy to travel the length of the cavity but the solution is only approximate because of the assertion that it should hold for all times. The second approximation for the photon density -- the one which provides the upper bound -- obtains from the first by taking R close to unity and then stipulating that the approximation hold for all values of R . The choice of the approximate relation between D_m and R greatly affects the functional dependence of the differential efficiency and, to a lesser extent, the threshold current upon the reflectivity. The use of the two approximate relations between D_m and R allows one to bound the photon density in the Fabre-Perot cavity and also bound the behavior of the differential efficiency and threshold current of the lasers.

The first approximate relation is found by considering the propagation of the optical energy across the Fabre-Perot cavity. The reflectivity R takes on values between 0 and 1 and both mirrors are assumed to have the same reflectivity. If U_0 is the initial optical energy within the cavity then $U_0 R^m$ is the energy after m reflections. The light travels the length L_c of the cavity at the group velocity v_g so that m reflections require the time $t = m (L_c/v_g)$. The expression for the energy remaining in the cavity can then be rewritten as $U(t) = U_0 R^m = U_0 \exp [- t (v_g / L_c) \ln(1/R)]$. Thus,

$$\frac{U(t)}{U_0} = e^{-\frac{t}{D_m}} \quad (2B1a)$$

$$D_m = \frac{L_c}{v_g \ln\left(\frac{1}{R}\right)} \quad (2B1b)$$

where equation 2B1a is assumed to hold for all times. Equation 2B1b shows that higher reflectivity mirrors produce longer lifetimes. For example, a typical semiconductor laser 100 μm long with reflectivities of $R \approx 0.33$ for the cleaved mirrors and $v_g = 0.85 \times 10^{10}$ cm/sec will have a mirror cavity lifetime of $D_m \approx 1$ picosecond.

The upper bound on the photon density in the cavity obtains from equation 2B1b by approximating $\ln(1/R)$ with $(1-R)$. The energy remaining in the cavity at time t becomes

$$\frac{U(t)}{U_0} = e^{-\frac{t}{D_m}} \quad (2B2a)$$

$$D_m = \frac{L_c}{v_g (1-R)} \quad (2B2b)$$

As an aside, equation 2B2 can be obtained directly from first principles by applying the equation of continuity to the optical energy in the cavity and the energy flux through the mirrors.

An expression for the energy remaining in the cavity can be found which properly takes into account the delay factor and holds for all times. The expression is obtained by dividing the cavity energy into infinitesimal lengths Δx along the cavity, calculating the loss of energy from each infinitesimal length at the mirror in the time $\Delta x/v_g$, and then summing the remaining energy in the infinitesimal lengths in the cavity. The expression for the remaining energy $U(t)$ is given by

$$\frac{U(t)}{U_0} = \{ 1 - [t - \Phi(t)](1-R) \} R^{\Phi(t)} \quad (2B3)$$

where t is in units of L_c/v_g and $\Phi(t)$ is the largest integer which does not exceed the value of t . For values of t which are multiples of L_c/v_g (that is, t is an integer in the previous equation), equation 2B3 reduces to equation 2B1. $U(t)$ decreases linearly between these points.

The three expressions for the photon density agree fairly well with each other for large values of R . The approximations tend to breakdown for low reflectivities. If, for example, $R=0$ then the cavity energy should pass through the mirrors without any reflection and the energy in the cavity should decrease linearly

to zero. Equations 2B1 and 2B3 predict this behavior but equation 2B2 predicts an exponential decay. Small nonzero values of R cause the optical energy predicted by equation 2B1 to be small compared with that predicted by equation 2B3 except for times which are a multiple of L_c/v_g . The behavior appears in figure 2B1 for $R=0.1$; the plot has been normalized to unity at $t=0$. Also note that the Taylor expansion for $\ln(1/R)$, equation 2B2 and curve 2, yields a better approximation to the infinitesimal volume approach, equation 2B3 and curve 3, for small times than does the R^m approximation in equation 2B1 and curve 1. Even though the laser equations are

solved under steady state conditions, which is equivalent to finding the solutions for very long times, the short time behavior of the cavity loss term in equation 2.2 can not be ignored. The irradiance at time t can be viewed as the sum of

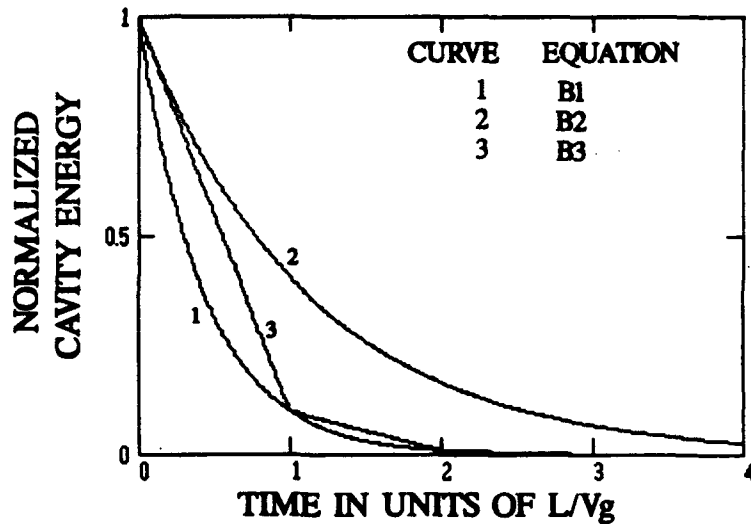


Figure 2B1: A plot of the normalized cavity energy as given by equations 2B1, 2B2 and 2B3 for $R = 0.1$.

contributions from photons produced in the cavity for times earlier than time t through a convolution integral. Thus the irradiance has contributions from the cavity loss term which encompass the short time behavior discussed above. For reflectivities above 0.35, the equation 2B1 yields results well within 5% of those from equation 2B3.

APPENDIX 4A: DISTRIBUTED IMPEDANCE MODELS

A distributed impedance approach can also be used to explain results obtained from certain electrode geometries. The electrodes shown in figure 4A1 approximate a set of contacts fabricated for this study. Semiconductor lasers use a similar construction except one of the metal electrodes would be a very low resistance one which carries the current common to all of the devices on the wafer. The narrow metal electrodes have resistances on the same order of magnitude as the doped GaAs. The voltage drop along the metal electrodes becomes significant at high currents; this drop is nonlinear with the distance along the electrodes.

The electrode structures shown in figure 4A1 can be analyzed by dividing the metal electrodes and GaAs into lengths dx . The structures are then represented as the series combination of resistances dR_m for the electrodes and the parallel combination of conductances dG for the semiconductor. The voltages $V_t(x)$ and $V_b(x)$ refer to the voltage of the node at point x on the upper and lower branches respectively. The current $I_t(x)$ and $I_b(x)$ are calculated by applying Ohm's law to each element dR_m with dV_t and dV_b as the voltage drop between adjacent nodes.

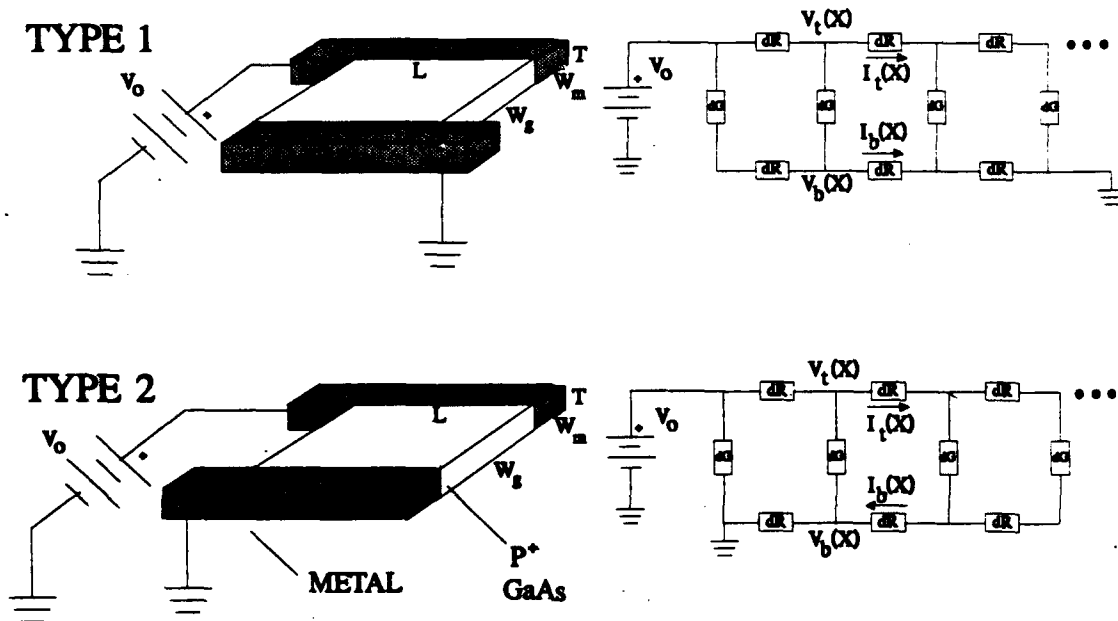


Figure 4A1: Two contact structures (left) and the corresponding discrete component circuit models (right). The top and bottom circuit elements dR represent the infinitesimal resistances along the metal pads. dG is the conductance of a thin strip of GaAs between the two pads. The contact resistance R_c is included with the dG term.

The basic relation between resistance R , resistivity ρ , length L and cross sectional area A , namely

$R = \rho \frac{L}{A}$, can be applied to the metal electrodes as $dR_m = \rho_m \frac{dx}{A} = R_m \frac{dx}{L}$ and to the GaAs as $dG = \frac{T dx}{\rho_g W_g} = \frac{1}{R_g} \frac{dx}{L}$. The circuit equations and boundary conditions for the type 1 and 2 electrode structures are:

Type 1 Equations

$$(4A1a) \quad dV_t = -I_t(x) dR_m$$

$$(4A2a) \quad dV_h = -I_h(x) dR_m$$

$$(4A3a) \quad dI_t = -dG [V_t(x) - V_h(x)]$$

$$(4A4a) \quad \frac{dI_t}{dx} = \frac{dI_h}{dx}$$

$$(4A5a) \quad V_n - V_t(x) = V_h(L-x)$$

Type 2 Equations

$$(4A1b) \quad dV_t = -I_t(x) dR_m$$

$$(4A2b) \quad dV_h = I_h(x) dR_m$$

$$(4A3b) \quad dI_t = -dG [V_t(x) - V_h(x)]$$

$$(4A4b) \quad I_t(x) = I_h(x)$$

$$(4A5b) \quad V_n - V_t(x) = V_h(x)$$

Type 1 Boundary Conditions

$$(4A6a) \quad V_t(0) = V_n$$

$$(4A7a) \quad V_h(L) = 0$$

$$(4A8a) \quad I_t(L) = 0$$

$$(4A9a) \quad V_h(0) = 0$$

Type 2 Boundary Conditions

$$(4A6b) \quad V_t(0) = V_n$$

$$(4A7b) \quad V_h(0) = 0$$

$$(4A8b) \quad I_t(L) = 0$$

$$(4A9b) \quad I_h(L) = 0$$

The circuit equations can be rewritten as first order, linear differential equations in x as

Type 1 Equations

$$(4A10a) \quad \frac{dV_t}{dx} = -I_t \frac{R_m}{L}$$

$$(4A11a) \quad \frac{dV_h}{dx} = -I_h \frac{R_m}{L}$$

$$(4A12a) \quad \frac{dI_t}{dx} = -\frac{1}{LR_g} [V_t(x) - V_h(x)]$$

$$(4A13a) \quad \frac{dI_h}{dx} = -\frac{dI_t}{dx}$$

$$(4A14a) \quad V_n - V_t(x) = V_h(L-x)$$

Type 2 Equations

$$(4A10b) \quad \frac{dV_t}{dx} = -I_t \frac{R_m}{L}$$

$$(4A11b) \quad \frac{dV_h}{dx} = I_h \frac{R_m}{L}$$

$$(4A12b) \quad \frac{dI_t}{dx} = -\frac{1}{LR_g} [V_t(x) - V_h(x)]$$

$$(4A13b) \quad I_h(x) = I_t(x)$$

$$(4A14b) \quad V_n - V_t(x) = V_h(x)$$

Equations 4A3 and 4A12 are obtained from the current flow from the upper to the lower branch.

Equations 4A4, 4A5, 4A13 and 4A14 are obtained from the symmetry of the circuits.

Solutions to Type 1 Equations:

$$\frac{V_t(x)}{V_0} = \frac{e^{b(1-x/L)} + e^{bx/L} + \frac{b}{L}(1-e^b)x + 1 - b + (1+b)e^b}{2(1+e^b) - b(1-e^b)} \quad (4A15)$$

$$\frac{V_b(x)}{V_0} = \frac{-e^{b(1-x/L)} - e^{bx/L} + \frac{b}{L}(1-e^b)x + 1 - b + (1+b)e^b}{2(1+e^b) - b(1-e^b)} \quad (4A16)$$

$$\frac{I_t(x)}{V_0/R_m} = \frac{b e^{b(1-x/L)} - b e^{bx/L} - b(1-e^b)}{2(1+e^b) - b(1-e^b)} \quad (4A17)$$

$$\frac{I_b(x)}{V_0/R_m} = \frac{-b e^{b(1-x/L)} + b e^{bx/L} - b(1-e^b)}{2(1+e^b) - b(1-e^b)} \quad (4A18)$$

where

$$b = +\sqrt{\frac{2R_m}{R_g}} \quad (4A19)$$

Solutions to Type 2 Equations:

$$V_t(x) = \frac{V_0}{2} \left(1 + \frac{e^{b(1-x/L)} + e^{-b(1-x/L)}}{e^b + e^{-b}} \right) \quad (4A20)$$

$$V_b(x) = \frac{V_0}{2} \left(1 - \frac{e^{b(1-x/L)} + e^{-b(1-x/L)}}{e^b + e^{-b}} \right) \quad (4A21)$$

$$I_t(x) = I_b(x) = \frac{V_0}{2} \sqrt{\frac{2}{R_m R_g}} \frac{e^{b(1-x/L)} - e^{-b(1-x/L)}}{e^b + e^{-b}} \quad (4A22)$$

where b is given by equation 4A19. Figure 4A2 shows $V_t(x)$ and $I_t(x)$ for the two types.

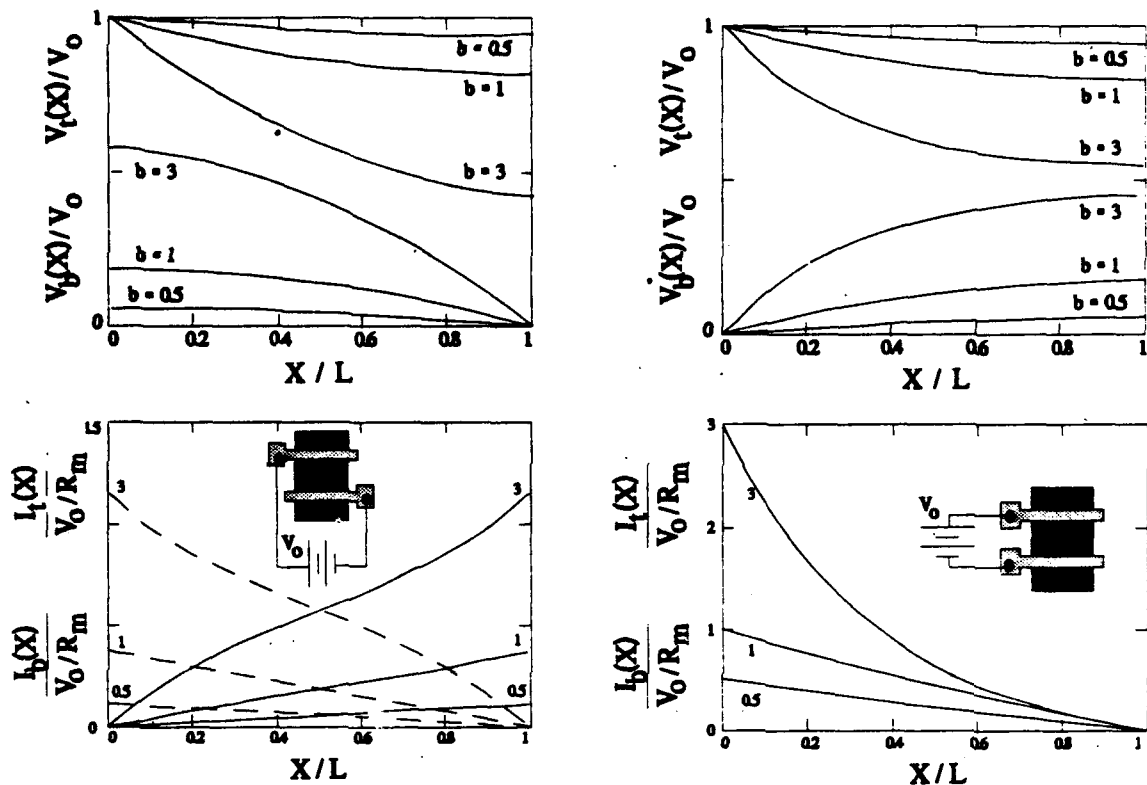


Figure 4A2: The voltage distribution (top) and current distribution (bottom) along the metal electrodes for the type 1 (left) and type 2 (right) electrode structures. The curves are parameterized by b . For the voltage plots, $V_t(x)$ and $V_b(x)$ are the top most and bottom most curves, respectively. The plots of the current in the top electrode for the type 1 structure (bottom left) are represented by dashed lines. Only one set of curves appears for the current in the electrodes of the type 2 structure since $I_t(x)$ and $I_b(x)$ are identical.

These two sets of solutions yield equivalent input resistances R_{eff} for the respective contact structure. R_{eff} is nonlinear in the GaAs and metal resistances and it is defined to be $V_0 / I_t(0)$. Another quantity of interest is the ratio of the voltage drop along one of the narrow metal electrodes $\Delta V = V_0 - V(L)$ to the voltage applied across the contact structure V_0 . The two sets of equations yield the following results. A plot of the effective resistance appears in figure 4A3.

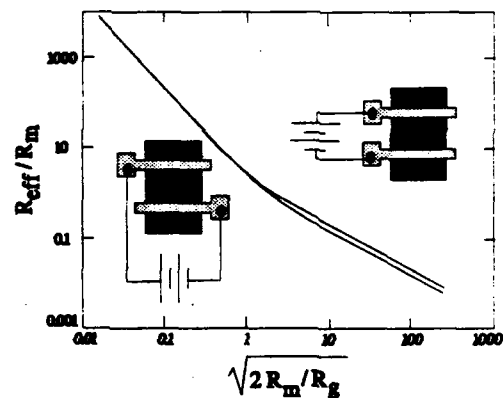


Figure 4A3: The effective input resistance as a function of the metal and P^+ GaAs resistance. The top and bottom curves correspond to the type 1 and type 2 structures respectively.

Type 1:

$$(4A23a) \quad R_{\text{eff}} = \sqrt{\frac{R_m R_g}{2}} \left(\frac{e^b + 1}{e^b - 1} + \frac{1}{2} \right)$$

$$(4A24a) \quad \frac{\Delta V}{V_0} = \frac{b(e^b - 1)}{2(1 + e^b) - b(1 - e^b)}$$

Type 2:

$$(4A23b) \quad R_{\text{eff}} = 2 \sqrt{\frac{R_m R_g}{2}} \frac{e^b + e^{-b}}{e^b - e^{-b}}$$

$$(4A24b) \quad \frac{\Delta V}{V_0} = \frac{1}{2} - \frac{1}{e^b + e^{-b}}$$

The distributed impedance model for the GL100 contact structures can be summarized by figures 4A2 and 4A3. Figure 4A2 shows the voltage and current distribution along the length of the electrodes. As the ratio of the metal to GaAs resistance becomes small (small values for b), the voltage drop along the electrodes also becomes small. The upper right graph in figure 4A2 shows that the unconnected ends of the type 2 metal electrodes have voltages which can be close for large values of b . As expected from the zero current boundary conditions (Eqs. 4A8a and 4A8b), the current in each electrode approaches zero at one point along its length. Figure 4A3 shows that the geometry of the structure has little influence on its total resistance.

Appendix 13.A Autocon Program Listing

```
DECLARE SUB ADD ()
DECLARE SUB POLY ()
***** AUTOCON6.BAS *****
' ***** The purpose of this program is to convert an Autocad dxf format
' file to SYMBAD macro command language. *****

'***** Get the name of the Autocad file with the dxf extension to convert
start: 'Control is passed to here for successive runs
CLS
COLOR 15, 1
CLS
COLOR 15, 1
PRINT "Type the name of the Autocad file you wish to convert."
PRINT "Be sure to include the .dxf extension."
INPUT "", AS      'AS = Autocad file name

'***** Open the Autocad.dxf file
ON ERROR GOTO errorhandler 'Takes care of bad filename error
OPEN AS FOR INPUT AS #1

'***** Get the name of the output file
PRINT ""
PRINT "Type the name of the output file."
COLOR 31, 4
PRINT "BE CAREFUL!";
COLOR 15, 1
PRINT " IF THE FILENAME ALREADY EXISTS, IT WILL BE OVERWRITTEN!!!!"
INPUT "", BS      'BS = SYMBAD file name

'***** Get the name of the SYMBAD LIBRARY file
PRINT
PRINT "Type the name of the SYMBAD LIBRARY file"
INPUT "", c$      'CS = SYMBAD LIBRARY file name

'***** Get the name of the SYMBAD CELL file
PRINT
```

```

PRINT "Type the name of the SYMBAD CELL file"
INPUT "", D$      D$ = SYMBAD CELL file name
'***** Open the SYMBAD output file
OPEN B$ FOR OUTPUT AS #2

'***** Put in SYMBAD header
PRINT #2, "TRANSCRIPT OFF"
Q$ = CHR$(34) 'Q$ = "      This is necessary for the SYMBAD header,
                        and the only way to output a " in QuickBasic
PRINT #2, "DEFINE KEY <f17> "; Q$; "exe CADMACROS:gs$CR"; Q$
PRINT #2, "DEFINE KEY <f18> "; Q$; "SHOW LIB CAT$CR"; Q$
PRINT #2, "DEFINE KEY <f19> "; Q$; "CLOSE CELL$CR"; Q$
PRINT #2, "DEFINE KEY <f1> "; Q$; "VIEW LEVEL$CR"; Q$
PRINT #2, "DEFINE KEY <f2> "; Q$; "VIEW DOWN$CR"; Q$
PRINT #2, "DEFINE KEY <f3> "; Q$; "MAX VIEW LEVEL$CR"; Q$
PRINT #2, "DEFIN KEY <f4> "; Q$; "VIEW LEFT$CR"; Q$
PRINT #2, "DEFINE KEY <f5> "; Q$; "VISIBLE LAYERS$FT"; Q$
PRINT #2, "DEFINE KEY <f6> "; Q$; "VIEW RIGHT$CR"; Q$
PRINT #2, "DEFINE KEY <f7> "; Q$; "VIEW SCALE 0.5$CR"; Q$
PRINT #2, "DEFINE KEY <f8> "; Q$; "VIEW UP$CR"; Q$
PRINT #2, "DEFINE KEY <f9> "; Q$; "VIEW SCALE 2$CR"; Q$
PRINT #2, "DEFINE KEY <pf1> "; Q$; "POINT UNSELECT$CR"; Q$
PRINT #2, "DEFINE KEY <pf2> "; Q$; "DELETE SELECTED$CR"; Q$
PRINT #2, "DEFINE KEY <pf3> "; Q$; "MODIFY OBJECT SELECTED $FT"; Q$
PRINT #2, "DEFINE KEY <pf4> "; Q$; "MODIFY OBJECT $FT"; Q$
PRINT #2, "TRANSCRIPT ON"
PRINT #2, "INITIALIZE LIBRARY "; c$; " BASIC"      'BASIC is the techfile name

'***** Find layer information in Autocad file and store in SYMBAD file
'***** Find the number of layers present
FOR I = 1 TO 10000
    INPUT #1, E$      'E$ = current record from Autocad file
    IF E$ = "EOF" THEN I = 10000      'Loop should now be terminated
    IF E$ = "LAYER" THEN
        INPUT #1, E$:      'E$ should = 70
        INPUT #1, nl      'nl should = number of layers
        PRINT "The file "; A$; " contains "; nl - 1; " layers"
                        'nl - 1 = # of layers, ignoring layer 0.
        I = 10000      'Terminate this loop
    END IF
NEXT I

'***** Find information for each layer and store it in SYMBAD file
lnum = 0      'Layer number to be used in DEFINE LAYER below

```

PRINT "Layer information follows:"

FOR I = 1 TO 10000

INPUT #1, ES

IF ES = "LAYER" THEN

INPUT #1, ES 'ES = 2

INPUT #1, lname\$ 'lname\$ = layer name or number (if no name was
'assigned)

IF lname\$ = "0" THEN GOTO layend 'Ignore layer 0

lnum = lnum + 1

INPUT #1, ES 'ES = 70

INPUT #1, ES 'ES = 0

INPUT #1, ES 'ES = 62

INPUT #1, lcolor\$ 'lcolor\$ = layer color number

SELECT CASE lcolor\$ 'convert color number to text for SYMBAD

CASE "1": lcolor\$ = "red"

CASE "2": lcolor\$ = "yellow"

CASE "3": lcolor\$ = "green"

CASE "4": lcolor\$ = "cyan"

CASE "5": lcolor\$ = "blue"

CASE "6": lcolor\$ = "magenta"

CASE "7": lcolor\$ = "white"

END SELECT

PRINT #2, "DEFINE LAYER "; lnum; lname\$, " "; lcolor\$

PRINT "DEFINE LAYER "; lnum; lname\$, " "; lcolor\$

END IF

IF ES = "ENDSEC" THEN I = 10000

layend:

NEXT I

***** Convert Autocad blocks to SYMBAD cells *****

FOR I = 1 TO 10000 Find BLOCKS label in Autocad file

IF ES = "BLOCKS" THEN I = 10000: GOTO stblo

INPUT #1, ES

stblo:

NEXT I

INPUT #1, ES 'ES = 0

INPUT #1, ES 'ES = ENDSEC or BLOCK

IF ES = "ENDSEC" THEN GOTO entbeg

blokstar: 'Control is passed to here from loop below when a new block is
'encountered

INPUT #1, ES 'ES = 8

INPUT #1, ES 'ES = layer name - not used here

INPUT #1, ES 'ES = 2

INPUT #1, bnam\$ 'bnam\$ = block name (SYMBAD cell name)

PRINT #2, "OPEN CELL "; bnam\$ 'Opens cell for storage

INPUT #1, ES 'ES = 70

INPUT #1, ES 'ES = 64

INPUT #1, E1\$: INPUT #1, xb 'E1\$ = 10, xb = base point x coordinate

INPUT #1, E1\$: INPUT #1, yb 'E1\$ = 10, yb = base point y coordinate

INPUT #1, E1\$ 'E1\$ = 0

FOR I = 1 TO 10000 'Get information about each Autocad entity

INPUT #1, ES

SELECT CASE ES

CASE "POLYLINE"

CALL POLY

'PRINT #2,

CASE "INSERT"

CALL ADD

CASE "BLOCK": I = 1000: GOTO blokstar

CASE "ENDSEC": I = 10000: GOTO endblo 'no more blocks

CASE "ENDBLK": PRINT #2, "CLOSE CELL"

END SELECT

endblo:

NEXT I

***** Find ENTITIES information in Autocad file and store in SYMBAD file

entbeg:

FOR I = 1 TO 10000 'Find ENTITIES label in Autocad file

IF ES = "ENTITIES" THEN I = 10000: GOTO stent

INPUT #1, ES

IF ES = "EOF" THEN

PRINT "EOF encountered while searching for ENTITIES."

PRINT "Program terminated."

END 'Terminate program since no ENTITIES were found.

END IF

stent:

NEXT I

PRINT #2, "OPEN CELL "; D\$ 'Opens master cell for entities

lent = 0 'counts the number entities as they are encountered

FOR I = 1 TO 10000 'Get information about each Autocad entity

INPUT #1, ES

SELECT CASE ES

CASE "POLYLINE"

```

        CALL POLY
        PRINT #2,
CASE "INSERT":
        CALL ADD
CASE "ENDSEC": I = 10000: GOTO endent, 'no more entities
END SELECT
endent:
NEXT I
PRINT " "
PRINT A$; " has been converted and saved in SYMBAD file "; B$
PRINT
PRINT "Do you wish to process another file ?"
ANS$ = INPUT$(1)
SELECT CASE ANS$
    CASE "y", "Y"
        GOTO start
END SELECT
END

```

'error handling routine to take care of a bad file name

'all other errors cause program termination

errorhandler:

```
IF ERR = 53 THEN
```

```
    PRINT
```

```
    PRINT "File "; A$; " not found."
```

```
    INPUT "Enter the file to process: ", A$
```

```
    RESUME
```

```
ELSE 'an unrecoverable error has occurred, print message and abort
```

```
    PRINT "Unrecoverable error "; ERR
```

```
    ON ERROR GOTO 0
```

```
END IF
```

```
SUB ADD
```

```
INPUT #1, ES 'ES = 8
```

```
INPUT #1, ES 'ES = layer name - not used here
```

```
INPUT #1, ES 'ES = 2
```

```
INPUT #1, cnam$ 'cnam$ = SYMBAD cell name, to be inserted in present cell
```

```
FOR I = 1 TO 10000 'Extract rotation and multiple insertion information
```

```
    INPUT #1, ES
```

```
    SELECT CASE ES
```

```
        CASE "10"
```

```
            INPUT #1, xi 'x - coord insertion point
```

```
        CASE "20"
```

```
            INPUT #1, yi 'y - coord insertion point
```



```

CASE "50" 'rotation angle follows
    INPUT #1, rang 'rang = rotation angle
CASE "70" 'multiple column insertion information follows
    INPUT #1, ncol 'ncol = number of columns to be inserted
CASE "71" 'multiple row insertion information follows
    INPUT #1, nrow 'nrow = number of rows to be inserted
CASE "44"
    INPUT #1, cspac 'cspac = column spacing
CASE "45"
    INPUT #1, rspac 'rspac = row spacing
CASE "0" 'Last piece of data for this insertion has been reached
    I = 10000
CASE ELSE
    INPUT #1, ES: INPUT #1, ES 'Get past unused data
END SELECT
NEXT I
PRINT #2, "ADD ARRAY "; cnam$;
PRINT #2, "/ROTATE="; rang;
PRINT #2, "/XANCHOR=LEFT/YANCHOR=BOTTOM";
IF nrow > 0 THEN
    PRINT #2, "/ROW="; nrow;
ELSE
    PRINT #2, "/ROW=1";
END IF
IF ncol > 0 THEN
    PRINT #2, "/COLUMN="; ncol;
ELSE
    PRINT #2, "/COLUMN=1";
END IF
IF nrow > 0 THEN PRINT #2, "/YDISPLACE="; rspac;
IF ncol > 0 THEN PRINT #2, "/XDISPLACE="; cspac;
PRINT #2, "/VIEWPORT=1 ("; xi; yi; ")"
END SUB

'Extracts Polygon information from Autocad and prints it to SYMBAD file
SUB POLY
INPUT #1, ES 'ES = 8
INPUT #1, lname$ 'layer name
PRINT #2, "ADD POLYGON "; lname$; "/MODE=ALLANGLE/VIEWPORT=1";
verc = 0 'vertex counting variable
FOR J = 1 TO 10000 'Extract vertex information and test for SEQEND
    INPUT #1, ES
    IF ES = "70" THEN
        switch = 1 'switch = 1 - closed polyline, last point printed to #2

```

```

      'must duplicate first point
'Get first vertex, print to #2, and then store
INPUT #1, ES  'ES = 1
INPUT #1, ES  'ES = 0
INPUT #1, ES  'ES = VERTEX
INPUT #1, ES  'ES = 8
INPUT #1, lname$ 'lname$ = layer name
INPUT #1, ES  'ES = 10
INPUT #1, x1  'vertex x-coordinate
INPUT #1, ES  'ES = 20
INPUT #1, y1  'vertex y-coordinate
PRINT #2, " ("; x1; y1; ") ";
END IF
IF ES = "SEQEND" THEN
  J = 10000
  IF switch = 1 THEN PRINT #2, " ("; x1; y1; ") ";
  PRINT #2, ",";
  GOTO verend
END IF
IF ES = "VERTEX" THEN
  'verc = verc + 1'increment vertex count
  INPUT #1, ES  'ES = 8
  INPUT #1, lname$ 'lname$ = layer name
  INPUT #1, ES  'ES = 10
  INPUT #1, x  'vertex x-coordinate
  INPUT #1, ES  'ES = 20
  INPUT #1, y  'vertex y-coordinate
  PRINT #2, " ("; x; y; ") ";
END IF
verend:
NEXT J
'PRINT #2, "ADD POLYGON "; lname$; "/MODE=ALLANGLE/VIEWPORT=1";
'PRINT #2, " ("; x(1); y(1); ") ";
FOR J = 2 TO verc - 1
  PRINT #2, " ("; x(J); y(J); ") ";
NEXT J
'PRINT #2, " ("; x(verc); y(verc); ") ";
END SUB

```

MISSION
OF
ROME LABORATORY

Rome Laboratory plans and executes an interdisciplinary program in research, development, test, and technology transition in support of Air Force Command, Control, Communications and Intelligence (C3I) activities for all Air Force platforms. It also executes selected acquisition programs in several areas of expertise. Technical and engineering support within areas of competence is provided to ESC Program Offices (POs) and other ESC elements to perform effective acquisition of C3I systems. In addition, Rome Laboratory's technology supports other AFMC Product Divisions, the Air Force user community, and other DOD and non-DOD agencies. Rome Laboratory maintains technical competence and research programs in areas including, but not limited to, communications, command and control, battle management, intelligence information processing, computational sciences and software producibility, wide area surveillance/sensors, signal processing, solid state sciences, photonics, electromagnetic technology, superconductivity, and electronic reliability/maintainability and testability.